^{56}Fe-ion Radiation as a Proxy for Cosmic Radiation: Impacts on Microglial Activity and Anti-inflammatory Strategies in Organotypic Hippocampal Slice Cultures.

1. GSI Helmhotz-Centre for Heavy-Ion Research Darmstadt, FAIR Phase 0
2. Department of Biology at Technical University Darmstadt
3. DLR German Aerospace Centre, FR: 50WB1837, 50WB2025
4. ESA European Space Agency, FR:AO_IBER_2017_011, AO_IBER_2019_015
5. Department of Anatomy at University Leipzig

For obtaining the degree Doctor rerum naturalium

(Dr. rer. nat.)

Dissertation submitted by

Bahar Djouiai

First Supervisor: Prof. Dr. Marco Durante

Second Supervisor: Prof. Dr. Alexander Löwer

Darmstadt 2025

Djouiai, Bahar: ^{56}Fe-ion Radiation as a Proxy for Cosmic Radiation: Impacts on Microglial Activity and Anti-inflammatory Strategies in Organotypic Hippocampal Slice Cultures.

Darmstadt, GSI Helmholtzzentrum für Schwerionenforschung
Technische Universität Darmstadt,

Jahr der Veröffentlichung der Dissertation auf TUprints: 2025
DOI: https://doi.org/10.26083/tuda-7496
URL: https://tuprints.ulb.tu-darmstadt.de/handle/tuda/14689
URN: https://nbn-resolving.de/urn:nbn:de:tuda-tuda-146890
Tag der mündlichen Prüfung: 27.10.2025

ABSTRACT

Astronauts will inevitably be exposed to low doses of ionizing radiation during future space missions, such as the transit to Mars. The effects on the brain and cognitive risks for astronauts are only partially understood, in part due to technical limitations in realistically reproducing the cosmic radiation composition. While neuronal damage in the hippocampus and other brain regions has already been demonstrated, the impact on microglial cell function, the immune cells of the brain, is largely unknown.

The dentate gyrus region of the hippocampus, where neurogenesis occurs, is of particular importance for the integrity of the brain. From neurodegenerative diseases such as Alzheimer's, it's known that prolonged and enhanced activation of microglia can generally lead to secondary damage in the surrounding tissue as well as in neuronal cells. This activation goes along with changes of the microglial cell phenotype. This work utilizes an organotypic tissue system of the hippocampus, in which microglia were examined for morphological changes and inflammatory signals after exposure to low-energy X-rays or high-energy ^{56}Fe-ion (1 GeV/n) radiation. Microglia are quantified and their activation morphologically classified over a period of 0.5 hours to 29 days after radiation exposure. Cytokine and molecular analyses were conducted to investigate the inflammatory profile.

While the total cell count in the dentate gyrus of irradiated OHSCs remained at control levels, X-ray irradiated OHSCs displayed reduced cell death and lower levels of pro-inflammatory IL-6 compared to control groups. In ^{56}Fe-ion irradiated OHSCs, a shift of phenotypes towards reactive microglia and a significant IL-6 increase was observed. An increase in IL-6 was seen only after 48 hours post ^{56}Fe-ion irradiation. Treatment of irradiated OHSCs with the cannabinoid receptor agonist AbnCBD resulted in reduced cell death and a short-term increase of IL-6 levels compared to untreated OHSCs. Post-irradiation treatment with GP1a, a highly specific cannabinoid receptor 2 ligand, resulted in an increase in activated microglia for ^{56}Fe-ion radiation and more cell death in the long term but significant IL-6 reduction. Overall, different inflammatory profiles were observed in the dentate gyrus when irradiated with X-rays or ^{56}Fe-ion radiation.

In summary, OHSCs proved to be a suitable model system to investigate complex tissue alterations for radiation damage. ^{56}Fe radiation did not result in stronger or longer-lasting inflammation. Post-treatment of irradiated OHSCs with AbnCBD and GP1a did not result in significant inflammation reduction but favored microglia activation.

ZUSAMMENFASSUNG

Astronauten werden bei zukünftigen Weltraummissionen, wie dem Transit zum Mars, zwangsläufig niedrigen Dosen ionisierender Strahlung ausgesetzt sein. Die Auswirkungen auf das Gehirn und kognitive Risiken für Astronauten sind nur teilweise verstanden. Die Region des Gyrus Dentatus im Hippocampus, in der Neurogenese stattfindet, ist von besonderer Bedeutung für die Integrität des Gehirns, weshalb die Integrität von Mikrogliazellen, den Immunzellen des Gehirns, von besonderer Relevanz ist. Aus neurodegenerativen Erkrankungen wie Alzheimer ist bekannt, dass eine anhaltende und verstärkte Aktivierung von Mikroglia im Allgemeinen zu sekundären Schäden im umliegenden Gewebe sowie in neuronalen Zellen führen kann. Diese Aktivierung geht mit Veränderungen des Phänotyps der Mikrogliazellen einher.

Diese Arbeit nutzt ein organotypisches Gewebesystem des Hippocampus, in dem Mikroglia auf morphologische Veränderungen und entzündliche Signale nach Exposition gegenüber Röntgenstrahlen mit niedriger Energie und ^{56}Fe-Ionenstrahlung (1 GeV/n) untersucht wurden. Mikroglia des Gyrus dentatus wurden quantifiziert und ihre Aktivierung über einen Zeitraum von 0,5 Stunden bis 29 Tagen nach der Strahlenexposition morphologisch klassifiziert. Zytokin- und molekulare Analysen wurden durchgeführt, um das entzündliche Profil zu definieren.

Während die Gesamtzellzahl im Gyrus Dentatus bestrahlter OHSCs auf Kontrollniveaus blieb, zeigten röntgenbestrahlte OHSCs eine verringerte Zellsterblichkeit und eine niedrigere Konzentration des proinflammatorischen Markers IL-6 im Vergleich zur Kontrollgruppe. Bei ^{56}Fe-Ionen-bestrahlten OHSCs wurde eine Verschiebung der Phänotypen hin zu reaktiven Mikroglia und ein signifikanter Anstieg von IL-6 beobachtet. Eine Zunahme von IL-6 wurde nur 48 Stunden nach ^{56}Fe-Ionenstrahlung festgestellt. Die Behandlung bestrahlter OHSCs mit AbnCBD, einem Liganden des Cannabinoid-Rezeptors GPR55, führte zu einer verringerten Zellsterblichkeit und einem kurzfristigen Anstieg der IL-6-Konzentration. Eine Nachbestrahlungsbehandlung mit GP1a, einem hochspezifischen Agonisten des Cannabinoid-Rezeptors 2, führte zu einer Zunahme aktivierter Mikroglia bei ^{56}Fe-Ionen-Bestrahlung und mehr Zelltod, jedoch zu einer signifikanten Verringerung von IL-6.

Zusammenfassend erwiesen sich OHSCs als geeignetes Modellsystem zur Untersuchung komplexer Gewebeveränderungen nach Bestrahlung. ^{56}Fe-Bestrahlung führte nicht zu stärkeren oder länger anhaltenden Entzündungen. Eine Behandlung von bestrahlten OHSCs mit AbnCBD und GP1a führte nicht zu einer signifikanten Verringerung der Entzündung, begünstigte jedoch die Aktivierung von Mikroglia.

Table of Content

1 INTRODUCTION

During extended human space missions, exposure to high energy particles from solar flares, distant stars and galactic cosmic radiation (GCR) can be a major risk to the CNS of astronauts and can potentially jeopardize their overall health and the mission success.

Studies with GCR on the ground and within lower-Earth-orbit (LEO) on the International Space Station (ISS) have been conducted to investigate the effects of ionizing radiation (IR) on rodents, where radiation has been shown to cause synaptic and hippocampus-associated behavioral changes. As microglia, the immune cells of the brain, adapt rapidly to changes of inflammatory signaling in their cellular environment, they represent a promising target for anti-inflammatory manipulation. Microglia also possess cell membrane receptors that are part of the endogenous endocannabinoid system, which make them a promising target for therapeutic intervention. This study aimed to develop risk mitigation measures for astronauts on deep space missions. For this, the use of organotypic hippocampal slice cultures as a model system for studying the effects of IR from X-rays and ^{56}Fe-ions and the potential therapeutic benefits of the cannabinoid receptor ligands AbnCBD and GP1a to mitigate damage to brain tissue were investigated.

1.1 PHYSICAL PRINCIPALS OF IONIZING RADIATION

Ionizing radiation is a type of electromagnetic radiation that has sufficient energy to remove electrons from atoms and molecules, leaving behind positively charged ions or molecules. Electrons that are released can participate in the further ionization of surrounding matter as secondary events (Hall & Giaccia, 2019). The amount of energy deposited in the tissue by the radiation is known as absorbed dose (D) and is defined as the deposited energy (E) per unit mass (m) of the irradiated object. This energy dose is expressed in the unit Gray (Gy = J/kg) (Formula 1).

Formula 1: $$D\ [Gy] = \frac{E\ [J]}{m\ [kg]}$$

In order to compare the strength of the radiation effect on humans in radiation protection regardless of its energy and type, an equivalent dose is often given in the unit Sievert (Sv). This is the product of the absorbed dose (D) in Gray and a radiation weighting factor (ωR). The International Commission on Radiological Protection (ICRP) selects radiation weighting factors

by taking into account experimental relative biological effectiveness (RBE) values, which are adjusted to favor biological end points that are significant for radiation protection, including cancer and heritable effects (ICRP Publication103, 2007). In addition, the factors are also relevant for low dose irradiation and low dose rates (Hall & Giaccia, 2019). Another measure of the potential biological effect of radiation on the human body is the effective dose, which is calculated by multiplying the equivalent dose received by each organ or tissue by a weighting factor (W_T) that reflects the relative risk of radiation-induced cancer or other health effects. The ICRP introduced the W_T in 2007 and labeled the brain tissue with a W_T of 0.01 (ICRP Publication 103, 2007).

X-rays and gamma rays belong to the electromagnetic spectrum. The energy of X-rays is determined by the frequency of the waves and can be calculated using Planck's equation, where E_{Ph} is the energy of the photon, h is Planck's constant ($6.626 \times 10^{-34}\ J$), and f is the frequency (Formula 2).

Formula 2: $$E_{Ph} = h \times f$$

In an X-ray generator, electrons are accelerated to high energy using an electrical device, which are then suddenly stopped in a target material, typically tungsten or gold. As a result of the sudden deceleration, part of the kinetic energy of the electrons is transformed into X-rays.
Heavy charged particles are nuclei of elements such as iron (Fe) that are positively charged as a result of stripping most or all of their electrons (Hall & Giaccia, 2019). Upon experimental or therapeutic use, heavy charged particles need to be accelerated to high energies in specialized facilities called synchrotrons or cyclotrons.

IR is classified into directly or indirectly ionizing. X-rays are referred to as indirectly ionizing, as they release energy into the material they were absorbed to and subsequently produce energetic electrons, called δ-rays, which are able to further induce damage to the absorber. The δ-rays extend laterally even at a distance from the core track (Cucinotta et al., 2000; Krämer, 1995; Scholz, 2003). Therefore, X-ray radiation is also characterized as loosely ionizing. In contrary, heavy charged particles directly disrupt the structure of the material they pass through and cause chemical and biological alterations along the particle trajectory. The majority of the absorbed dose

is deposited along the particle's trajectory (Scholz, 2003). The dose distribution is locally concentrated in these regions. Heavy-particle radiation is therefore described as densely ionizing.

The biological effects of radiation exposure depend on the amount of dose absorbed by the tissue and the type of radiation. The RBE is a measure of the potential harm of different types of radiation and is defined as the ratio of the dose of a reference radiation (usually X-rays) to that of the test radiation that produces the same biological effect. Heavy particles like Fe have a higher RBE value than X-rays because they deposit more energy per unit length of their track in the tissue, a property known as the linear energy transfer (LET) (Formula 3). The LET is measured in units of $keV/\mu m$ and is related to the energy deposited by the radiation along its path in the tissue. Low LET radiation, such as X-rays or gamma rays, uniformly deposit their energy in the tissue. In contrast, high-LET particles of high energy and charge deposit part of their energy along the trajectory through the tissue.

Formula 3: $$LET = \frac{dE[keV]}{ds\,[\mu m]}$$

Due to atomic and nuclear interactions, the composition and energy of the nuclei passing through the tissue, alters the RBE as a function of penetration depth (Norbury et al., 2016). The biological effectiveness of IR is a topic of considerable interest in the field of radiobiology. IR has the ability to induce significant damage to tissues by ionizing molecules, particularly to the desoxyribonucleic acid (DNA), leading to a range of cellular responses. Among these responses, DNA damage is a key event, including base damage, single-strand breaks, and double-strand breaks. These DNA lesions, if left unrepaired, can result in genetic mutations and chromosomal aberrations, ultimately leading to carcinogenesis (Hall & Giaccia, 2019; Lomax et al., 2013).
Furthermore, IR can generate reactive oxygen species (ROS), which can further exacerbate DNA damage and cause oxidative stress to the cells. This oxidative stress can lead to the induction of inflammatory signaling pathways and inflammatory responses, as well as the alteration of cellular homeostasis. Consequently, IR can induce various modes of cell death, including apoptosis, necrosis, and autophagy, depending on the level and type of exposure, as well as the cell type and stage of the cell cycle (Autsavapromporn et al., 2011; Gómez-Virgilio et al., 2022; Maier et al., 2016).

In summary, IR deposits energy in tissue, measured in Grays, and the biological effectiveness of radiation depends on the RBE and LET of the radiation. IR is a potent source of biological damage, particularly to DNA, which can lead to various cellular responses, such as ROS generation, cell death, and inflammation. Nevertheless, cells have developed (DNA)- repair mechanisms to mitigate the impact of IR and sustain genomic stability.

1.2 Space Radiation Environment

GCR nuclei are believed to originate from supernovae or exploded stars, resulting in a spatially homogeneous particle flux. When combined with episodically released, high-intensity solar energetic particles (SEP), they form the space radiation background, whose level varies during the 11-year solar cycle (Committee on the evaluation of radiation shielding for space exploration, 2008). GCR is predominantly composed of protons (90 %), helium ions (9 %), and heavier ions (1 %) with an energy range of from a few MeV/nucleon up to TeV/nucleon (Mewaldt, 1994; Simpson, 1983). The latter are also referred to as high nuclear Charge (Z) and Energy (E) (HZE) particles. The major GCR particle species include hydrogen (H), helium (He), carbon (C), oxygen (O), neon (Ne), silicon (Si), calcium (Ca), and iron (Fe) (Figure 1). Although Fe (Z = 26) constitutes only 1 % of GCR, it is an important HZE that contributes to GCR's biological effectiveness (Chew et al., 2019).

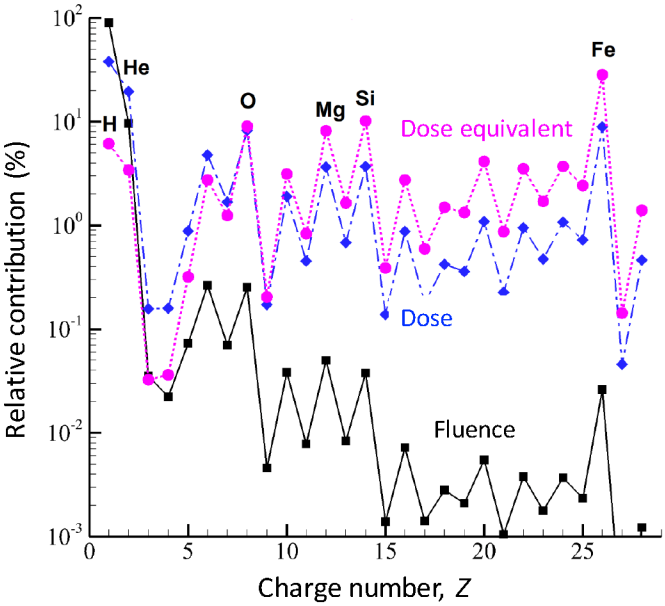

Figure 1 Relative contribution of various elements in GCR to dose equivalent (circles), dose (diamonds) and fluence (squares). Calculations are an average over 1-year in solar minimum behind 5 g/cm² aluminum shielding. (Adapted from Durante & Cucinotta, 2008)

High-LET particles like ^{56}Fe or ^{16}O traverse the astronaut's body only every few months at low fluence rates, resulting in a total dose of 0.3 - 0.6 Gy for a three-year round trip to Mars (Durante, 2014; Guo et al., 2015; Norbury et al., 2016). However, such exposure can permanently damage the astronaut's CNS, compromising their cognition and motor function (Boyd et al., 2021; Klein et al., 2021; Krukowski et al., 2018; Lumniczky et al., 2017). The cohort of astronauts is small, and only seven humans have been beyond LEO during the Apollo Mission (1969 – 1972), which limits direct investigation of biological effects of deep space radiation. Nevertheless, ground-based studies with simulated space-relevant environments are used to investigate the health consequences of GCR exposure. High-energy particle accelerator facilities worldwide provide mono-energetic beams of heavy-ion species at defined energies as an approximation to the complex of space radiation environment. However, these approximations naturally neglect the composition of GCR and other fundamental space environment stressors, such as microgravity and socio-emotional factors like isolation and confinement (Clément et al., 2020; Stuster, 2016). To overcome these technical limitations, advanced space radiation simulators have been developed, such as the NASA Space Radiation Laboratory (NSRL) at Brookhaven National Laboratory and the hybrid active-passive simulation concept at GSI/FAIR in Darmstadt, Germany (Schuy et al., 2020; Simonsen et al., 2020). The science conducted with these newly emerging technologies will eventually improve our understanding of and ability to mitigate risks for future astronauts.

Space agencies regulate astronaut activity based on the effective dose, with 1 Sv being an accepted threshold over the astronauts' lifetime (Cool et al., 2019; ICRP Publication103, 2007). NASA establishes exposure limits separately for cancer-induced mortality and non-cancer effects, which rely on the mission duration, astronaut age, and gender, to maintain a 3 % probability of radiation-induced death with 95 % confidence level (Committee on Assessment of Strategies for Managing Cancer Risks Associated with Radiation Exposure During Crewed Space Missions et al., 2021; Cucinotta et al., 2011). All requirements for astronaut exposure limits should be fulfilled.

Humans on Earth and astronauts within LEO are protected by Earth's magnetosphere. However, during long-duration space exploration missions, shielding and radiation protection remain major challenges that scientists are working to improve. Physical radiation shielding, or passive shielding, is one countermeasure being explored as human operations extend beyond LEO. On-board shielding with hydrogen-rich composite materials, such as polyethylene (PE), with low nuclear charge number (Z) has demonstrated the highest shielding efficiency, as measured by

stopping power and fragmentation cross section (Naito et al., 2020, 2021). However, on-board shielding and the spacecraft itself can also be sources of secondary particles generated by nuclear interactions with the spaceship materials.

The high kinetic energies of GCR result in a high penetration depth, and due to the extremely large clusters of ionization (the so-called penumbra), high-energy electrons deposit large amounts of energy in biological material (Durante, 2014).In addition to passive shielding, increasing distance from the radiation source and shortening mission time are fundamental principles of radiation protection. While neither of these principles is currently part of the future space exploration plans of major space agencies, scientists are exploring other shielding methods that may reduce radiation exposure (Durante & Bruno, 2010).

1.3 CNS UNDER SPACE RELEVANT RADIATION

IR is known to cause significant damage to the CNS by inducing oxidative stress, inflammation, and DNA damage (Heuskin et al., 2016). Cognitive impairments, motor deficits, and other neurological disorders are some of the observed consequences of IR exposure. The extent of CNS damage depends on various factors such as the dose and duration of exposure, age, sex, and genetic susceptibility. For instance, during a three-year Mars mission, an astronaut's individual cell is expected to be crossed by protons once every three days, helium nuclei once every three weeks, and more than two nuclei of higher atomic number once every three months, potentially harming more than 13 % of all neurons (Krukowski et al., 2018). *In vivo* studies have demonstrated that a single ion beam exposure can cause behavioral dysfunctions, including learning and memory deficits, anxiety, and social withdrawal (Davis et al., 2021; Krukowski et al., 2021; B. Liu et al., 2019). These performance decrements can persist for up to 52 weeks and occur simultaneously with changes in structural plasticity, neuroinflammation, and synapse loss (Britten et al., 2014; Limoli, 2020; Parihar et al., 2015, 2018). Previously published data on CNS impairments in mice are summarized in Figure 2. Our study used murine hippocampal model systems of both sexes to explore the yet under-represented area marked in star-shaped in the graph (Figure 2).

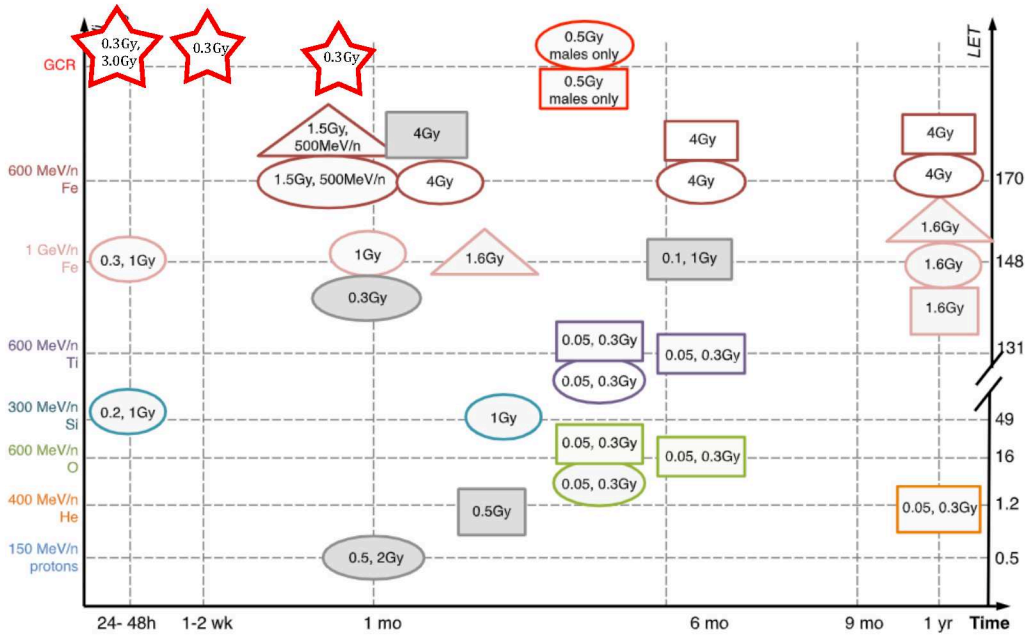

Figure 2 Spatiotemporal mapping of radiation-induced neurological alterations following exposure to charged particles. Time course and particle/energy-dependent effects on neuronal damage and neuroinflammation were assessed in mice exposed to various charged particles (protons to iron ions) at different LET values. Neurological endpoints were evaluated from 24 hours to 1-year post-irradiation and include neuronal/synaptic loss (ovals), gliosis (squares), oxidative stress (triangles), and immunological activation (star-shaped). Numbers within shapes indicate radiation doses in Gray (Gy). White shapes represent significant effects while grey shapes indicate no significant changes from controls. All data are from male mice unless otherwise specified (Adapted from Cekanaviciute et. Al., 2018).

The deleterious effects of HZE radiation on cognitive function have been well established and are attributed to several mechanisms, including inhibition of synaptic activity and loss of dendritic structures. A key factor underlying these alterations is CNS inflammation, which involves the activation of microglia and astrocytes, release of pro-inflammatory cytokines, chemokines, and reactive oxygen species (ROS), resulting in impaired neuronal function and damage (Cucinotta & Cacao, 2019; Parihar et al., 2016). HZE radiation has been shown to activate microglia and prompt the release of cytokines such as IL-1β and IL-6, exacerbating CNS inflammation. The hippocampus, responsible for neurogenesis and neuronal differentiation, is particularly susceptible to these changes, and thus serves as a primary research focus of in this field (Rola et al., 2008a). To mitigate long-term cognitive impairments such as memory deficits and learning impairments, it is essential to understand the underlying mechanisms of CNS inflammation in response to ionizing radiation exposure (Acharya et al., 2019)

1.4 THE HIPPOCAMPAL FORMATION

Since its introduction in the 16th century, the hippocampus has been extensively studied in neuroscience and various functions have been discovered, including learning, spatial information processing, episodic memory, memory consolidation, and emotion regulation (Andersen et al., 2007; Papez, 1995; Robinson et al., 2020; Ruiz et al., 2014; W. Sato et al., 2019) The hippocampal formation comprises the dentate gyrus (DG), the Cornu Ammonis areas 1 to 3 (CA1 - 3), the entorhinal cortex (EC), and the subiculum (Sub) (Figure 3D) (Amaral, 1978; Lorente de Nó, 1934; Witter & Amaral, 2004).

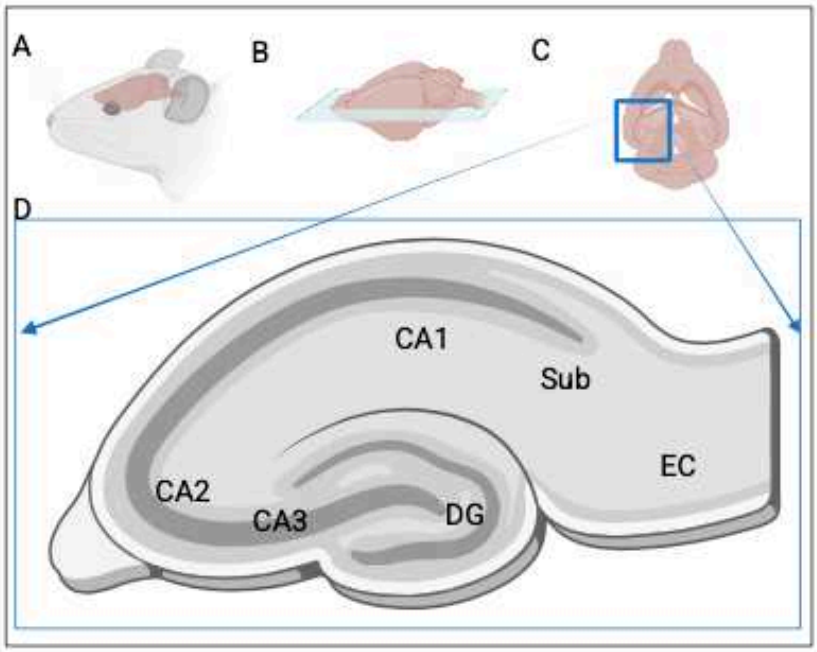

Figure 3 Anatomical organization of the hippocampus in the murine brain. (A) Sagittal view of the rodent brain highlighting the hippocampal formation.(B) Horizontal sectioning from sagital perspective of the mouse brain.(C) Horizontal section of the rodent brain with the hippocampal formation highlighted (blue box).(D) Detailed view of the hippocampal subfields showing the principal anatomical regions: Cornu Ammonis (CA1, CA2, CA3), the Dentate Gyrus (DG), the enthorinal cortex (EC) and the subiculum (Sub). The characteristic curved structure reveals the distinct layered organization of hippocampal subregions (designed with BioRender, 2025).

The DG consists of granule cells, mossy cells, radial glia-like cells (RGLs), astrocytes, and microglia cells. It is organized into three layers: the molecular layer (ML), the granular cell layer (GCL), and the polymorphic layer (PL) or hilus (Ribak et al., 1985) (Figure 4). The neurogenic subgranular zone contains neurons at different stages of maturation, from neural stem or progenitor cells (NSC) to mature neurons (Kempermann et al., 2004). The granular cells give rise to mossy fibers, which terminate in the basal dendrites of CA3 pyramidal basket cells and proximal dendrites of mossy cells in the polymorphic layer (Acsády et al., 1998). The three-layered structure is conserved across many species (Amaral et al., 2007).

The hippocampal formation receives highly processed, multimodal sensory information from various neocortical sources. This information is processed through the hippocampal circuit, beginning with axons from the superficial layers of the EC projecting unidirectionally into the DG via the perforant pathway (PP), the major hippocampal input pathway (Andersen et al., 2007) (Figure 3).

1.4.1 The Dentate Gyrus

The DG harbors a stem cell population that generates new neurons through neurogenesis, which occurs throughout life in only two brain regions: the subventricular zone (SVZ) of the lateral ventricles and the subgranular zone (SGZ) of the DG (Altman & Das, 1965; Andersen et al., 2007) (Figure 4). Neurogenesis encompasses the developmental steps from neural stem cell division to mature, functionally integrated neurons (Kempermann et al., 2003). Studies show that its suppression increases hippocampal degeneration after severe continuous seizures (status epilepticus), while its enhancement reduces neurodegeneration, especially in the hilus and CA1 region, suggesting that new neurons protect the adult mouse brain (Jain et al., 2019). However, heavy-ion radiation exposure risks short- and long-term neurogenesis deficits (Rivera et al., 2013; Rola et al., 2004, 2008b).

1.4.2 Organotypic Hippocampal Slice Cultures

Organotypic hippocampal slice cultures (OHSC) are a valuable model system for studying various aspects of hippocampal physiology and pathology. (Delbridge et al., 2020). The tissue cultures consist of self-contained, three-dimensional slice of neuronal tissue and closely resemble the native microenvironment of the brain, providing an accurate representation of the cellular interactions and signaling pathways *in vivo* (Gähwiler et al., 1997; Holopainen, 2005; Stoppini et al., 1991). Within OHSCs, all cell types maintain their morphologic characteristics and blood vessels are preserved (Delbridge et al., 2020; Humpel, 2015; Muller et al., 2003) (Figure 4). Neural excitation enters via the molecular layer perforant pathway projections to the CA1 region.
OHSCs offer advantages over *in vivo* studies, including enhanced experimental control, reproducibility and the ability to isolate specific cell types or signaling pathways, while serving as a more ethical and cost-effective alternative. However, successful preparation requires considerable expertise to prevent contamination and culture mortality. Notably, isolated *ex*

vivo cultivation significantly alters microglial phenotype and gene expression, resulting in the loss of their homeostatic gene signature (Timmerman et al., 2018).

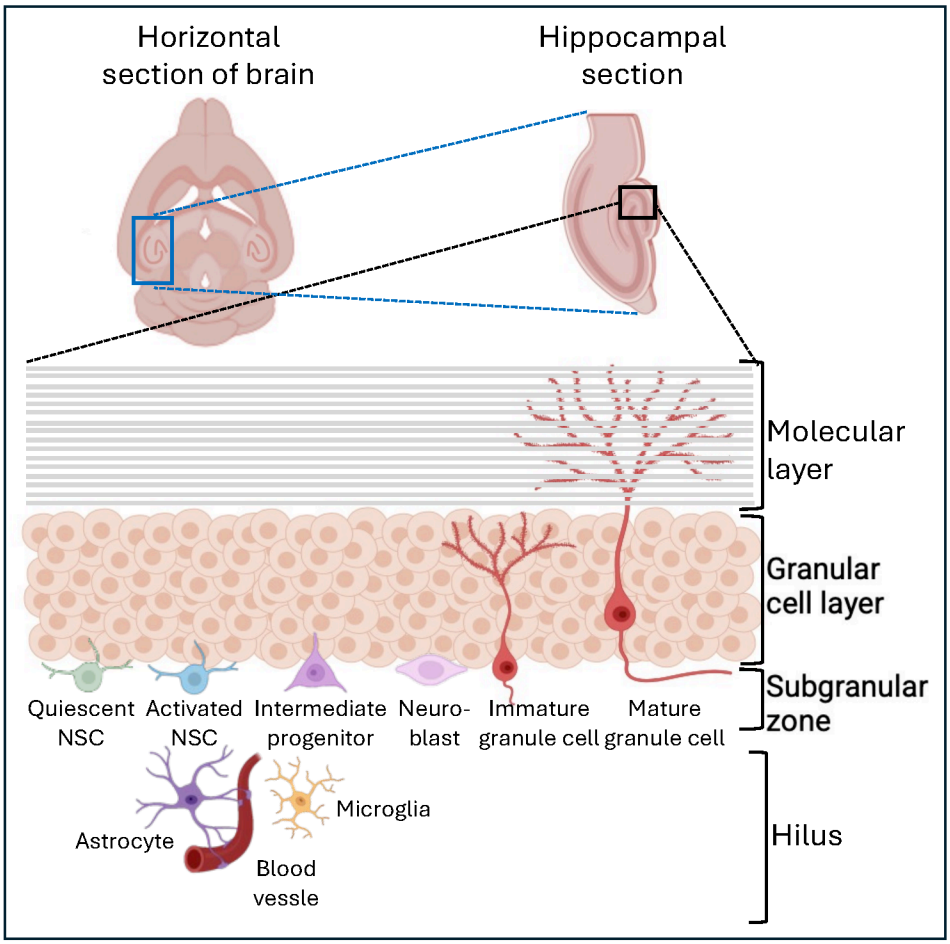

Figure 4 Neurogenesis in the adult hippocampal dentate gyrus. Schematic representation of a horizontal brain section highlighting the hippocampus, with detailed cellular organization of the dentate gyrus. The molecular layer, granular cell layer, and subgranular zone are shown with their distinct cellular components. Neural stem cell (NSC) development is illustrated through various stages: quiescent NSC, activated NSC, intermediate progenitor, neuroblast, immature granule cell, and mature granule cell. Supporting cells including astrocytes, microglia, and blood vessels in the hilus region are also depicted (designed in BioRender 2025).

1.5 Microglia: Origin & Functions

Microglia cells are the resident immune cells of the CNS, originating from yolk sac precursors and colonizing the CNS during embryonic development (Prinz et al., 2021a). They play critical roles in brain development, homeostasis, and neurological disorders. Microglia's well-known functional behaviors include (i) constant surveillance of the tissue environment, (ii) neuroprotection, (iii) phagocytosis of cell debris and (iv) synaptic remodeling (Prinz et al., 2021a; Sierra et al., 2010). To fulfill the key functions, the microglia-neuron crosstalk is a key interaction. Following an

impairment of the brain tissue (depending on the source and energy of the damage), damaged cells secrete inflammatory and apoptotic cytokines to initiate necessary repair mechanisms and alert their surroundings to their possible decay. Evidence suggests that when 'activated', microglia can harm neurons by generating reactive oxygen and nitrogen species, cytokines, chemokines, and other inflammatory mediators. In turn, dying neurons release additional stimulatory substances, exacerbating microglia activation (Bennett et al., 2018; Tanaka et al., 2020), which activate microglia. Interestingly, systemic immune suppressive strategies for resolving neuroinflammation are often counterproductive because they inhibit microglia activation, which is needed to resolve the inflammatory process as described above (Schwartz & Baruch, 2014). Merlini and colleagues' research demonstrated the significance of microglia motility and surveillance in the control of microglia-neuron interactions (Borst et al., 2021; Merlini et al., 2020). As seen in neurological disorders with impaired microglia dynamics, hypersynchrony, a state of abnormal synchronization among neuronal populations or groups of neurons, which can result in the generation of excessive electrical activity, is prevented by the microglia response to physiologically evoked neuronal activity. This mechanism, which controls the signaling of purinergic, glutamatergic, and adenosine G_i-coupled receptors on microglia, is obviously crucial to interactions between microglia.

The brain has long been described as immunologically privileged (Carson et al., 2006), suggesting that it not only represents a constricted system to the periphery through the blood-brain barrier (BBB), but also describes the persistent nature of neurons of favoring cellular repair over replacement and cell death (Daneman & Prat, 2015) .

1.5.1 MICROGLIA CLASSIFICATION

In their resting state, (simplified: M0-phenotype) microglia express a range of pattern recognition receptors (PRRs) on their cell surface. These PRRs identify endogenous host-derived molecules, also known as damage-associated molecular patterns (DAMPs), that are released by damaged cells in the CNS. Upon recognition of DAMPs, intracellular cascades and downstream transcription factors are activated, ultimately leading to the synthesis of inflammatory mediators (Murray et al., 2014). Preceding this is a dynamic morphological change of microglia, which can be simplistically categorized into two activated main types: the classically activated M1-phenotype, associated with pro-inflammatory and neurodegenerative responses, and the alternative M2-phenotype, whose morphological changes exhibit anti-inflammatory and neuroprotective properties (Kigerl et al.,

2009; Martinez & Gordon, 2014). The M2-phenotype is further divided into M2a to M2c, depending on the phenotype, corresponding cytokines, chemokines, and other signaling molecules which are secreted. Within the scientific community, it is widely recognized that this classification falls short in capturing the complexity and resulting functions of microglia (Ransohoff, 2016), leading to discussions about new terminologies for describing microglial morphologies (EMBO Workshop, Microglia 2021). To more accurately describe the microglial form and function, this study adopted a classification based on the current research of Professor Bechmanns group at the University of Leipzig.

Three functional cell types were distinguished: ramified, reactive, and amoeboid. In response to neuronal damage, microglia transform their morphology from ramified to reactive and eventually to amoeboid, to migrate to the site of damage and execute their immune response. This is achieved by retracting their processes, which increase the size and volume of the cell body. In the reactive form, the cells continue to monitor their environment and identify the damaged site as well as individual cells that need to be cleared. Once appropriate signaling molecules are given, a further transformation occurs towards the activated, amoeboid and phagocytic microglia. The processes are now completely retracted, with only stubs visible on the cell body, and the cell body is visibly enlarged. In this morphological status, microglia can migrate to the wound site within minutes of the onset of damage and phagocytose dead cells and debris. Microglia undergo several morphological stages during this transformation process, many of which are functionally relevant (Lumniczky et al., 2017). A persistent activation of microglia is the hallmark of a chronic neuroinflammation. Single-cell RNA sequencing (scRNA- seq) has been used to extensively investigate the molecular characteristics and phenotypic diversity of microglial functions. However, it lacks the ability to provide spatial information about brain homeostasis and disease progression mechanisms (Galatro et al., 2017; Gosselin et al., 2017).

In the scientific literature, activated microglia cells are often described as pro-inflammatory and detrimental to neurons, which may lead to the perception of them being ‘harmful’. However, it is important to emphasize that the primary function of microglia, as innate immune cells, is the protection of neuronal tissue. If activated microglia cells were inherently destructive, chronic microglia-associated diseases such as Alzheimer's would not exhibit a chronic course, but rather result in rapid degradation of all neuronal structures. The neuroprotective function of activated microglia has been demonstrated in various contexts, including the postnatal brain, where depletion of activated microglia has been shown to lead to increased apoptosis (Fujita & Yamashita, 2021). Therefore, the balance between the neuroprotective and neurotoxic functions

of activated microglia is complex and dependent on the type of damage incurred, but it has not yet been fully elucidated.

Microglia cell population remains steady from late postnatal stages until aging, which is maintained through a precisely regulated equilibrium between slow and local proliferation cell division and programmed cell death, without any involvement of progenitors (Askew et al., 2017). However, during conditions of disease, microglia can rapidly undergo clonal proliferation and self-renewal (Borst et al., 2021; Ginhoux & Guilliams, 2016; Mildner et al., 2007).

1.6 THE ENDOCANNABINOID SYSTEM

The endogenous endocannabinoid system (ECS) is a complex signaling system involved in the regulation of various physiological processes, including pain, inflammation, appetite, and mood and homeostatic processes in the brain. It consists of endocannabinoids, receptors, and enzymes responsible for their synthesis and degradation. The endogenous ECS ligands, N-arachidonoylethanolamide (AEA) and 2-arachidonoylglycerol (2-AG) activate the receptors, resulting in a reduction in neurotransmitter release and thereby mediate synaptic plasticity (Kano et al., 2009; Robledo-Menendez et al., 2022). The main proteins of the ECS are the cannabinoid receptors (CB)1 and 2, which are dormant G-protein-coupled receptors that are mainly coupled to Gi/o α subunits (Gαi/o). The binding of an agonist activates the receptors and allows for exchanging guanosine diphosphate (GDP) for guanosine triphosphate (GTP) on the α subunit of the G-protein. Gα dissociates from the Gβγ dimer and from the receptor and inhibits adenylyl cyclase (AC) and subsequently the cyclic adenosine monophosphate (cAMP)-dependent pathway. Gβγ regulates mitogen activated protein kinases (MAPKs) and thereby affects calcium and potassium channels (Bosier et al., 2010). The CB1 are mainly found on neurons in the neocortex, hippocampus, basal ganglia and the brain stem (Herkenham et al., 1991) and was first cloned as a binding receptor for Δ9- tetrahydrocannabinol (Δ9- THC), the major psycho-active compound of the plant Cannabis sativa. CB2, on the other hand, are primarily located on immune cells, such as macrophages and microglia. Both CB1 and CB2 receptors are naturally involved in the modulation of neuroinflammation and have been shown to play a role in the regulation of microglial activity (Ativie et al., 2018; Atwood & MacKie, 2010). In response to inflammation, microglial activation occurs, leading to altered expression of cell surface receptors and cytokine release. The orphan G-protein-coupled receptor 55 (GPR55), first described by Sawzdargo et al. in 1999 is expressed in

peripheral tissue and the CNS by monocytes and microglia cells (Sawzdargo et al., 1999). Although it shares several cannabinoid ligands with CB1 and CB2, leading to the hypothesis that it might be a putative 'CB_3' cannabinoid receptor, GPR55 exhibits low amino acid identity of 13.5 % to 14.4 % to the cannabinoid receptors (Sawzdargo et al., 1999). Further, in contrast to the cannabinoid receptors CB1 and CB2, GPR55 only couples to $G\alpha_{12,13}$ proteins which leads to the activation of the ras homolog gene family member A (RhoA) and Rho-associated protein kinase (ROCK). Both CB2 and GPR55 were found on the surface of microglial cells and hence can be targeted to modulate inflammatory processes.

1.6.1 CANNABINOID-RECEPTOR LIGANDS

Abnormal cannabidiol (AbnCBD) and GP1a (N-(piperidin-1-yl)-1-(2,4-dichlorophenyl)-1,4-dihydro-6-methylindeno(1,2-c) pyrazole-3-carboxamide) are synthetic ligands of the ECS and show potential for therapeutic use for inflammation mitigation. AbnCBD is a synthetic derivative of cannabidiol (CBD) and a potent agonist for GPR55, that has been shown to have anti-inflammatory and neuroprotective effects (Krohn et al., 2016; Tudurí et al., 2017; von Widdern et al., 2020).

GP1a is a synthetic cannabinoid and a highly potent selective CB2 agonist. GP1a has been shown to promote wound healing, mitigate inflammation and fibrogenesis while benefitting re-epithelization (Wang et al., 2016; Zhao et al., 2021). In this study, the efficacy of GP1a and AbnCBD, are being investigated for attenuating a possible inflammatory responses or chronic microglial activation that may arise, leading to a reduction in radiation-induced tissue damage.

The use of these synthetic ligands provide a promising avenue for the development of novel therapeutics targeting the ECS. Targeting CB_2R and GPR55 has the potential benefit of more specific immune cell activation while simultaneously avoiding unwanted, psychoactive side effects associated with activating CB_1Rs.

1.7 MITIGATING SPACE RADIATION DAMAGE

Several nutritional supplement compounds with antioxidant properties, including L-Selenomethionine (SeM), N-acetyl cysteine (NAC), ascorbic acid (vitamin C), co-enzyme Q10, α-lipoic acid and vitamin E succinate, were found to have significant suppressive effects on space radiation-induced oxidative stress *in vitro* when used alone or in combination (Guan et al., 2006;

Kennedy & Wan, 2011). These compounds were also found to protect against radiation-induced cytotoxicity, transformation, and oxidative stress in animals exposed to HZE particles, protons, and γ rays (Sridharan et al., 2015; Yoo et al., 2014). In addition, the soybean-derived protease inhibitor, Bowman-Birk inhibitor (BBI), which is used in human trials as an anti-carcinogenic agent, was evaluated for its ability to affect radiation-induced malignancies in animal studies (Kennedy et al., 2006).

The idea of using radio-protective substances is continually revisited because there is likely no single substance that will be effective against all potentially emerging radiation-induced damages (M. Li et al., 2014). Aminothiol amifostine (Ethyol) is known from radiotherapy and has been tested as a chemo-radio-protectant since the mid-1990s but still delivers controversial results (Kouvaris et al., 2007; Seed et al., 2002). Therefore, there is a need for effective, cost-effective, and harmless substances for the prevention or post-treatment of radiation-induced damage (Durante & Cucinotta, 2008; Moreno-Villanueva et al., 2017).

Previous research on neural tissue response to radiation exposure has predominantly focused on isolated time points, with Elgart et al. (2018) primarily examining effects after 24 hours and Belcher et al. (2020) mainly investigating long-term consequences after 14 days (Belcher et al., 2020; Elgart et al., 2018). A comprehensive, continuous observation of the dynamic changes over time is notably absent, as Hladik and Tapio (2021) critically pointed out in their review on radiation-induced neuronal damage (Hladik & Tapio, 2016). The varying activation patterns of microglia in response to radiation were described by Cai et al. (2019), albeit without a systematic characterization of the temporal dimension of this activation (Boyd et al., 2021a). The present study conducts, for the first time, an extensive temporal analysis that integrates immediate effects (within 0.5 hours), short-term effects (12-48 hours post-irradiation), and long-term consequences (7-29 days), providing a unique insight into the dynamic development of microglial activation and associated neuroinflammatory processes. This novel approach addresses a significant research gap identified by Liu et al. (2022), who emphasized the necessity of examining microglial responses across a temporal continuum to more precisely define therapeutic intervention windows (Q. Liu et al., 2022).

1.8 AIM AND MOTIVATION

Space agencies' mission plans have the goal of human exploration of Mars (ISECG, 2020). During transit, astronauts are inevitably exposed to space radiation (Chancellor et al., 2014). However,

there is limited data on the effects of this high-LET radiation on the dentate gyrus within the hippocampus, the brain region responsible for learning, memory, and emotional processes. *In vivo* studies suggest neuronal damage and long-term impairment in animal subjects. The influence of microglial cells, the immune cells of the brain, is still being investigated and indicates inflammatory dysregulation of these cells.

This study aims to investigate the short- and long-term effects of low-dose X-ray (low-LET) and ^{56}Fe-ions (high-LET, 1 GeV/n) on the morphology and accompanying immune response of microglia in the OHSC model. Additionally, this study aims to compare the anti-imflammatory effects of cannabinoid receptor ligands AbnCBD and GP1a on microglia. The findings from these studies may offer a novel therapeutic approach to protect astronauts during deep space long-duration missions and may also provide harmless damage-minimization in radiation therapy of patients.

2 MATERIALS AND METHODS

All chemicals were pA quality. Water for preparing solutions and buffers was generated in an ultrapure water system (Millipore) by reverse osmosis and was always autoclaved before use. In the following, this high-purity water is referred to as MilliQ.

2.1 MATERIALS

2.1.1 ANIMALS

C57BL/6J wild-type (wt) mice were obtained from the medical-experimental center (MEZ), University of Leipzig, or purchased from Charles Rivers. Pregnant mice were housed in the animal facility until they gave birth. On postnatal days 3-4, mice were sacrificed by decapitation for dissection.

2.1.2 TABLES OF MATERIALS

Table 1 List of specific reagents

	Reagens	Manufacturer	Concentration/ Dilution	Secondary Antibody/ 3'-Overhang	Solvent/ lenght	Reference Number	Special Note
Slice culture medium	Minimal Essential Medium 1X (MEM)	Gibco	50 %			21090-022	+ Earle's Salts
	Donor Equine Serum (NHS)	GE Healthcare Life Science, HyClone Laboratories	25 %			SH30074.03	
	Hank's Balanced Salt Solution 1X (HBSS)	Gibco	25 %			24020-001	
	GlutaMAX™- I 100X	Gibco	1 %			35050-061	
	Penicillin/Steptomycin (Pen Strep)	Gibco	1 %			15140-122	+ 10.000 Units/mL Penicillin + 10.000 µg/mL Streptomycin
	Glucose Solution (45 %)	Corning	1 %			25-037-CIR	
Preparation medium							
	Minimal Essential Medium 1X (MEM)	Gibco	98 %			21090-022	+ Earle's Salts
	GlutaMAX™- I 100X	Gibco	1 %			35050-061	
	Penicillin/Steptomycin (Pen Strep)	Gibco	1 %			15140-122	+ 10.000 Units/mL Penicillin + 10.000 µg/mL Streptomycin
Antibodies							
	NeuN mouse monoclonal antibody	Millipore Sigma	1:100	Goat anti mouse 633		MAB377	5% (v/v) Roti
	DAPI solution	BD Pharmingen	1:2000	405	PBS	564907	
	GFAP monoclonal mouse antibody	BD Pharmingen	1:500	Goat anti mouse 633		556327	5% (v/v) Roti
	Isolektin GS-iB4 (IB_4) Griffonia simplicifolia	Thermo Fisher Scientific - Life Technologies - Invitrogen	1:50	Alexa Fluor™ 647 Conjugate	1 mM $CaCl_2$	I32450	pH 7.15
	Propidium Iodide (PI)	Sigma-Aldrich	5µg/ml		PBS	P4864-10ML	emission max. 536 nm
Solutions							
	GP1a	Tocris	10 µM		DMSO	2764	
	abnCBD	Tocris	10 µM		DMSO	1297	Evaporate methyacetate under nitrogen flow
	Paraformaldehyde (PFA)	Thermo Scientific	4 %		PBS, 16 % Formaldehyde Solution (w/v)	28908	
	PBS				NaCl 9,00 g, KH2PO4 0,54 g, Na2HPO4 2,27 g		
	Blocking Solution 1		5 % Normal Goat Serum + 0.02 M PBS/0.3 % Triton (PBST)				
	Blocking Solution 2:		0.5 % BSA in 0.02 M PBST				
Kit's							
	Mouse IL-6 High Sensitivity ELISA Kit	Thermo Fisher Scientific - Life Technologies - Invitrogen				BMS603HS	
	GeneSilencer-siRNA Transfection Kit	Genlantis				T505750	
siRNA							
	Cnr1 (CB1)	eurofins	20nmol	dTdT rUrG	19		5'-3': CAACAUUACAGAGUUCUAU 3'-5': GUUGUAAUGUCUCAAGAUA
	Cnr2 (CB2)	eurofins	20nmol	dTdT rArU	19		5'-3': ACUCUAUGGUCAAUCCUAU 3'-5': UGAGAUACCAGUUAGGAUA
	Gpr55 (GPR55)	eurofins	20nmol	dTdT rGrA	19		5'-3': CUGUGUUUCUCCAACAUCA 3'-5': GACACAAAGAGGUUGUAGU
qPRC	Primer Sequence (5'->3')	Direction	Amplicon Length (bp)	Annealing Temp. (°C)			
CNR1	CTGGGCACCTTCACGGTTCT	Forward	84	62.40			
	GTAGGAAGGCCTGCATCGGA	Reverse		61.69			
CNR2	GGCCCAAGGTCCTCGGTTAC	Forward	133	62.53			
	GGACTTCTGACTCGGGCTGT	Reverse		61.54			
GPR55	CCAGTGCACTTGGGCTTCTTC	Forward	79	61.75			
	TGATGCCCTGCTTCATTCTGC	Reverse		61.29			

Table 2 List of specific equipment

Devices	Manufacturer	Model Number	Specification
Cell Culture Inserts - Millicell-®CM	Millipore	PICM0RG50	0.4 μm, 30 mm diameter
Mullkompressen - Gazin®	Lohmann & Rauscher	PZN 238 690 8	7.5 x 7.5 cm
1.5 % Agarose Gel			in 30 % TAE-Buffer + 1 % PenStrep
Microscope	Olympus IX81		Fluoview Version 4.2
3D printed angled step for plate positioning	self-made		suitable for 6-well plate

2.2 METHODS

Unless otherwise specified, all data sets comprise three independent comparative experiments (N = 3). All OHSCs within each experiment were derived from the same litter (same parents). OHSCs from each litter were pooled and distributed with three slices placed on each tissue culture insert. Each insert containing 3 OHSCs represents an independent experimental condition (n = 1). Each OHSC contains the complete hippocampal formation, incorporating the DG, hilus (H), CA1-CA3 regions, as well as the associated connected subiculum and entorhinal cortex. Throughout this study, experimental conditions are denoted in figure legends as 'N' (number of independent experiments), 'i' (tissue culture insert), and 's' (individual OHSCs). For consistency in graphical representation, the time points '7 days', '16 days', and '29 days' were converted to hours and expressed as 168 hours, 384 hours, and 696 hours, respectively.

2.2.1 ORGANOTYPIC HIPPOCAMPAL SLICE CULTURES

OHSC were prepared using a modified method first described by Stoppini and colleagues (Stoppini et al., 1991). The slice cultures were prepared from 3-4-day neonate C57BL/6J mice. The Animals were decapitated and the brains removed under semi-sterile conditions. The cerebellum and the frontal lobe were removed with a vertical cut using a scalpel and brains were and immediately placed into cold minimal essential medium (MEM) containing 1 % (v/v) GlutaMAX (Gibco) and 1 % (v/v) penicillin/streptomycin. Two to four brains were simultaneously mounted ventral side view with the forebrain facing the vibratome blade with a tissue adhesive (Histoacryl, Braun, Melsungen, Germany) on a vibratome specific stamp. They were stabilized with aseptic 1.5 % agar blocks on the sites for the slicing procedure. The stamp with the brains was then placed in the medium dish filled with cold preparation medium. With the sliding vibratome (Leica VT 1200S, Leica Microsystems AG, Wetzlar, Germany) the brains were sliced horizontally into 350 µm thick tissue slices and were collected in cold preparation medium. Only slices in which the typical hippocampal regions dentate gyrus (DG), cornu ammonis 1-3 (CA1-3) and EC were visible, intact and in the desired brain layer were selected for cultivation. Out of both hemispheres the hippocampi including the EC (Figure 6)were cut out with a scalpel under a binocular (Zeiss) and placed on cell culture inserts (pore size 0.4 µm; Millipore, Schwalbach/Ts., Germany) for 6-well culture dishes (Falcon, BD Biosciences Discovery Labware, Bedford, MA). The wells were pre-filled with 1 ml slice culture medium and cultivated at 37°C.

2.2.2 CULTIVATION AND TREATMENT OF OHSCS

The OHSCs were cultured at 37°C in a fully humidified atmosphere of an incubator with 5 % (v/v) CO_2. They were kept in culture for 11-14 days after dissection before any treatment. The medium was changed 2 hours and 24 hours, then every other day after dissection.
After treatment or irradiation, the culture medium was changed every third day to accumulate measurable amounts of cytokines and chemokines. To add a treatment, appropriate master-mixes were prepared with culture medium and completely exchanged for the existing medium underneath the inserts. DMSO, AbnCBD and GP1a were prepared 1:2000 in fresh tissue culture medium before medium exchange.

2.2.3 IRRADIATION OF OHSCS

2.2.3.1 X-ray irradiation

The irradiation with a single dose of X-rays, as a reference to particle beams, was performed at GSI using the MXR 320/26 X-ray tube from Comet. The X-ray tube was operated with a tube voltage of 250 kV and a current of 16 mA. Irradiation was performed at 27 cm from the radiation source and at a dose rate of ~ 1.87 Gy/min. OHSC were irradiated either at 13-14 days *in vitro* (div) with sham, 0.3 or 3.0 Gy X-rays.
Irradiation with X-rays was partly conducted using the X-ray device (XStrahl 200, XStrahl, Camberley, UK) at a dose rate of ~ 1.85 Gy/min, Medizinisches Versorgungszentrum (MedVZ) - Radiotherapy at University Clinics Leipzig.

2.2.3.2 Iron Irradiation

The heavy ion exposure was performed the heavy-ion synchrotron (SIS 18) of the GSI Helmholtz Centre for Heavy Ion Research using ^{56}Fe (1 GeV/u; LET ~170 keV/µm, 0.3 Gy or 3.0 Gy). Three days prior to irradiation (-72 hours) tissue culture supernatant was collected and stored at – 80°C for baseline values. To create a homogenous dose distribution on the 6-well plate, the plate positioned vertically. To avoid leakage of culture medium during this vertical irradiation, 3D printed brackets with an intermediate step were designed and printed to create an 10° angle

towards the plates' bottom side. Shortly before irradiation, 8 layers of sterile Gauze compresses (Hartmann, Heidenheim, Germany) with a diameter of approximately 3.5 cm were positioned underneath the tissue culture insert to prevent the insert membrane from drying out andn medium leackage during irradiation. Another, inner lid, which was placed on top of the insert, secured it's positioning within the closed 6-well plate. Immediately after ion exposure the culture plates were positioned horizontally. The Gauze compresses were removed and individually centrifuged at 13.000 rpm for 2 min to extract the culture medium, which was transferred back to the referring well. Cannabinoids AbnCBD, GP1a and DMSO were added to the according wells and plates were further cultivated until fixation. Tissue culture medium from early samples (~30 min after irradiation) were collected and stored at -80 °C until further analysis.

2.2.4 STAINING OF DEAD CELLS IN OHSCS

Propidium iodide (PI) is a non-damaging fluorescent dye that penetrates damaged cell membranes and accumulates in the cell's nucleus by attaching to the DNA. PI (Sigma-Aldrich) was used as a 5 µg/ml solution per well to analyze the number of dead cells in the tissue samples. PI was directly added to each well 2 h prior to fixation. The tissue was then fixed with 4 % (w/v) paraformaldehyde (PFA) (Sigma-Aldrich) in 0.1 M phosphate-buffered saline (PBS) (Gibco) for 18-24h before it was stored in PBS until further analysis.

2.2.5 HISTOCHEMICAL STAINING OF MICROGLIAL CELLS IN OHSCS

To visualize microglia cells within the tissue, slices were stained using Isolectin GS-B4 (IB_4) conjugated to a fluorochrome (Isolectin GS-IB_4, Alexa Fluor 647 conjugate) (Invitrogen, Oregon, USA). For this the slices were carefully brushed down the insert and transferred to a blocking solution consisting of 5 % Normal goat serum (NGS) in 0.02 M PBS and 0.3 % Trition (PBST) for 30 min at room temperature on an orbital shaker at 3000 rpm. Subsequently the tissue was incubated with IB_4 (1:50 in 0.5 % (w/v) BSA in PBST) over night at 4°C on an orbital shaker. To visualize the cell nuclei a 4′,6-Diamidino-2-phenylindole (DAPI) staining (1:2000 in PBST) was performed for 10 min on an orbital shaker at room temperature. The samples were then washed twice with PBS and were each embedded in 60 µl fluorescent mounting medium (Dako Diagnostika GmbH, Hamburg, Germany) for microscopy.

2.2.6 MORPHOLOGICAL ANALYSIS OF TISSUE

To analyze cell death and microglia number and morphology in the dentate gyrus hippocampal region 24 µm z-stacks (2 µm) with a 20-fold magnification were generated at the inverse Olympus IX81 laser scanning confocal microscope (Olympus, Hamburg, Germany) with the Olympus software Fluoview ver.4.2. The microglia morphology and number and the dead cell count in the dentate gyrus were analyzed with ImageJ, OIB data images (U.S. National Institutes of Health, http://rsb.info.nih.gov/ij/download.html). Two comparative methodologies were employed to assess microglia morphology, cell count, and the presence of dead cells in the DG region of the OHSC. Utilizing 24 µm stack images stored as OIB files as the initial dataset, ImageJ was utilized for manual assessment. Five random microglia from the DG region were selected, with their soma and entire territory delineated, and photorecords were enumerated. Concurrently, manual counting and documentation of dead cells in the whole referingn DG was performed, with positional coordinates recorded for all cells for subsequent identification. Subsequently, from a dataset comprising over 1400 cells, 20 representative cells per morphological class were chosen, each exhibiting characteristic morphology.

For machine learning analysis, OIB files were imported into GIMP, and all discernible microglial and dead cells were centrally marked, with individual image tiles created for each cell. Only cells identified through both manual and machine analyses were included in constructing the following neuronal network analysis. Training data comprising 800 manually assigned cells per morphological class were utilized for subsequent automated classification, resulting in the assignment of over 14,000 cells.

2.2.6.1 Classification of microglia morphologies in OHSCs

In both analytical methodologies, cell classification was conducted based on three key measurement parameters: soma size, territorial area, and the number of primary processes. Manual evaluation outcomes were stratified via cluster classification, whereby each assessed cell was allocated to a pre-established morphological class. In the realm of machine learning, all parameter data were initially aggregated into a matrix, utilizing clustering techniques under unsupervised learning paradigms. Subsequently, the resulting point clouds were utilized to discern the three distinct morphological classes through labeling procedures under supervised learning frameworks. By iteratively determining the centroid of each point cloud, the entirety of

the 14,000 cells underwent classification, being allocated to one of the three classes within the matrix. It should be noted that only the combined observation of cytokine release, morphology and tissue condition can lead to a reliable statement about neuroinflammation in the tissue.

2.2.7 HIGH SENSITIVITY ELISA

IL-6 is a pro-inflammatory cytokine that is involved in immune response and multiple functional and behavioral reactions of the CNS. In the brain microglia appear to be the main cell type to express IL-6 receptors. The state of inflammation of the OHSC was measured via a highly sensitive enzyme-linked immunosorbent assay (HS-ELISA) (Invitrogen) for the quantitative detection of mouse interleukin-6 (IL-6) secreted into the tissue culture supernatant. The tissue supernatants were collected over a total period of 72 h to accumulate sufficient cytokines above the measurable threshold of the high-sensitivity ELISA kit's. An analysis before 72 h only yielded values below the sensitivity threshold of the analysis kit (see 'Multiplex analysis' in the appendix).

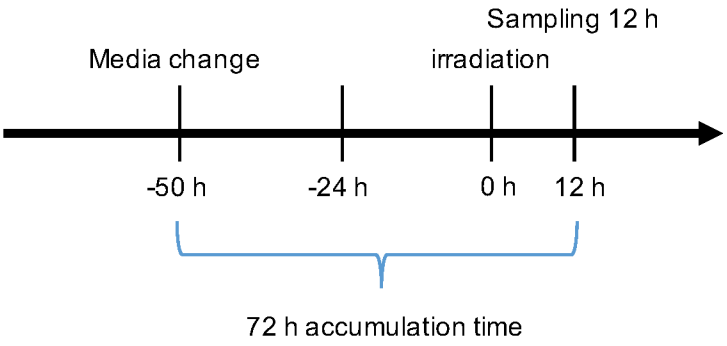

Figure 5 Schematic representation of sample collection for the 12 hour time pointafter irradiation.

The HS-ELISA was conducted according to the manufacturer's instruction. Briefly, a 96-well plate absorbed with an anti-mouse IL-6 coating antibody was used to analyze the mouse IL-6 in the collected tissue culture supernatant. Microwell strips were washed twice. Standards, samples and the biotin-conjugate, which binds the IL-6 captured by the first antibody, were added to the according wells and incubated at 4°C over night in the dark. Wells were washed 6 times and the streptavidin/ horse radish peroxidase (HRP) was added and incubated for 1 h at room temperature on a shaker. Wells were washed again and amplification solution I was incubated for 15 min before amplification solution II was added and additionally incubated for 30 min at room temperature on a shaker. After another washing step 3,3',5,5'-Tetramethylbenzidine (TMB)

substrate solution was added to all wells and incubated for another 18 min before stop solution was added. The absorbance was read with a spectro-photometer at 450 nm. IL-6 concentration was calculated using an according standard curve.

Additional cytokine and chemokine measurements were conducted via Milliplex cytokine analysis due to the high number of analytes of interest.

2.2.8 MILLIPLEX CYTOKINE ANALYSIS

The Milliplex mouse high sensitivity t-cell panel (EMD Millipore) allows simultaneous quantification of even low levels of up to 18 analytes in a sample volume of 25 µl. For this analysis the following 14 customized analytes were tested: IFNy, IL-1β, IL-4, IL-6, IL-10, IL-12 p70, IL-13 and TNFα.

The Milliplex Map is based on the Luminex xMAP technology which used color-coded magnetic microspheres each of which coated with a specific capture antibody. The analytes from the samples are captured by the beads and tagged with a reporter molecule. The FLEXMAP 3D flow cytometer analyzed each bead but at least 50 of each to refer to the cytokine concentration in the sample. The cytokine analysis was carried out according to the manufacturer's instructions. Briefly, the wells were washed before standards, controls and samples were added. An assay buffer was additionally added to wells with sample solution. The magnetic beads for each analyte were sonicated and premixed before being added to all wells. After the overnight incubation at 4°C plate was washed and a detection antibody was added and incubated for another 1 h. Streptavidin-phycoerythrin solution was added on topand incubated again for 30 min. Before running, the plate was washed once again and sheath fluid was added. The plate was run on FLEXMAP 3D with the xPONENT software. The median fluorescent intensity (MFI) was measured and analyzed with the Belysa software (Merck) and GraphPad Prism version 9.4.2. Because of the built-in two-fold sample dilution, for all neat samples, the calculated concentrations needed to be multiplied by two. Although this method was repeatedly optimized for the specific samples in consultation with the manufacturer and performed under the supervision of the manufacturer's scientific specialists, it failed to produce sufficient usable data. Consequently, all further cytokine analyses had to be conducted using individual high-sensitivity ELISA kits.

2.2.9 siRNA

A small interfering RNA (siRNA) experiment was performed to determine which of the cannabinoid receptors, CB1, CB2 or GPR55, AbnCBD predominantly binds to and additionally confirm the specific ligand-receptor binding from GP1a to CB2 for the tissue culture model. This was tested under the influence of sham or 0.3 Gy X-ray radiation with a dose rate of 1.8 Gy/min. The controls were non-transfected siRNA and samples were no siRNA was added. The knock down of the receptors was monitored via real time PCR. Additional OHSC (2 per insert) were collected and treated as mentioned above to be used as a morphological pendant to the siRNA samples. All siRNA's were synthesized by Eurofins Genomics, Ebersberg, Germany.
C57BL/6J mice pups between the age of P3-P4 were sacrificed for OHSC extraction. Four OHSCs were cultivated on each insert in 6-well plates for 11-14 days with a full media exchange every third day. For the first of two siRNA treatments 5 µl GeneSilencer (GeneSilencer siRNA Transfection Kit, Genlantis) were diluted in 25 µl serum-free culture medium. 25 µl siRNA diluent was diluted in 15 µl serum-free medium and 1000 ng siRNA was added before the mixture was incubated for 5 minutes. For the transfection mixture, the diluted GeneSilencer and the diluted siRNA were combined, incubated for 12 minutes and added directly into the culture medium of each well. Plates were further incubated for 24 hours. This first addition of siRNA took place 24 h before irradiation. Shortly after irradiation the second dose of siRNA (1000 ng) and the ligands AbnCBD, GP1a and DMSO were added 1:2000 (10 µM) directly into the tissue culture medium. Plates were cultivated further for 12 h. Tissue culture medium was removed and OHSCs were fixed with cold RNAlater (Invitrogen) and stored at -20 °C. Morphological samples were fixed in 1:1 cold RNAlater and 4 % PFA for 24 h and subsequently stored in PBS until further analysis via confocal microscopy.

2.2.10 qPCR

All primers were synthesized by Eurofins Genomics, Ebersberg, Germany and diluted to 100 nM. Total RNA from four OHSC per condition was isolated using TRIzol reagent (Invitrogen). Briefly, RNAlater was removed, 700 µl Trizol was added, and the tissue was homogenized by mechanical shearing through a disposable cannula (Sterican) with a 0.55 mm diameter. After 15 min incubation at room temperature, 200 µl chloroform was added to separate the phases during the subsequent centrifugation for 15 min at 13.000 rpm at 4°C. The aqueous phase was collected and

520 µl ice cold isopropanol was added and incubated for 10 min at room temperature. After the RNA was precipitated the tubes were centrifuged at maximum speed (13.000 rpm) and the supernatant was discarded. The resulting pellet was gently washed with 520 µl ice cold 70 % (v/v) ethanol (EtOH) (Carl Roth) and centrifuged again. The supernatant was removed and 1000 µl EtOH (Carl Roth) absolute was added. After a further centrifugation step, as much supernatant as possible was removed from the pellet and it was dissolved in 10 µl nuclease free water. RNA concentration was quantified using the nano-photometer Pearl from Implen. At an absorption of 260 nm and 280 nm. The quotient of the measured absorption represents the purity of the RNA extracted and must be approximately 2.0 (optical density (OD) 260/280).

DNA digestion in the samples was performed using the TURBO DNA-free kit from Invitrogen according to manufacturer's manual. The RNA concentration was quantified again at OD 260/280. The reverse transcription of RNA to cDNA was conducted with the ProtoScript M-MuLV First Strand cDNA Synthesis kit from New England Biolabs. 1 µg/ml RNA was reverse transcribed according to manufacturer's instruction and stored at -20° C until qPCR according to manufacturer instructions.

2.2.11 Statistical analysis

Data from at least three independent experiments were expressed as mean value (± standard error of mean (SEM)). Data were statistically analyzed using one way ANOVA, followed by Bonferroni posttests. Results with $p < 0.05$ were considered as significant. Anylysis was conducted with Graph Pad Prism software version 10 for macOS (© 1994 - 2024 GraphPad Software, LLC).

3 RESULTS

The following sections describe radiation-induced changes within the microglia population in OHSCs after exposure to a single dose of X-rays or monochromatic ^{56}Fe-ion radiation (1 GeV/n). Detailed analyses were performed at multiple key time points following irradiation: 0.5 hours post irradiation, the short-term period spanning 12 to 48 hours, and the long-term period extending from 7 to 29 days post irradiation. Microglia were analyzed for various inflammatory markers and morphologically categorized. Additionally, two potentially neuroprotective substances, AbnCBD and GP1a, which are synthetic cannabinoid-receptor ligands to can CB1 and CB2, were tested for mitigating radiation-induced damage through the endogenous endocannabinoid system. The aim of these investigations is to provide a risk evaluation for future long-distance space missions and to investigate further protective measures to safeguard astronauts.

3.1 ORGANOTYPIC HIPPOCAMPAL TISSUE SLICE INTEGRITY AND CELLULAR COMPOSITION

Monitoring tissue integrity is crucial to ensure that observed effects are solely attributable to the applied treatments. Figure 6 presents representative examples of intact and necrotic OHSCs.

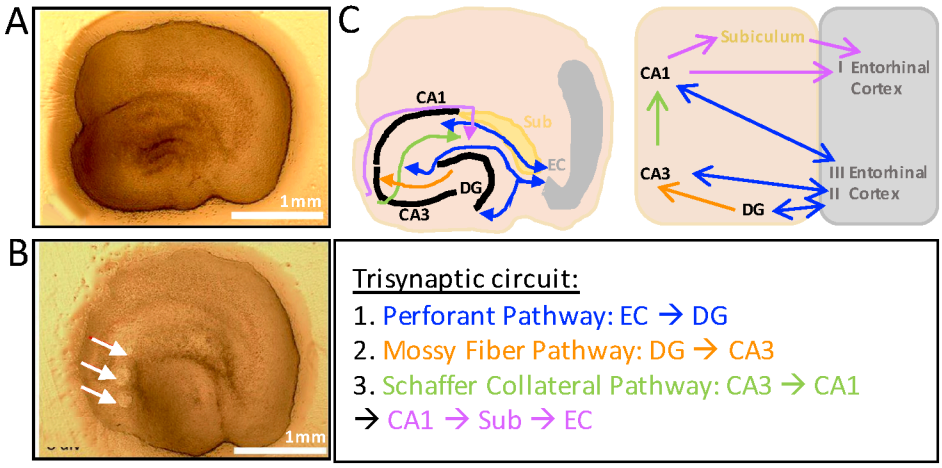

Figure 6 Structure, pathology, and circuitry of mouse hippocampal OHSCs. (A) Brightfield image of an intact OHSC showing the characteristic C-shaped morphology of the hippocampus. (B) OHSC exhibiting necrosis, with white arrows indicating necrotic tissue sections that disqualify the OHSC from further use. 350 µm thick OHSCs from P4 mice were cultivated on semipermeable inserts at an air-liquid interface (depicted here at 6-8 days in vitro (div)) and regularly monitored for integrity using transmitted-light microscopy at 4x magnification. Scale bar: 1 mm. (C) Schematic representations of hippocampal circuitry. Left: Detailed diagram showing major hippocampal subfields (CA1, CA3, DG) and associated regions (Subiculum, Entorhinal Cortex), with colored arrows indicating primary neuronal pathways. Right: Simplified circuit diagram illustrating connections between hippocampal subfields and layers of the entorhinal cortex (EC). Below: Trisynaptic hippocampal circuit. The perforant pathway (blue), mossy fiber pathway (orange), and Schaffer collaterals (green) connect the entorhinal cortex, dentate gyrus, CA3, and CA1, forming a key loop for memory processing and synaptic plasticity.

Figure 6A shows an intact OHSC with the characteristic C-shaped morphology of the hippocampus, suitable for further analysis. In contrast, the bottom row (Figure 6B) displays an OHSC with clear signs of cell necrosis in the CA3 region, indicated by white arrows. These necrotic areas increase in size over time and are irreversible once they appear. Consequently, only structurally intact OHSCs were used for subsequent investigations. Regular monitoring through transmitted-light microscopy allowed for continuous assessment of culture quality, ensuring that only healthy tissue slices were utilized for experiments. This rigorous quality control is essential to guarantee the reliability and reproducibility of results. The schematic diagrams in Figure 6C further illustrate the complex circuitry preserved in healthy OHSCs, underscoring the importance of maintaining tissue integrity for studying hippocampal function and connectivity *in vitro.*

To verify that the OHSCs exhibit a physiological response to the treatments, it is necessary for all cell types of the whole brain, to be represented within the OHSCs. The image sections depicted in Figure 7 exemplifies the presence of intact cell nuclei (DAPI), mature neuronal cell bodies (NeuN), astrocytes (GFAP), and microglia (IBA1) in the neuron-rich dentate gyrus region of an OHSC. For all further analysis DAPI staining's were employed and nucleus integrity was consistently monitored.

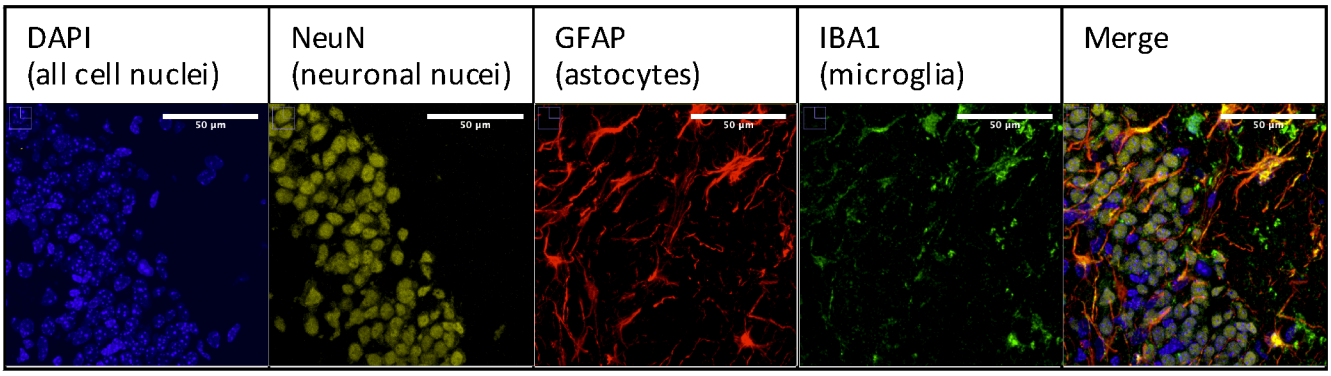

Figure 7 Immunofluorescent staining of relevant cell types in murine OHSC. OHSC cryo-sections with a layer thickness of 10 µm and immunofluorescence staining with a dye and antibody mix targeting: DAPI staining (cells nuclei, blue), NeuN (adult neuronal cell bodies, yellow), GFAP (astrocytes, red) and IBA1 (microglia, green). Images were taken with a Leica Microscope: 40x, zoom: 1.5, scale bar: 50 µm.

A comparison of microglia visualization techniques was used on differently processed tissue samples (Figure 7). Direct comparison of these staining methods revealed that the IBA1 staining method provides a more detailed staining of microglial processes. However, the lack of image depth prevents accurate quantification of these details. In contrast, the IB_4 staining method allows for three-dimensional observation of microglia (Figure 7). Methodologically, IBA1 immunofluorescence staining required brain samples to be sliced into 10 µm sections using a cryostat-microtome. This slicing of tissue sections was found to be unsuitable for accurate

morphological evaluation of microglia due to the difficulty in assigning the cell body to its processes after being cut through. Furthermore, the quality of the section was highly dependent on temperature-fluctuations, inside and outside the cryostat-microtome. These technical and infrastructural limitations eventually rendered the IBA1 method unsuitable for use for this study. In contrast, IB_4, a lectin substance derived from the seeds of *Griffonia simplicifolia*, can penetrate brain sections that have been cut with a vibratome and are up to 350 µm thick. This method is suitable for staining microglia and blood vessels in thicker tissue sections, which is advantageous for additional integrity control of OHSCs. Therefore, IB_4 was employed for microglia visualization in all subsequent experiments.

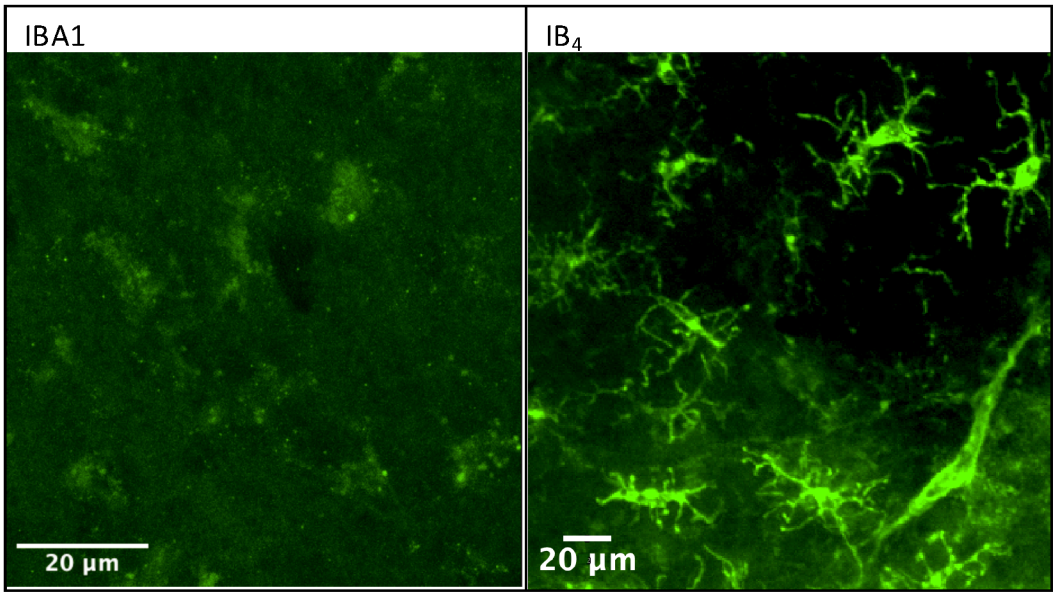

Figure 8 Comparison of microglia markers IBA1 and IB_4 in murine (wt) tissue. Left: IBA1 (microglia, green) immunostaining was performed in 10 µm cryo-slices. Right: IB_4 staining (microglia, green) in whole mount OHSCs to visualize microglia. The images represent a maximum projection of a total stack thickness of 28 µm. Zoom: 300 %, scale bar: 20 µm.

Figure 8 demonstrates an examplification of the IB_4-stained hippocampal sections. It is noticeable that the blood vessels (red arrows) and microglia (IB_4, green) are both IB_4-stained and exhibit similar color intensity, which makes automated distinction based on size and intensity challenging, particularly when the sectioning orientation (transverse or longitudinal) is considered. As a result, automated evaluation of the images was not feasible, and manual measurement and assessment of microglia was required for all experiments.

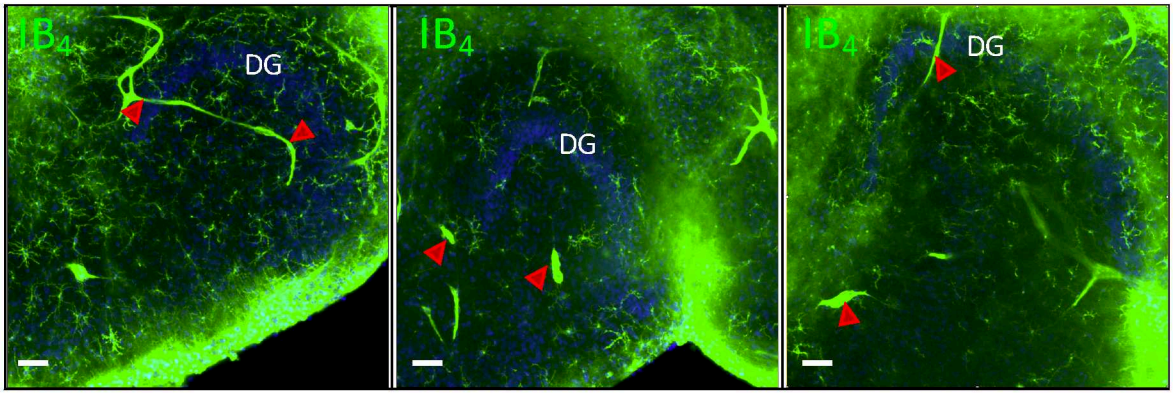

Figure 9 IB_4 staining of microglia and blood vessels in dentate gyrus of whole mount OHSC. The co-stained blood vessels traverse all relevant hippocampal regions and have a similar color intensity as microglial cells. The red arrows indicate blood vessels that are incised differently (transversely or longitudinally). Scale bar: 50 µm.

3.2 Classification of Microglia

Microglia constantly survey the CNS for signs of damage and exhibit dynamic morphological transformations and associated functional adaptations in response. As a result, various microglia morphologies have been identified. However, a consensus on the nomenclature and definition of these morphologies is still being discussed in the relevant literature. To address this issue and evaluate the radiation effects on a cellular level, three morphological classes were defined for this work – 'ramified', 'reactive', and 'amoeboid' – based on measurements of morphological parameters obtained from a dataset comprising 1647 manually measured microglial cells from all conditions in OHSCs, in collaboration with Dr. Karsten Winter from the University of Leipzig (Figure 10F-H). The parameters measured in our definition of the morphological classes include soma area, number of primary branches, and territorial area of each microglia cell. The classification was established based on previously defined robust criteria from the literature, which are commonly accepted.

The classification was performed by analyzing the manually measured microglia population, aiming to provide an overall impression of the morphological differentiation possibilities (Figure 10). This was conducted with Nearest Centroid (NC) classification methods, which includes an optimization of cluster learning algorithms. To this end, a set of cells was manually assigned to one of the three morphological classes (labeling) to define feature spaces. A feature space is a mathematical representation of the distinct attributes or features of an object. In this study, morphological parameters, soma area, territory area, and number of primary branches were used as features to represent each microglia cell. Initially, feature spaces were created in two dimensions (not shown). However, this initial approach, which relied on the combination of only

two parameters, was not sufficient to perform accurate classification. Therefore, the analysis was expanded to a three-dimensional space, which considered all three parameters to capture the variability in the data optimally. Scatter plots for parameter values of all cells were generated using a color scheme for the indication of the three classes: ramified microglia in blue, reactive microglia in green, amoeboid microglia in red.

Once the feature spaces were created, the center point (centroid) of each class was calculated, which represents the average position of all the points in a feature space that belong to a particular class (Figure 10D-E, black dots). The centroids serve as a reference point for classification and represents the typical characteristics of a class. To classify the unlabeled microglia dataset into one of the three classes, the triplet of parameters was compared with the centroids', with subsequent labeling. Once a new cell is assigned to a feature space, the feature space is updated, and its centroid is repositioned. This process is repeated until the best possible assignment of all cells is achieved to increase the performance of the NC classification.

3.2.1 DEFINITION OF MORPHOLOGICAL AND FUNCTIONAL MICROGLIA CLASSES

For each morphological class the variance of the parameters was plotted (Figure 10A-C). The classification included a population of ramified microglia, which were identified by soma sizes with a median of approximately 90 μm^2 and a median territory area of approximately 1400 μm^2 and 5 primary branches (Figure 10H, blue). The ramified microglia population was identified with the smallest soma size and the biggest territory area centroids of the three classes (Table 3).

The reactive population was identified by intermediate soma areas (centroid = 105.69 μm^2) and median territory area around 1100 μm^2 (Figure 10G, green). The branching also resulted in a median of 5 primary branches (Figure 10C). A direct cell-cell contact with several surrounding cells through their extensions was observed in these microglia. At the time of recordings, most of these cells were observed to engulf another cell using their processes (Figure 10G, indicated by white arrow).

The third class of microglia, the amoeboid microglia, have a round soma area centroid of 115.51 μm^2 and median territory areas of 990 μm^2 (Figure 10B). Although they also formed the beginnings of several primary processes, these processes ended close to the cell body, resulting in a significant reduction of the territorial size of the cell (Figure 10F, indicated by white arrows). Within the three-dimensional feature spaces, each microglia was assigned to one of the classes so that a 'sharp-edged' separation of the classes was available (Figure 10E). Represented as convex

hulls containing all cells of the class and their respective characteristic centroids, this method allowed a differentiation of the classes. With this analysis the territorial and soma size were found to be the most differentiable parameter between the microglia populations (Table 3).

Table 3 Centroid values of morphological microglia classes for soma area, territory area and number of primary processes from NC analysis.

Class name	Soma area [µm²]	Territory area [µm²]	Primary branches
Ramified	76.438	2152.374	5
Reactive	105.694	1751.998	5
Amoeboid	115.508	408.705	4

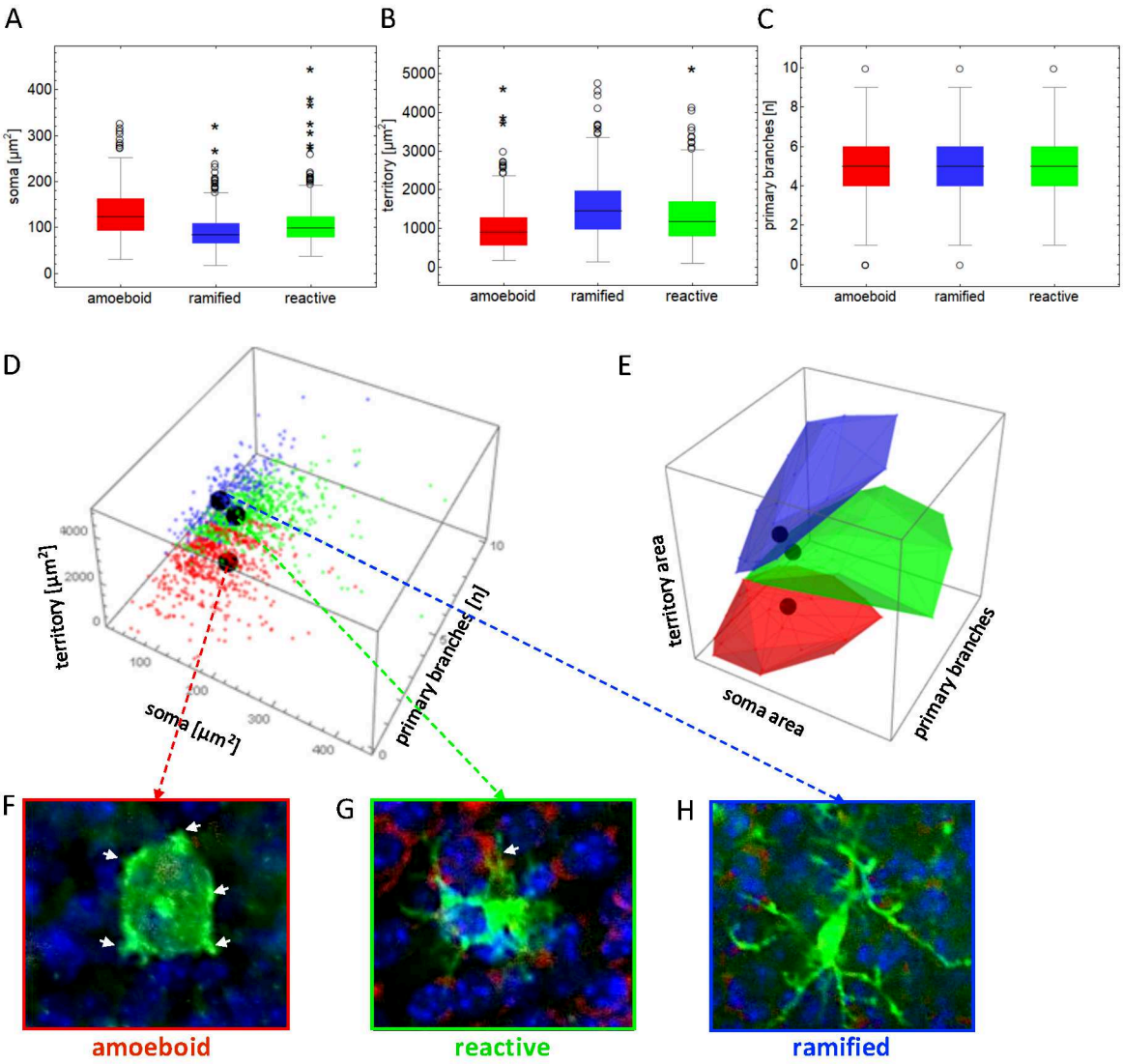

Figure 10 Nearest centroid classification analysis reveals distinct morphological parameters of microglial phenotypes. (A-C) Box plots displaying the distribution of morphological parameters from 1647 manually classified microglia: (A) soma area, (B) territory area, and (C) number of primary branches. Boxes represent 25-75th percentiles, whiskers extend to minimum and maximum values excluding outliers, horizontal lines indicate medians. Outliers are shown as individual points (*$p < 0.05$). (D) Three-dimensional scatter plot illustrating the distribution of individual microglia based on soma area, territory area, and number of primary branches. Black dots represent class centroids derived from nearest centroid classification analysis. (E) Three-dimensional visualization of morphological parameter space using convex hulls to demonstrate the clustering of microglial phenotypes, with centroids indicated as black dots. (F-H) Representative immunofluorescence images of the three microglial classes: (F) amoeboid (red frame), characterized by enlarged soma and few processes (white arrows), (G) reactive (green frame), showing intermediate morphology, and (H) ramified (blue frame), displaying extensive branching characteristic of surveillance state. Microglia are labeled in green, nuclei in blue, and white arrows point to branches.

3.3 OHSCs as a Model System For Radiation Damage and Inflammation Mitigation

OHSCs can provide a valuable model system for studying the effects of IR on the brain. The tissue cultures consist of self-contained, three-dimensional neuronal tissue and closely resemble the native microenvironment of the brain, representing the cellular interactions and signalling pathways of the *in vivo* situation more accurate.

Each OHSC contains the complete hippocampal formation incorporating the DG, hilum and CA1- to CA3 regions including the associated connected subiculum and entorhinal cortex as described in section 1.4. The present study focused on the investigation of the dentate gyrus region only, as the sub-granular zone within this region is where neurogenesis occurs and is therefore especially vulnerable to damage caused by radiation.

The planned schedule of the beam time experiments and the ultimate outcome of the analysable OHSCs that survived each designated cultivation and treatment are presented in the table below (Table 4). Littermates were used for one experiment, and OHSCs from the animals were pooled and divided among the experimental conditions of dose and treatment. However, not all litters contained enough animals or yielded sufficient OHSCs to be consistently divided among experiments. Consequently, 'excess' OHSCs were assigned to other experiments. A total of 528 OHSCs were prepared from 83 animals. The average number of dissected OHSCs per animal ranged between 4.3 and 7.5 OHSCs per animal. These fluctuations resulted partly due to technical conditions and the brain-size difference of the littermates.

Table 4 Experimental setup for ^{56}Fe-ion and X-ray irradiation. The number of inserts depends on the number of animals in a litter.

Beamtime	Experiments	Planned experimental period	Dose	Litter	# Animals	# Inserts	# OHSC (total/ analyzed)
^{56}Fe	1	short + long term	0 Gy, 0.3 Gy	1	11	26	78/ 76
^{56}Fe	2	short + long term	0 Gy, 0.3 Gy	2	10	26	78/ 74
^{56}Fe	3	short term	0 Gy, 0.3 Gy	4	6	14	42/ 41
^{56}Fe	4	short term	0 Gy, 0.3 Gy	2	6	14	42/ 41
^{56}Fe	5	0.5 h + 7 d	0 Gy, 0.3 Gy	1	4	8	24/ 22
^{56}Fe	6	0.5 h + 29 d	0 Gy, 0.3 Gy	3	3	8	24/ 24
^{56}Fe	7	0.5 h + 12 h	3.0 Gy	4	2	4	12/ 12
Total	7			4	42	100	300/ 278
X-ray	1	short term	0 Gy, 0.3 Gy	1	7	14	42/ 39
X-ray	2	short term	0 Gy, 0.3 Gy	2	8	14	42/ 41
X-ray	3	short term	0 Gy, 0.3 Gy	3	7	14	42/ 41
X-ray	4	long term	0 Gy, 0.3 Gy	4	7	10	30/ 29
X-ray	5	long term	0 Gy, 0.3 Gy	5	6	12	36/ 34
X-ray	6	long term	0 Gy, 0.3 Gy	1	4	8	24/ 24
X-ray	7	0.5 h + 12 h	3.0 Gy	2+3	2	4	12/ 12
Total	7			5	41	76	228/ 220

3.4 SHAM IRRADIATION

3.4.1 CELL SURVIVAL IN SHAM IRRADIATED OHSCS

The sham transport controls to the X-ray tube or the heavy-ion accelerator for the ^{56}Fe-ion irradiation are referred to as sham X-ray or sham ^{56}Fe controls.

The viability assessment of OHSCs was investigated by a nucleus staining (DAPI) and microglia staining (IB_4) to determine the total cell number and microglia density in sham irradiated X-ray and ^{56}Fe-ion sham controls (Figure 11A, Figure 11B).

The analysis of the total cell numbers revealed no significant difference between the sham irradiated controls of X-ray or ^{56}Fe ($p = 0.81$). Both sham controls resulted in mostly equal cell numbers from 0.5 hours to 7 days. From day 7 to day 29, cell numbers within sham X-ray OHSCs increase significantly ($p = 0.04$) to a mean cell count of 585.0 ± 26.0 and thereby create a non-significant difference to sham ^{56}Fe irradiated OHSCs (385.7 ± 118.9) due to the high variance in the latter samples (Figure 11A). The density of microglia in both sham control groups was approximately 350 cells per square millimeter (n/mm^2) 0.5 hours after transport to their respective irradiation units. At the 12-hour mark, the group transported to the X-ray unit maintained stable microglia density, while OHSCs moved to the heavy-ion accelerator room exhibited a significant reduction in microglia density (Figure 11B). By 48 hours, an increase in microglia density was observed in both sham controls; however, this increase was only statistically significant in the sham ^{56}Fe group. On the seventh day, there was a non-significant decrease in microglia density in the sham X-ray samples, which remained consistently low through the 29-day measurement period, staying below the initial density recorded at 0.5 hours. In contrast, the ^{56}Fe sham controls showed a reduction in microglia density at the long-term measurement points, though this reduction was less pronounced compared to the sham X-ray group.

While the absolute cell count remained relatively constant over the entire 29-day test period, the microglia density exhibited temporal fluctuations. These fluctuations were observed at several key intervals: within the initial 12 hours, at the 48-hour mark, and throughout the subsequent long-term measurement period.

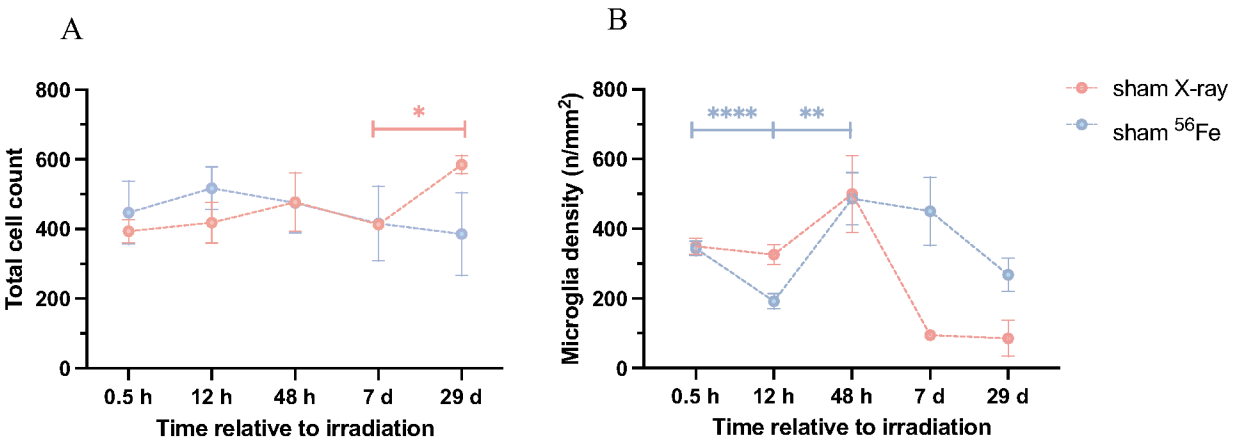

Figure 11 (A) Absolute cell numbers in the dentate gyrus region of OHSCs after sham irradiation (X-ray or ^{56}Fe-ion). (B) Density (n/mm^2) of microglia cell population in dentate gyrus after sham irradiation. Cell numbers were determined by a DAPI staining and microglia by IB_4 staining of 20 µm OHSCs and images were taken with Olympus confocal microscope and analyzed in ImageJ/Fiji. Error bars depict mean with SEM. N = 3, I =3, s = 9. Statistics performed by unpaired t-test with Welch's correction. *p < 0.05, **p < 0.001, ****p < 0.0001.

3.4.2 Inflammatory cytokines in sham irradiated OHSCs

To analyze the cytokines secreted following sham radiation into the culture supernatant, multiple experiments were performed using the magnet-bead based Mouse High-Sensitivity T-CellMultiplex Assay (Merck KGaA) to measure 18 customized pro- and anti-inflammatory cytokines simultaneously. However, even after various methodological adjustments and technical support from the manufacturer, only one of the eighteen cytokines yielded values above the threshold. This method was therefore eliminated, and subsequent cytokine measurements were limited to IL-6 (pro-inflammatory) and IL-4 (anti-inflammatory) in the supernatant using high-sensitivity ELISA assays. Since IL-4 concentrations were below the assays' threshold in all samples, IL-6 was used as an inflammatory marker in all subsequent experiments.

The inflammatory baseline of the slices was determined prior to and following irradiation at the respective radiation facility. IL-6 concentrations were generally low, and no statistically significant differences were observed between sham X-ray and sham ^{56}Fe OHSCs at all experimental time point (Figure 12). However, it was observed that the IL-6 concentrations in the sham X-ray irradiated slices remained elevated for extended periods of cultivation, compared to those in the sham ^{56}Fe irradiated slices.

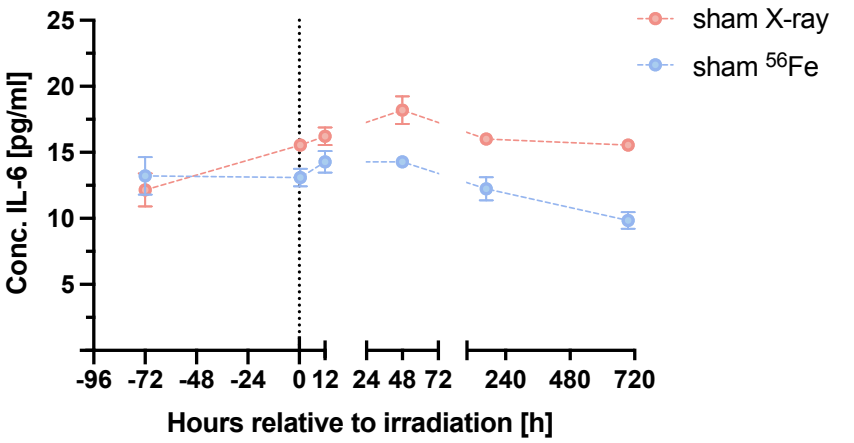

Figure 12 IL-6 concentration in tissue-culture supernatant of sham (X-ray or ^{56}Fe) irradiated OHSC. The concentration of the pro-inflammatory marker IL-6 was measured using a highly sensitive ELISA assay. The accumulation of IL-6 was determined for each measurement time point after 72 hours of cultivation time. N = 3, i = 3, s = 9. Means ± SEM. Statistics performed by unpaired t-test with Welch's correction, comparing the irradiation conditions at each time point.

3.4.3 Effects of synthetic cannabinoid-receptor ligands on sham irradiated OHSCs

The cannabinoid-receptor ligands GP1a and AbnCBD can potentially mitigate irradiation-induced damage. The protective effect can be inferred from a reduced count of propidium iodide-stained cell nuclei (PI+ cell nuclei), as PI only enters dead or membrane-compromized cells. In a preliminary experiment, a non-toxic concentration of 10 µM/mL GP1a or AbnCBD was determined in accordance with current literature and was used in the experiments of this work. The application of cannabinoid-receptor agonists occurred promptly following irradiation (~ 0.5 hours post irradiation), resulting in the earliest measurement time available being 12 hours post irradiation. Cannabinoid-receptor ligands were added to the medium during each media change, every third day. DMSO was used as a solvent control.

The results of the following study showcase the effects of 10 µM GP1a or AbnCBD on microglia and PI+ cell density in sham irradiated OHSCs (Figure 13). The sham X-ray irradiated OHSCs treated with either 10 µM GP1a or AbnCBD are shown to follow a similar trend of microglia density over time (Figure 13A). Both treatments display a microglia density as the control group at 12 hours and drop below the DMSO control at 48 hours with a mean difference of 175.61 ± 42.08. At 7 days the microglia densities of the treated samples remain slightly higher than of the control group post sham X-ray irradiation. At 29 days post sham irradiation all treatments show a microglia density below 200 n/mm^2.

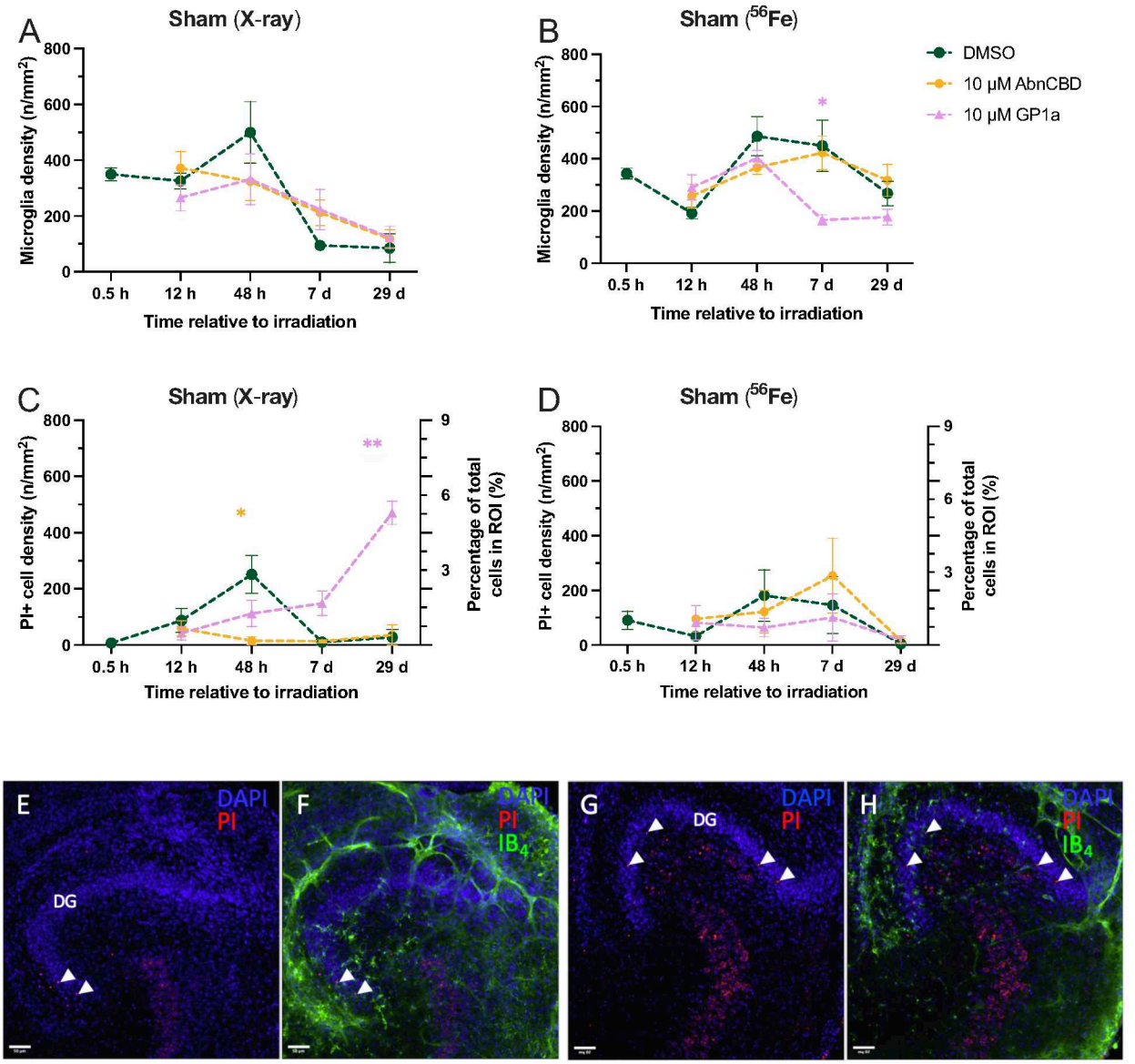

Figure 13 Microglia and PI+ cell density in dentate gyrus of sham irradiated OHSC treated with 10 µM AbnCBD or GP1a. Cell numbers were measured in immunofluorescent images and correlated to the area (mm^2) of the associated dentate gyrus region to determine cell density (n/mm^2). Microglia densities for (A) X-irradiated OHSCs and (B) ^{56}Fe-ion irradiation in. The density of PI + cells after (C) X-ray irradiation and (D) for ^{56}Fe-ion irradiation. Immunofluorescent images (E – H) show examples of DG regions with PI + cells (PI, red, marked with arrows) and (F, G) additionally show microglia (IB_4). Scale bars: 50 µm. Mean ± SEM for N = 3, i = 3, s = 9 samples. Statistics performed by unpaired t-test with Welch's correction, comparing each group to the DMSO control at the associated experimental time point. * $p < 0.05$, ** $p < 0.001$.

The microglia density of sham ^{56}Fe irradiated samples is shown in Figure 13B. OHSCs treated with 10 µM AbnCBD showed marginally higher microglia densities at 12 hours and a lower microglia density at 48 hours compared to the control group. The density increased over time and remained slightly higher than the control group 29 days after sham irradiation. On the other hand, GP1a

treatment reduced the microglia density significantly at 7 days ($p = 0.03$, mean diff. = 284.13) post sham irradiation and remained lower than the control and AbnCBD group at 29 days.
The PI+ cell density in the dentate gyrus of DMSO treated OHSCs (Figure 13C and Figure 13D) paralleled the microglial density increase at 48 hours in Figure 13A, followed by a statistically non-significant decrease from 48 hours to 7 days for sham X-ray. At 48 hours, the peak of cell death in DMSO controls accounted for approximately 4 % of all cells (right Y-axis) in the DG (Figure 13C). The addition of AbnCBD resulted in a significantly lower cell death at this time point ($p = 0.04$) and remained at minimum levels over time. In contrast, GP1a treatment was associated with a constant increase of cell death, which was significantly higher than the control and AbnCBD at day 29 ($p = 0.002$). Sham ^{56}Fe irradiated OHSCs, however, did not show any statistically significant differences of cell death, regardless of the treatment (Figure 13D). Each of the three groups demonstrated a high level of variance at both 48 hours and 7 days and ultimately reaching a minimum average of 12.88 ± 8.44 by day 29. Confocal immunofluorescence images of PI+ cells and microglia are shown as examples in Figure 13E to Figure 13H, providing an overview of the distribution and size ratio of these cell types. Examples of PI + cells are represented in image are marked with a white arrow. Examples of IB_4-stained microglia are depicted in green in Figure 13F and Figure 13H.

To further investigate the inflammatory baseline, IL-6 high-sensitivity ELISA analysis of cannabinoid-receptor-ligand-treated OHSCs was performed (Figure 14). This experiment aimed to demonstrate the inflammatory or mitigating effects on intact tissue. Therefore, the sham irradiated tissue was observed over a period of 29 days (696 hours). The baseline measurement was taken 72 hours prior to any treatment and before OHSC transportation to the radiation facilities. The second measurement time point, 0.5 hours, included measurement of IL-6 in DMSO treated OHSCs as well as the addition of the cannabinoid-receptor agonist to the associated groups (Figure 14A and Figure 14B). The initial measurement with cannabinoid-receptor ligand was taken at the 12-hour time point.

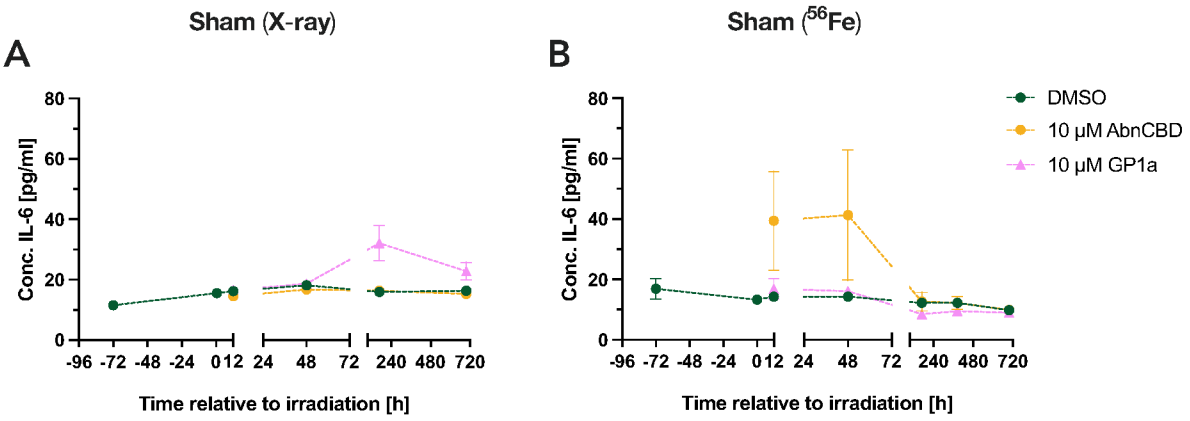

Figure 14 IL-6 concentrations in sham irradiated OHSCs treated with 10 µM AbnCBD or GP1a. The concentration of the pro-inflammatory marker IL-6 was measured using a highly sensitive ELISA assay. The accumulation of IL-6 was determined for each measurement time point after 72 hours of cultivation time. N = 3, i = 3, s = 9. Means ± SEM. Statistics performed by unpaired t-test with Welch's correction, comparing the irradiation conditions at each time point.

As shown before in Figure 12, sham irradiated, DMSO control OHSCs increased IL-6 secretion in the first 48 hours compared to the baseline concentration (72 h before sham irradiation). The IL-6 secretion in the group treated with 10 µM AbnCBD was comparable to the control group over the entire application phase (Figure 14A). In contrast, the GP1a treated samples depicted a non-significant increase in IL-6 concentrations in the long-term observations in sham X-ray irradiated OHSCs.

The IL-6 concentrations in the supernatant of sham ^{56}Fe irradiated OHSCs (Figure 14B) were similar in the DMSO control group and the group treated with 10 µM GP1a. Conversely, a non-significant increase in IL-6 concentration was observed in the short-time data points of AbnCBD treated OHSCs compared to the DMSO group, creating an opposing picture to the sham X-ray irradiated OHSCs and AbnCBD-treated OHSCs.

To investigate whether the administered receptor ligands bind to one of the cannabinoid receptors of the endocannabinoid system and modulate their activity, an RNA interference (RNAi) experiment was conducted. For this purpose, multiple small interfering RNA (siRNA) primers were designed and utilized against the mRNA of the three endogenous cannabinoid receptors CB1, CB2 and GPR55. The objective of inhibiting the protein synthesis of the receptors was not achieved within this experiment. Due to complications in designing suitable primers. Thus, a definitive conclusion could not be made regarding which of the receptors the administered agonists, GP1a and AbnCBD, bind to (data not shown).

3.5 Impact of X-ray Irradiation on Microglia

The preceding sections have provided a presentation of the analytical methods used in this study on sham irradiated samples. In subsequent sections, cultured OHSCs were irradiated with X-rays, treated with the cannabinoid-receptor ligands and various inflammatory expression characteristics were analyzed as previously described.

3.5.1 Cell survival in OHSCs post 0.3 Gy X-ray irradiation

To assess the viability of OHSCs subjected to 0.3 Gy X-ray radiation, DAPI staining was employed to determine the total cell number, compared to the corresponding sham irradiated controls (Figure 15).

The findings from the cell count analysis revealed a similar pattern of progression in the total cell count over time between sham X-ray, and the OHSCs exposed to 0.3 Gy X-ray irradiation. Yet, the average total cell count observed in the DG region of the sham irradiated OHSCs was consistently slightly higher (457.27 ± 43.06) compared to the cell count of X-ray irradiated samples (404.800 ± 64.277). On day 29, a statistically significant rise ($p = 0.04$) in total cell count within the DG was exclusively observed in the sham irradiated samples, while the 0.3 Gy X-ray irradiated OHSCs did not exhibit this increase but a high variance at the late time data points (Figure 15).

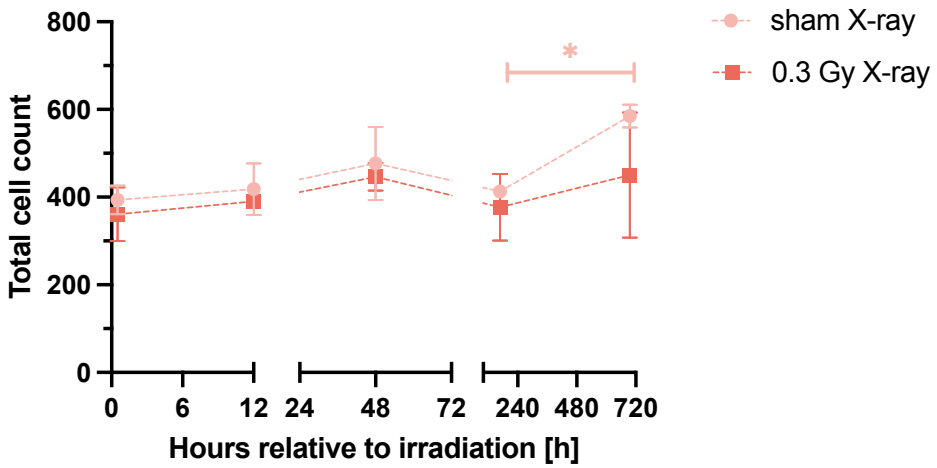

Figure 15 Total cell number in dentate gyrus of sham and 0.3 Gy X-irradiated OHSC. Cell numbers were determined by DAPI staining of 350 µm whole mount OHSCs. Mean ± SEM. N = 3, i = 3, s = 9. Statistics performed by unpaired t-test with Welch's correction, comparing irradiated samples at each time point to sham irradiated OHSC at associated experimental time point. *$p < 0.05$.

3.5.2 SPATIOTEMPORAL DYNAMICS OF MICROGLIAL POPULATION AND CELL DEATH IN THE DENTATE GYRUS FOLLOWING X-RAY EXPOSURE

Microglial cells, serving as the primary immune mediators within the CNS, exhibit rapid responsiveness to pathological alterations through swift migration to affected regions within minutes of insult. This characteristic renders microglial density a valuable indicator of both localized and global tissue integrity. To evaluate radiation-induced tissue damage, we conducted simultaneous quantification of microglial populations and PI+ cells. Representative immunofluorescence micrographs of the DG region (ROI, magenta) are presented in Figure 16A-C, illustrating IB_4-positive microglia (green) and DAPI-stained nuclei (blue). Microglial somata and their territorial domains were delineated (white outlines) for morphological classification, with additional microglia identified by magenta circumscription. PI+ cells were marked with white diamonds for automated quantification (Figure 16B-C). The ROI was precisely defined to ensure exclusive enumeration of microglia and PI+ cells within the designated area (Figure 16B). Cell counts were normalized to ROI area, yielding density measurements (n/mm^2) as depicted in Figure 16D-F and subsequent analyses.

Comparative analysis of microglial population density and cell death in the dentate gyrus between sham-irradiated controls and specimens exposed to 0.3 Gy X-rays revealed distinct temporal patterns (Figure 16D). Sham-irradiated specimens exhibited a significant reduction ($p= 0.02$) in microglial density between 48 hours and 7 days post-treatment. Peak microglial density (499.59 n/mm^2) occurred at 48 hours, constituting approximately 7.5 % of the total cellular population within the ROI. X-ray-exposed specimens demonstrated reduced microglial presence during the short-term phase of 12 hours and diminished cell death at 48 hours post-irradiation relative to controls. Notably, a 300-fold elevation in microglial density was observed 7 days post-irradiation, although high variability precluded statistical significance (Figure 16E). Microglial density reached its nadir at 29 days post-exposure. While X-ray-exposed specimens generally exhibited reduced cell death compared to controls, a marked exception occurred at 0.5 hours post-irradiation, characterized by a 50-fold increase in cell death rate (Figure 16F).

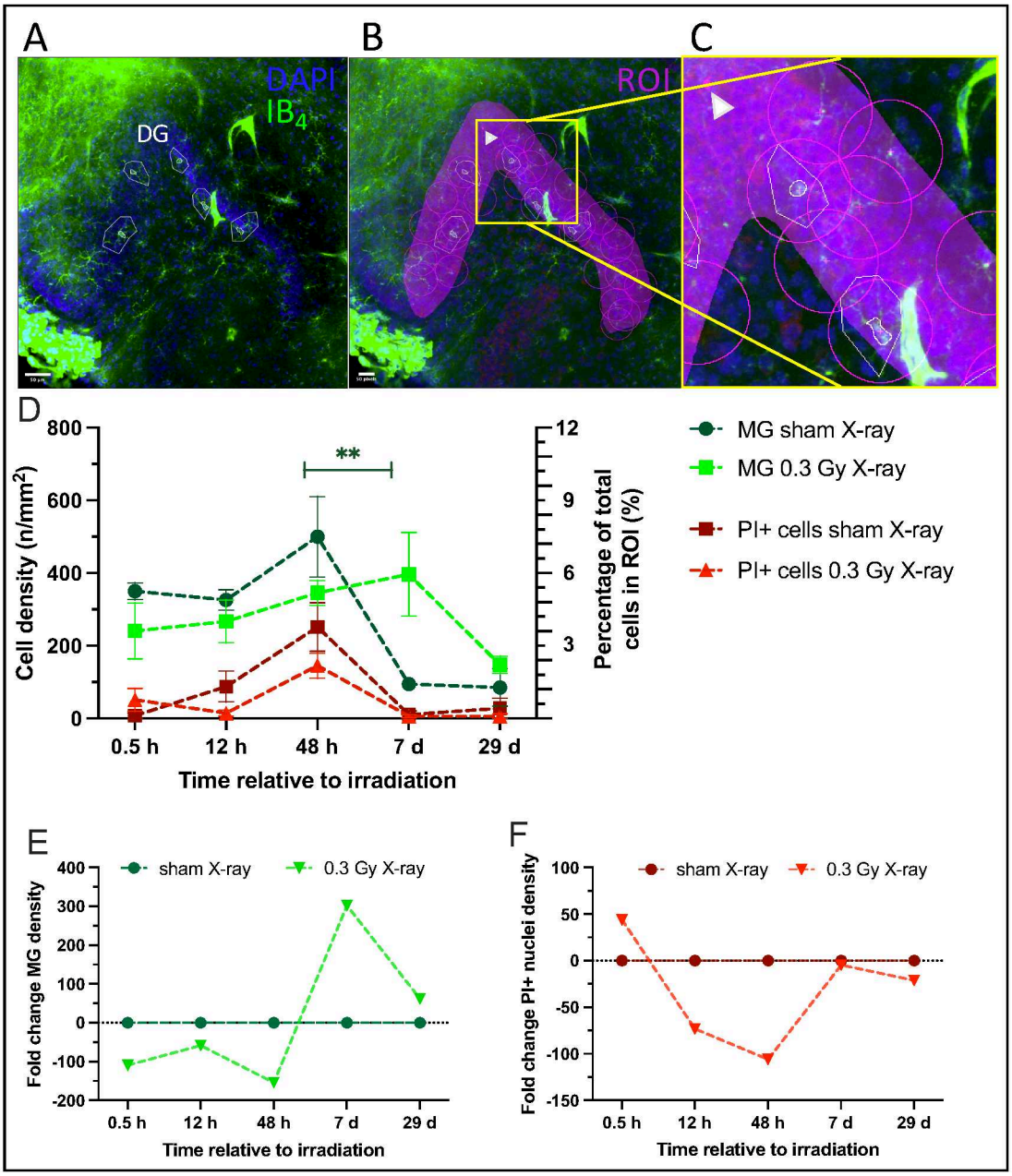

Figure 16 Analysis of microglial density and cell death in the dentate gyrus following X-ray exposure. (A) Representative immunofluorescence micrographs showing IB_4-positive microglia (green) and DAPI nuclear staining (blue) in the dentate gyrus (DG), with individual microglia delineated (white outlines). (B) Region of Interest (ROI, magenta) demarcation of the dentate gyrus shown in (A), with PI-positive cells (white arrowhead) and microglia (magenta circles with central cross) identified for quantification. (C) Magnified view of the ROI highlighted in (B). (D) Quantitative analysis of microglial and PI-positive cell densities following sham or 0.3 Gy X-ray exposure over a 29-day time course. Cell densities were calculated as cells per mm^2 of dentate gyrus ROI area. (E) Temporal changes in microglial density expressed as fold change relative to time-matched sham controls. (F) Fold change in PI-positive cell density relative to sham controls across the experimental timeline. Data are presented as mean ± SEM (N=3 independent experiments, i=3 internal replicates, s=9 total samples). Statistical significance was determined using unpaired t-tests with Welch's correction comparing irradiated samples to time-matched sham controls (**$p < 0.001$).

3.5.3 DYNAMIC MORPHOLOGICAL TRANSITIONS IN MICROGLIAL POPULATIONS FOLLOWING LOW-DOSE X-RAY EXPOSURE IN OHSCS

Exposure to X-rays can induce a range of effects in the CNS, including increased inflammatory signals. One potential mechanism underlying these effects are the dynamic morphological changes that microglia cells undergo in response to injury or damage in the CNS. As immune cells of the CNS, microglia continuously survey their environment and respond with dynamic morphological activation, which can have functional consequences. The microglia morphologies in response to IR exposure over a 29-day period were classified and analyzed to comprehend changes in microglia phenotype and function (Figure 17A and Figure 17B). The absolute cell numbers are presented above each bar.

The proportion of amoeboid microglia increased 0.5 hours after X-ray exposure whereas the ramified microglia population decreased compared to the sham irradiated samples (Figure 17A). At 12 hours post irradiation, a nearly equal number of microglia from all three classes are observed in both irradiated and sham irradiated OHSCs. Forty-eight hours post irradiation, the highest proportion of amoeboid microglia is found in both conditions, with almost no ramified microglia identifiable. The consistent proportions of the classes are still present after 7 days, although fewer amoeboid microglia are found than at 48 hours post irradiation. Only 29 days after X-rays, differences were observed between the compared conditions. In X-ray irradiated samples the proportion of amoeboid microglia was lower than the controls whereas more reactive and ramified were to be found.

To provide a more comprehensive analysis of the microglia response, the cell numbers of each microglia class were normalized to the total numbers of microglia counted in each sample. The class shares were then plotted in comparison to the sham irradiated control at the same time point to reveal the relative changes in microglia class (Figure 17C and Figure 17D). In cases where the cell number for a specific morphological class was zero, a limit value of 0.1 was assumed for the purpose of calculation and analysis (limit value consideration). This Temporal analysis of morphological transitions relative to sham controls revealed distinct patterns in both acute and chronic phases post-irradiation. During the acute phase (0.5h – 48h), amoeboid morphology exhibited an initial increase (+100 %) at 0.5 hours post-exposure, followed by a progressive decline to baseline levels by 48 hours (Figure 17C). Conversely, reactive and ramified populations showed early decreases (-25 % and -75 % respectively) at 0.5h, with reactive morphology demonstrating a modest recovery (+50 %) by 48 hours. The chronic phase response (7d – 29d) was characterized by pronounced morphological redistribution (Figure 17D). Most notably, the

ramified population exhibited a substantial increase (+300 %) at 29days post irradiation, while the amoeboid population showed a consistent decline to approximately - 50 % below control levels. The reactive phenotype displayed a gradual increase, reaching +50 % above control levels at 29 days. These temporal dynamics suggest a radiation-induced shift from acute inflammatory responses (amoeboid) toward tissue surveillance states (ramified) during the chronic phase.

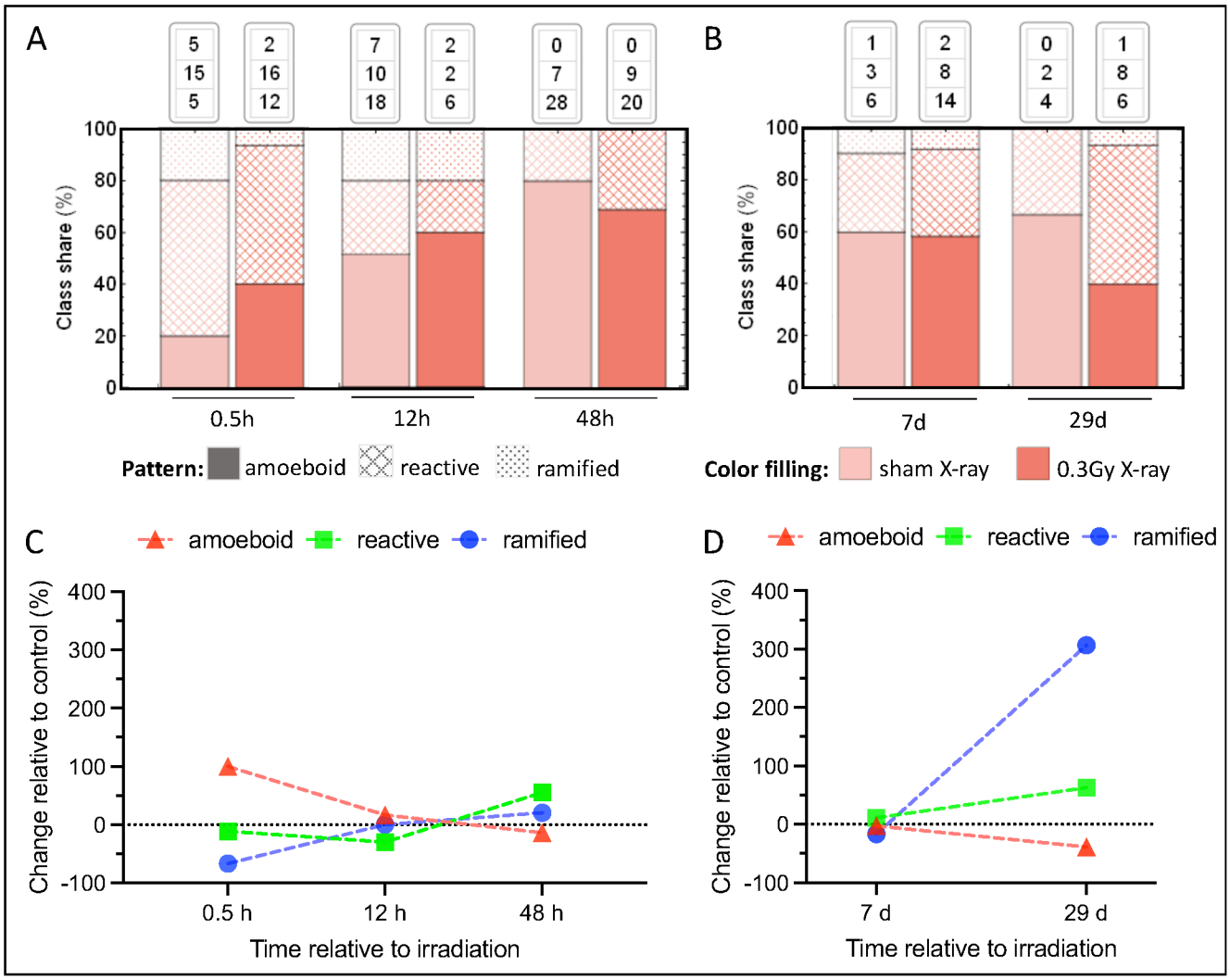

Figure 17 Quantitative assessment of microglial morphological phenotypes post-X-ray exposure. (A-B) Distribution of microglial morphological states (ramified, reactive, and amoeboid) expressed as percentage of total population in OHSCs following sham or 0.3 Gy X-ray exposure. (A) Acute phase response (0.5-48h) showing temporal shifts in morphological distribution. (B) Chronic phase response (7-29d) demonstrating sustained morphological alterations. Numerical values above columns represent absolute cell counts per morphological class (n=3-4 independent experiments, total of 9 OHSCs, 6-45 microglia per experimental condition). (C-D) Temporal dynamics of morphological transitions expressed as percentage change relative to time-matched sham controls for (C) acute and (D) chronic phases post-irradiation. Morphological classification was performed using a semi-automated approach with manually curated training datasets (100 cells per morphological category). Pattern designations: amoeboid (solid gray), reactive (cross-hatched), and ramified (dotted). Color scheme: sham X-ray (light pink) and 0.3 Gy X-ray (coral). This systematic morphological characterization provides quantitative insights into the temporal dynamics of microglial activation states following low dose IR exposure.

3.5.4 Inflammatory cytokine IL-6 in X-ray irradiated OHSCs

For the evaluation of the inflammation potential of X-rays, the pro-inflammatory marker IL-6 was measured with a high-sensitivity ELISA assay.

X-ray irradiation decreased the IL-6 concentration in the tissue culture supernatant indicating an additional hallmark feature of inflammation (Figure 18). Prior to irradiation (-72 h, baseline), a mean IL-6 concentration of 11.58 pg/mL (SD ± 2.70) was determined (Figure 18A). Starting at 48 hours after radiation, significantly reduced levels of IL-6 in the low-dose X-ray irradiated OHSCs were detected, which continued throughout the entire measurement period and even fell below the initial baseline level upon irradiation (Figure 18A and Figure 18B). Despite the observed statistical significance of the differences, the magnitudes of the effect sizes are relatively small, typically in the range of 10 pg/mL. Therefore, the biological relevance of these differences requires careful consideration and further discussion.

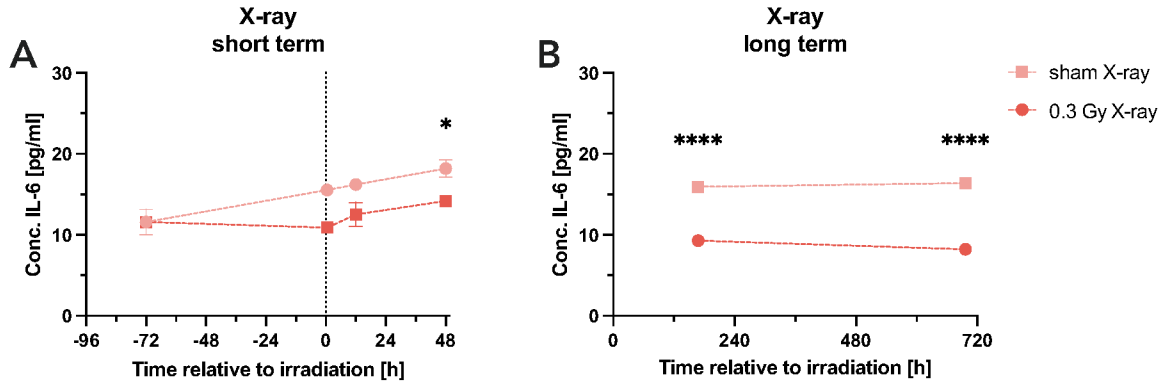

Figure 18 IL-6 concentration in OHSC supernatant over (A) short term and (B) long term observation period exposed to sham or 0.3 Gy X-irradiation. The concentration of the pro-inflammatory marker IL-6 was measured using a highly sensitive ELISA assay. IL-6 was determined for each measurement time point after 72 hours of cultivation time. N = 3, i = 3, s = 9. Means ± SEM. Statistics performed by unpaired t-test with Welch's correction, comparing each group to 0 Gy, sham irradiation control at the corresponding time * $p < 0.05$, **** $p < 0.0001$.

Additionally, to low dose effects of X-rays, a higher dose of 3.0 Gy was investigated (Figure 19). The IL-6 concentration in the culture supernatants of X-ray irradiated OHSCs, 12 hours post irradiation, was not statistically significantly altered with exposure to 3.0 Gy X-rays in comparison to the control group. The concentrations varied between an average of 16.21 pg/mL (sham) and 12.52 pg/mL (0.3 Gy), with the highest radiation dose inducing a mean of approximately 14.05 pg/mL of IL-6 in the supernatant. Samples exposed to 3.0 Gy irradiation did not yield analyzable DG regions for PI+ cell quantification.

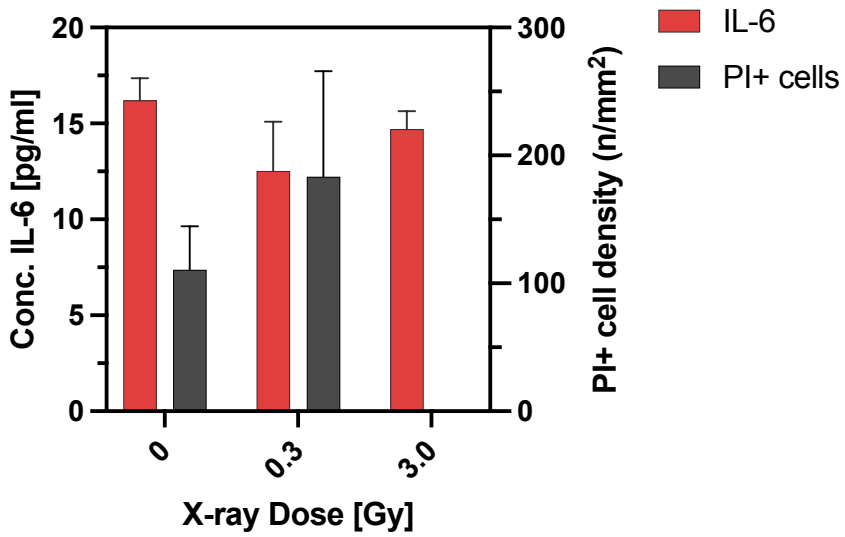

Figure 19 Dose-dependent IL-6 secretion and cell death (PI-positive cell density) in OHSCs following X-ray exposure. Quantification of IL-6 concentration (red bars, left y-axis) in culture supernatants and PI-positive cell density (gray bars, right y-axis) 12 hours post-irradiation with 0, 0.3, and 3.0 Gy X-rays. IL-6 levels were determined using high-sensitivity ELISA following 72 hours of cultivation. Data represent means ± SD from independent experiments (N=1-3, with i=1-3 internal replicates, total samples s=3-9). Statistical analysis was performed using unpaired t-tests with Welch's correction, comparing irradiated samples to sham controls (0 Gy).

3.5.5 Differentially expressed genes in OHSCs exposed to X-ray

To identify further changes in gene expression 12 hours post X-ray irradiation, RNA-seq analysis of 0.3 Gy X-ray irradiated OHSCs were compared to sham irradiated OHSCs. Comparison of housekeeping genes revealed no significant differences, suggesting that the observed genomic changes were caused by radiation (Figure 20A). The results of the differentially expressed gene (DEG) analysis are shown in the volcano plot (Figure 20B). It displays 35 out of 17025 investigated genes that are significantly differentially expressed. In detail, 17 genes were down-regulated (blue dots) and 18 genes were up-regulated (red dots) following irradiation.

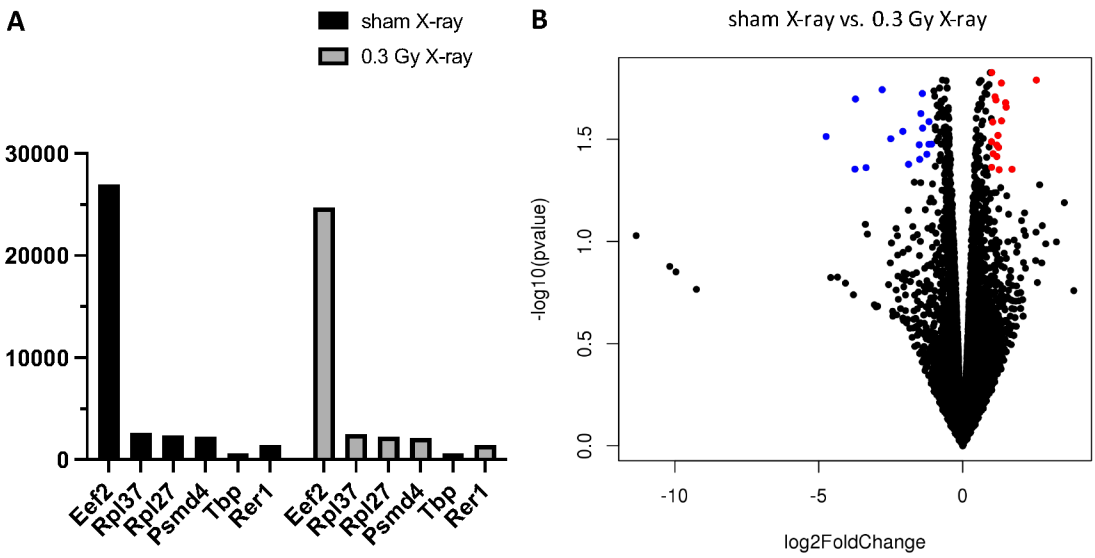

Figure 20 Gene Expression differences of sham or 0.3 Gy X-ray irradiated OHSCs. (A) Expression of housekeeping genes. (B) Significantly differentially expressed genes (DEG) between sham (X-ray) and 0.3 Gy X-irradiated OSHC at 12 h post irradiation. The x-axis of the volcano plot represents the log2 fold change (the difference between the expression level in the irradiated sample and the sham control sample), and the y-axis represents the -log10 of the p-value (the significance of the difference). Genes with high fold changes and low p-values are considered to be differentially expressed. Blue dots are therefore down-regulated proportion of genes, red dots the up-regulated genes compared to sham control and black dots are non-significant. Generated by Azenta Genewiz bioinformatics.

To identify DEG's associated with CNS inflammation, a gene ontology (GO) Ribbon Sandbox Tool analysis was conducted on the DEG dataset, focusing on annotations associated with genes involved in microglia activation and CNS inflammatory processes. Of the 35 differentially expressed genes, 12 genes had corresponding annotations. Table 5 highlights the genes and relevant annotations (red-framed area), where the color gradient indicates the number of available annotations for each subset term (text above squares) from low (white square) to high numbers (dark square). X-ray irradiation downregulated the expression of *otx2*, *muc2*, *lox*, *Igf2*, *stra6*, and *ret*, and upregulated that of *vegfd*, *msr1*, *htr7*, *ifi203*, *nmbr* and *mmp3* (Table 5).

Table 5 Annotation summary of significant, differentially expressed genes in Mus musculus (Mmu) between sham irradiated and 0.3 Gy X-irradiated OHSC at 12 h post irradiation.

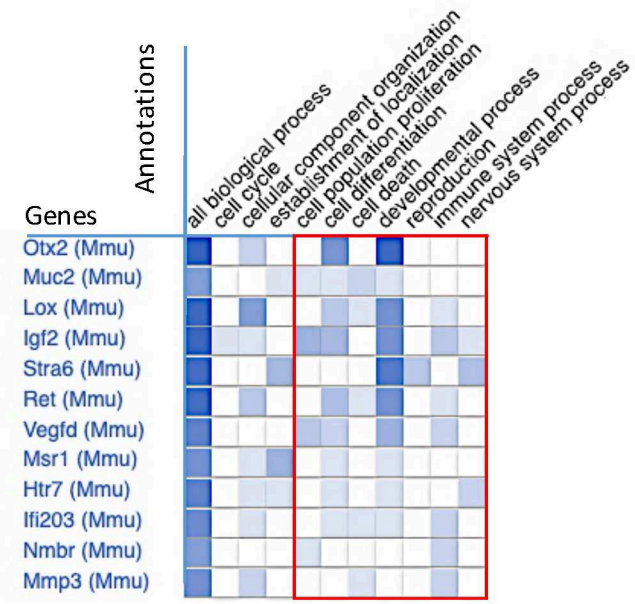

Relevant annotations were filtered out for each gene and listed in Table 5. The expression of gene associated with neuronal cell fate and differentiation, such as *otx2*, is downregulated upon irradiation. Additionally, genes that are involved in memory (*igf2*), cognition, and learning processes (*stra6*) are expressed at reduced levels. Conversely, the production of pro-inflammatory cytokines, IL-6 and IL-1β, was upregulated, as indicated by the elevated expression of *vegfd* and *ifi203* genes. Moreover, innate immune response activation (*ifi203*), G-protein coupled receptor activity (*htr7, nmbr*), and oxidative stress-induced cell death (*mmp3*) are upregulated upon X-ray irradiation (Table 6).

Table 6 List of genes with significantly different expression between 0.3 Gy and sham X-ray irradiated OHSCs 12 h post exposure. The p-values listed represents the probability of observing a certain number of genes annotated to a specific term given the proportion of the background genes annotated to that term.

Mouse genome informatics (MGI) ID	Gene symbol	Full gene name	Log2 fold change	P-value	Regulation related to control	Relevant gene annotation	Reference
MGI:97451	Otx2	orthodenticle homeobox 2	-3.358	0.044	↓	Axon guidance, cell differentiation, cell fate commitment, neuron fate commitment, neuron fate determination, neuron fate specification, oligodendrocyte differentiation	GO_REF:0000096, PMID:26494787, PMID:15105370, PMID:16339193, PMID:26166575, PMID:19592574, PMID:19592574, PMID:15888661, PMID:26166575, PMID:26166575
MGI:1339364	Muc2	mucin 2	-1.51	0.034	↓	pos. regulation of apoptotic process, neg. regulation of cell migration, neg. regulation of cell population proliferation	PMID:11872843, PMID:11872843, PMID:11872843
MGI:96817	Lox	lysyl oxidase	-1.494	0.040	↓	cellular response to chemokine, reg. of apoptotic process	PMID:18586678, PMID:28538980
MGI:96434	Igf2	insulin-like growth factor 2	-1.402	0.019	↓	memory	GO_REF:0000096
MGI:107742	Stra6	stimulated by retinoic	-1.174	0.033	↓	cognition, learning	GO_REF:0000096, GO_REF:0000096
MGI:97902	Ret	ret proto-oncogene	-1.082	0.033	↓	glial cell-derived neurotrophic factor receptor signaling pathway	GO_REF:0000096
MGI:108037	Vegfd	vascular endothelial growth factor D	1.058	0.037	↑	positive regulation of interleukin-6 production	GO_REF:0000096
MGI:98257	Msr1	macrophage scavenger receptor 1	1.156	0.020	↑	endocytosis	GO_REF:0000004
MGI:99841	Htr7	5-hydroxytryptamine (serotonin) receptor 7	1.348	0.017	↑	dopaminergic neuron differentiation, G protein-coupled receptor activity, neuronal cell body	GO_REF:0000096, GO_REF:0000002, GO_REF:0000096
MGI:96428	Ifi203	interferon activated gene 203	1.512	0.022	↑	activation of innate immune response, pos. regulation of IL-1 beta production	GO_REF:0000096
MGI:1100525	Nmbr	neuromedin B receptor	1.715	0.044	↑	G protein-coupled receptor activity	GO_REF:0000004
MGI:97010	Mmp3	matrix metallopeptidase 3	2.558	0.016	↑	neg. regulation of hydrogen peroxide metabolic process, pos. regulation of oxidative stress-induced cell death, innate immune response	GO_REF:0000096, PMID:20969476,

↑ = up-regulated, ↓ = down-regulated

The analyses shown above, demonstrates that exposure to X-rays triggers an upregulation of genes associated with the activity of G protein-coupled receptors (GPCRs) such as *htr7* and *nmbr*. Therefore, the RNA expression levels of the cannabinoid GPCR genes *cnr1* (CB1), *cnr2* (CB2) and *gpr55* (GPR55) were quantified (Figure 21). The results show only slight changes in the expression of the three receptor genes, with *cnr1* and *gpr*55 being upregulated and *cnr2* being downregulated. Given that this study is based on one experiment with 3 OHSCs per insert membrane, it is crucial to validate this analysis.

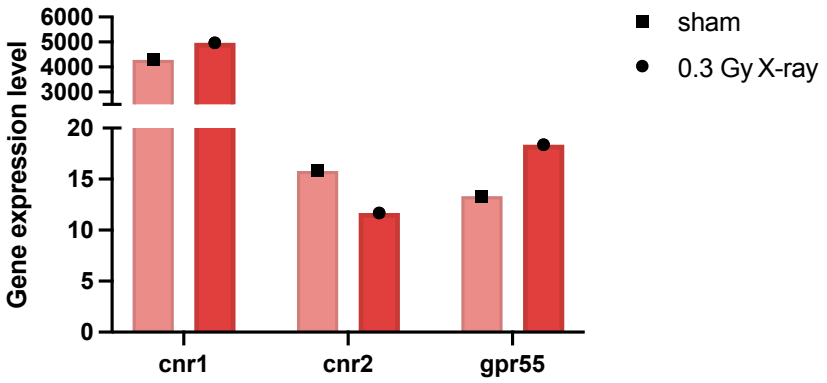

Figure 21 Gene expression of cnr1, cnr2 and gpr55 in 0.3 Gy X-irradiated OHSCs 12 h post exposure. Gene expression was analyzed with RNA sequencing methods by Azenta Genewiz. N = 1, s = 3.

3.5.6 Effects of synthetic cannabinoid-receptor ligands on X-ray irradiated OHSCs

The present studies focused on the damage mitigating effects of cannabinoid-receptor ligands GP1a and AbnCBD on OHSCs that have been exposed to X-rays. A proof-of-concept experiment was conducted, consisting of one experiment with 3 OHSCs on an insert (N = 1, i = 1, s = 3) for 3.0 Gy X-rays. As previously shown, treatment of sham irradiated OHSCs with the agonists did not change IL-6 secretion (Figure 12). To facilitate comparison, these results are also presented as 0 Gy (sham) in Figure 22. At 12 hours post cannabinoid-receptor ligand treatment, an increased variability between experiments was detected (20.53 ± 17.60 pg/mL). The administration of the CB2 receptor agonist GP1a to OHSCs irradiated with 0.3 Gy led to a statistically significant but biologically marginal decrease in IL-6 (16.58 ± 1.14 to 11.90 ± 0.88 pg/mL) compared to the sham irradiated and GP1a treated group (Figure 22). No dose-dependent increase in IL-6 was observed in any of the samples. Overall, IL-6 levels remained below 25 pg/mL in all tested conditions.

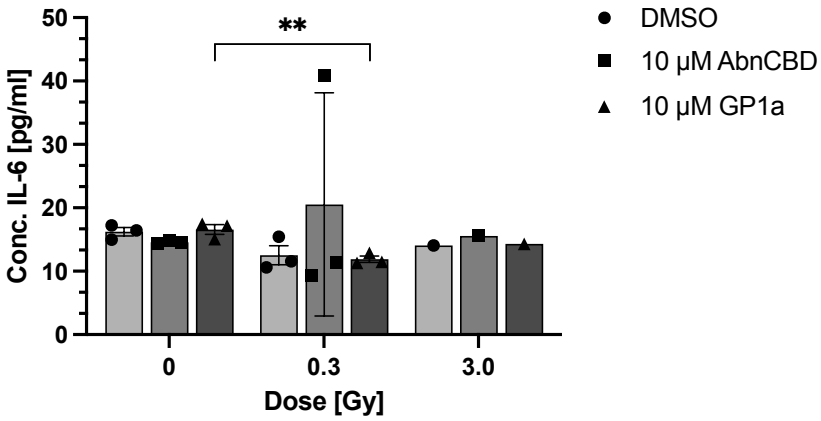

Figure 22 Dose-dependent IL-6 concentration in tissue culture supernatant of OHSCs 12 h post X-ray exposure and subsequent treatment with 10 µM of *cannabinoid-receptor* agonists GP1a and AbnCBD. N =1-3, i = 1- 3, s = 3 - 9; Error bars: Mean ± SD. Statistics performed by 2way ANOVA (Sidak's muliple comparison). Comparisons were conducted between sham vs. irradiated groups. ** p < 0.001.

The subsequent sections further elucidate detailed investigations of the receptor ligands on X-ray irradiated OHSCs.

3.5.6.1 Effects of GP1a treatment after exposure to X-rays

GP1a is highly specific cannabinoid receptor 2 ligand. CB2 is preferentially expressed on activated microglia. Therefore, in the following section, cellular changes that are caused by the binding of GP1a to CB2 on microglia were investigated in further detail.

The examination of the total cell number after addition of 10 µM GP1a revealed a 22 % lower total cell number (mean difference ~ 100 cells) 48 hours after X-ray irradiation compared to the DMSO control (Figure 23). Long-time data points, 7 days after irradiation and treatment, revealed higher total cell numbers in the dentate gyrus of OHSCs, but similar total cell number 29 days after compared to the controls.

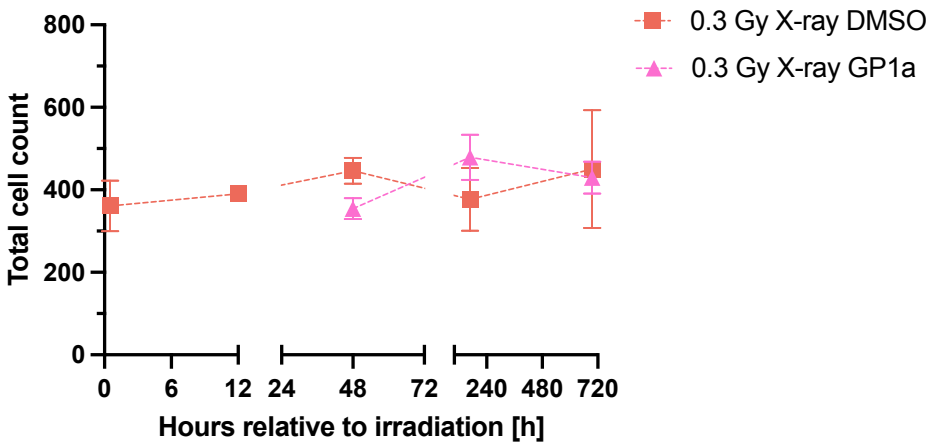

Figure 23 Total cell count in dentate gyrus of sham and 0.3 Gy X-ray irradiated OHSCs treated with 10 µM GP1a over the entire cultivation time. Cell numbers were determined by DAPI staining of 350 µm whole mount OHSCs. Error bars: mean ± SEM. N = 3, i = 1, s = 3. Statistics performed by unpaired t-test with Welch's correction, comparing irradiated samples at each time point to sham irradiated OHSC at associated experimental time point.

In Figure 16A the radiation effects of X-ray on untreated microglia and PI+ cell density was demonstrated. The impact of GP1a treatment on X-ray irradiated OHSCs was evaluated over a 29-day period (

Figure 24). Both GP1a-treated and DMSO control groups showed similar microglial densities through the first 48 hours post-irradiation (

Figure 24A). A notable divergence emerged at day 7, where GP1a-treated OHSCs demonstrated approximately 200 % reduction in microglial density compared to controls (

Figure 24B). This differential effect on microglial populations was transient, with densities converging again by day 29. Notably, GP1a treatment was associated with a dynamic in cell death as evidenced by decreased PI+ cell density at 48 hours and an increase in cell death, beginning at day 7 and reaching statistical significance by day 29 ($p < 0.0001$;

Figure 24A,C). This observation suggests that while GP1a effectively modulates microglial populations in the intermediate term, it may compromise overall tissue viability in the long-term following radiation exposure.

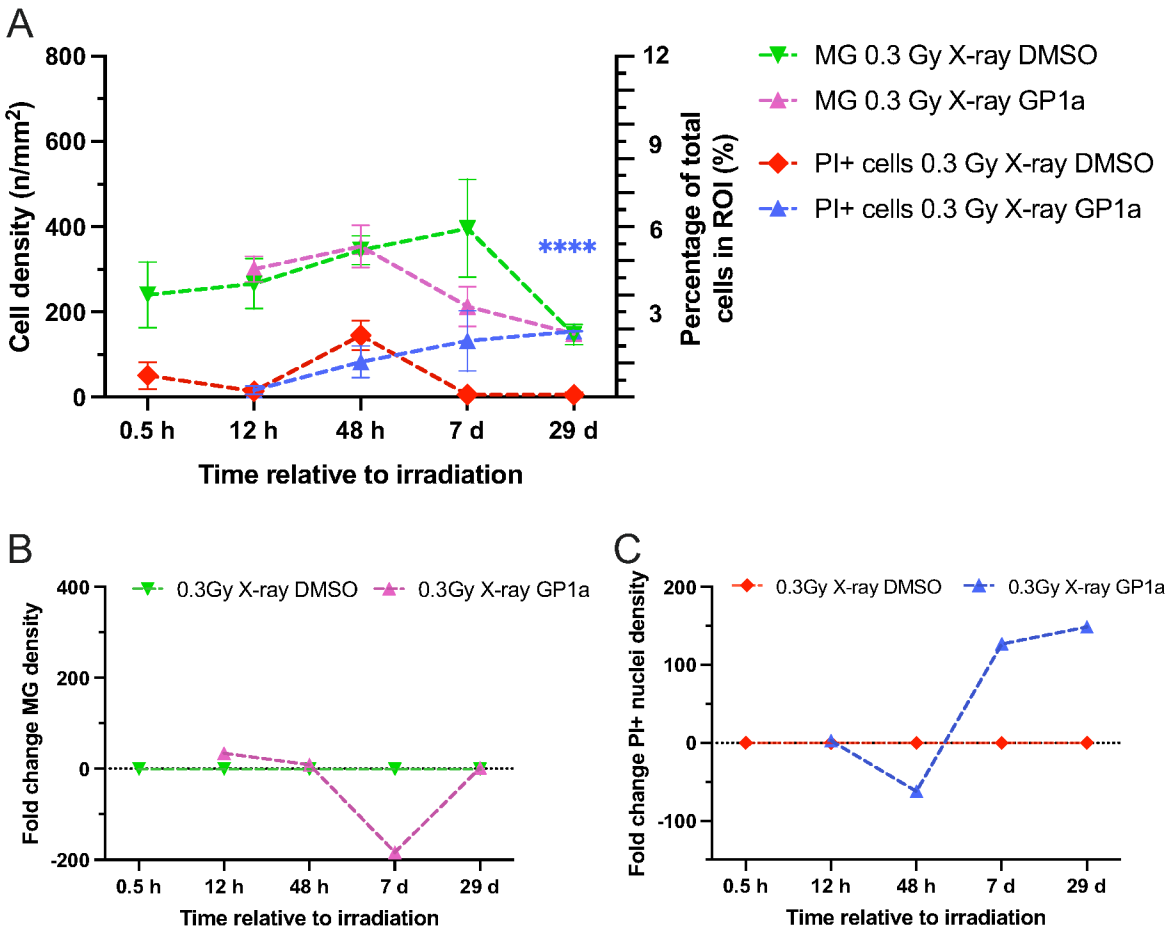

Figure 24 Temporal dynamics of microglial density and cell death in X-ray irradiated hippocampal tissue following GP1a treatment. (A) Quantification of microglial density (left y-axis) and PI-positive cells (right y-axis) in the dentate gyrus following 0.3 Gy X-ray exposure with either DMSO (control) or 10 µM GP1a treatment. (B) Fold change in microglial density relative to time-matched sham controls. (C) Temporal changes in PI-positive cell density expressed as fold change compared to sham controls, demonstrating increased cell death in GP1a-treated samples from day 7 onward. Cell densities were calculated per mm^2 of dentate

gyrus region of interest (ROI). Data represent mean ± SEM from three independent experiments with three internal replicates each (n = 9 total samples). ****p < 0.001, unpaired t-test with Welch's correction comparing irradiated samples to time-matched sham controls).

To investigate the effects of X-ray irradiation and subsequent treatment with GP1a on microglial activation, a classification of the three morphological classes was performed in accordance with the method previously described (Figure 17). For technical reasons, no measurements could be taken 12 hours post irradiation in the GP1a treated OHSCs. Microglial morphological changes following 0.3 Gy X-ray exposure and GP1a treatment were analysed using a semi-automated classification approach. In the acute phase (0.5h - 48h), control samples showed a relatively stable distribution of morphological classes, with reactive microglia comprising approximately 60 % of the population. GP1a treatment induced a marked shift in microglial phenotypes by 48 hours, characterized by a dramatic increase in ramified microglia and a corresponding decrease in amoeboid cells (Figure 25A). During the long-term period (7d - 29d), both control and GP1a-treated samples exhibited a more balanced distribution between morphological classes, though GP1a treatment maintained a slightly higher proportion of reactive microglia (Figure 25B). Quantitative analysis of class-specific changes revealed a striking ~6000 % increase in ramified microglia at 48 hours post-irradiation in GP1a-treated samples, accompanied by a modest increase in reactive morphology and reduction in amoeboid cells (Figure 25C). These morphological shifts largely normalized by day 7 despite an approximate 100 % reduction of ramified cells, with only subtle differences persisting through day 29 (Figure 25D).

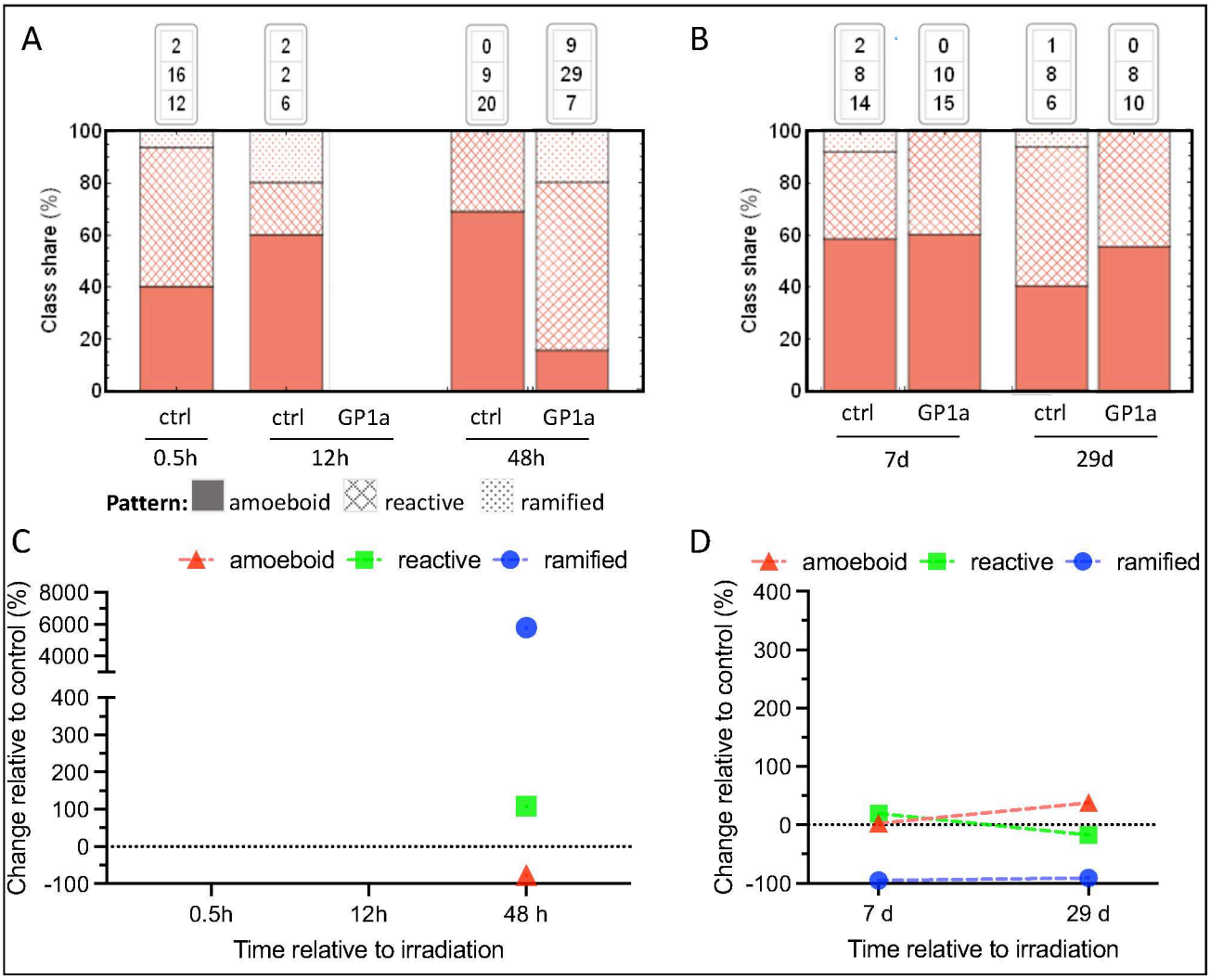

Figure 25 Temporal dynamics of microglial morphological changes following X-ray exposure and GP1a treatment. (A) Distribution of microglial morphological classes (amoeboid, reactive, and ramified) during the acute phase (0.5-48h) and (B) extended period (7-29d) post-irradiation in control and GP1a-treated samples. Numbers above bars indicate absolute cell counts per class. (C, D) Fold change in morphological class distribution relative to irradiated, DMSO-treated controls during acute (C) and extended (D) observation periods. Data represent measurements from 9 OHSCs across 3-4 independent experiments, with initial classification training performed on 100 cells per morphological class. Control data from previous measurements were included for comparison.

IL-6 concentrations of OHSCs treated with 10 µM GP1a following X-ray irradiation were comparable to controls up to 48 hours (Figure 26A). However, starting from day 7 post irradiation, a marked increase in average IL-6 concentrations was observed (mean 21.85, SD ± 10.86 pg/mL), which was statistically significant after 29 days compared to DMSO controls (mean diff. ± SEM: 7.73 ± 1.26 pg/mL) (Figure 26B). Overall, the supernatant of GP1a-treated and irradiated OHSCs had on average higher concentrations of IL-6 compared to the irradiated only samples.

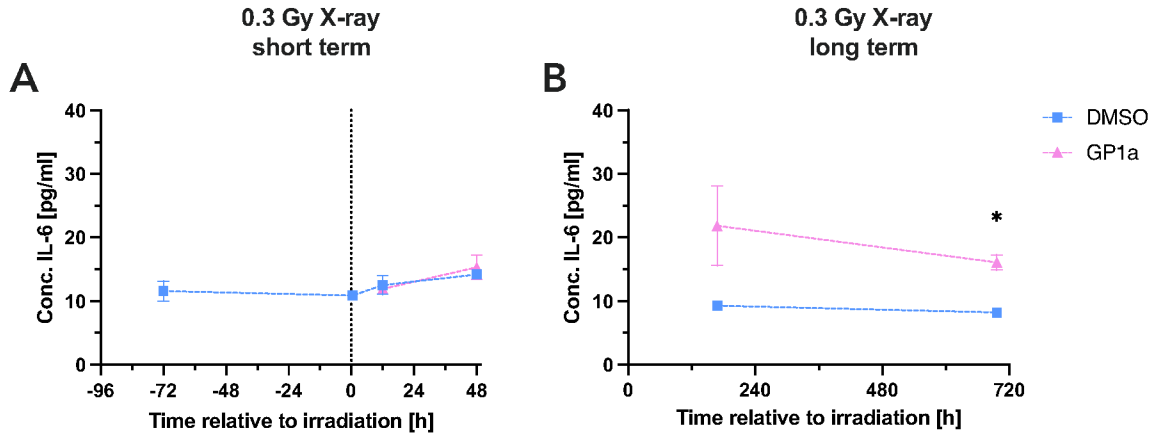

Figure 26 IL-6 concentration in sham and 0.3 Gy X-ray irradiated samples with and without 10 µM GP1a. IL-6, was accumulated over a period of 72 h for each sampling time point and measured in pg/mL with a high-sensitivity ELISA assay. The data presented for -72 h and 0.5 h DMSO were collected during the same experimental procedure but recurring in this figure. N = 3, i = 3, s = 9; Error bar: mean ± SEM. Statistics performed by unpaired t-test with Welch's correction, comparing each group to 0.3 Gy DMSO controls at corresponding time. * $p < 0.05$.

To examine the effects of radiation and potential mitigating effects of the ligands AbnCBD and GP1a on the genomic level, the conventional qPCR method with designed primers for the cannabinoid-receptor genes *cnr1* (CB1), *cnr2* (CB2), and *gpr55* (GPR55) was employed, considering all relevant requirements for an optimal primer design.

The qPCR amplification was followed by a melting curve and melting peak analysis to evaluate the specificity of the PCR products. The melting curves plot the relative fluorescent units (RFU) against the increasing temperature (Figure 27, left panel) and the melt-peak curves plot dRFU/dT against the temperature (Figure 27, right panel). In the melt peak graphs on the right panel, the curves observed at lower temperatures (arrow, magenta), before the specific product peak (arrow, red) in the melting curve of *cnr1* and *gpr55*, suggest the formation of primer-dimers during amplification that could bind to the Sybr- Green dye early in the process (Figure 27, right panel). The presence of genomic DNA contamination is also indicated, by the third peak in the melting curve of *gpr55* (arrow, blue). No DNA double strands have formed, as evidenced by the lack of DNA amplification observed in *cnr2* (Figure 27, right panel). Multiple attempts were made to amplify the samples with different primer pairs, but insufficient transcript amplification or impurities were repeatedly observed.

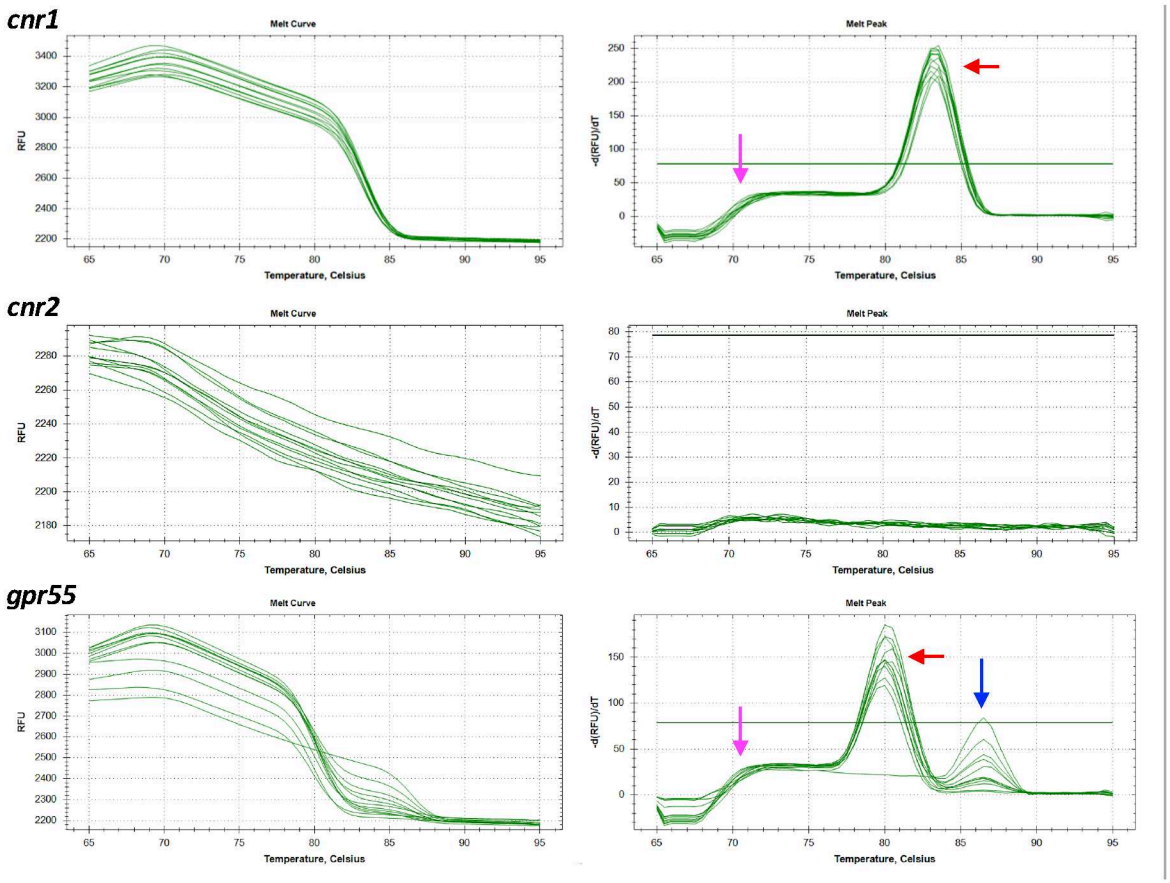

Figure 27 Melt curve (left panel) and melt peak (right panel) analysis of qPCR products amplified using primers specific for cannabinoid-receptor genes cnr1, cnr2, and gpr55.

Due to time constraints, an alternative method, was employed instead of designing and testing additional primers. RNA sequencing was adopted as an alternative method, which is more sensitive to small expression differences and is better suited for the complex OHSC model system. Subsequently, all gene expression analyses were conducted utilizing RNA sequencing. RNA was isolated 12 hours post irradiation and was subsequently sequenced by Azenta Genewiz (Leipzig, Germany).

The gene expression analysis provided insights into the impact of 10 µM GP1a on the cannabinoid-receptor expression (Figure 28). Upon GP1a treatment, CB1 receptor gene (*cnr1*) expression slightly decreased. Conversely, expression of *cnr2*, which is responsible for regulating CB2 receptor expression and is known to be modulated by GP1a, slightly increased post irradiation and treatment. The treatment of X-ray irradiated OHSCs with GP1a resulted in a decrease of *gpr55* expression, which is involved in regulating the homonymous receptor. In conclusion, a significant

alteration in cannabinoid-receptor gene expression upon treatment with GP1a in X-ray irradiated OHSCs could not be detected.

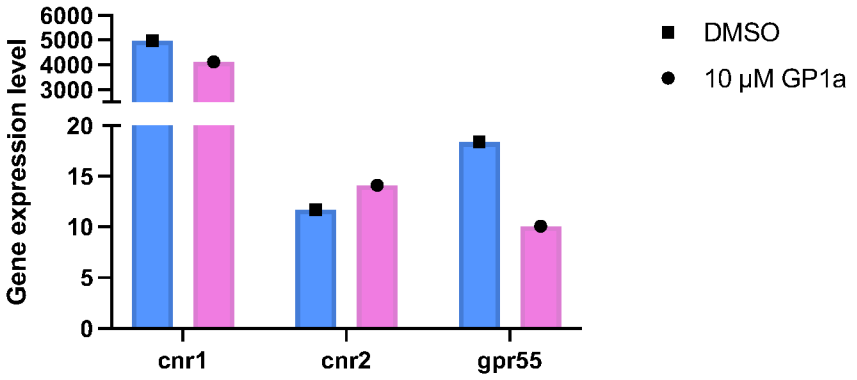

Figure 28 Gene expression of cnr1, cnr2 and gpr55 in GP1a treated, 0.3 Gy X-irradiated OHSC 12 h post exposure. Gene expression was analyzed with RNA sequencing methods by Azenta Genewiz. N = 1, s = 3.

3.5.6.2 Effects of AbnCBD treatment after exposure to X-rays

AbnCBD is an agonist of the G-protein-coupled receptor 55, which was shown to have neuroprotective effects in neurodegenerative diseases or wound healing *in vivo* and *in vitro*. GPR55 is expressed in immune cells such as monocytes and microglia and has been reported to modulate inflammation.

Analogous to experiments in the previous chapter, 10 µM AbnCBD was tested for damage mitigating effects on cultivated and X-ray irradiated OHSCs. The mean total cell count after AbnCBD treatment was 503.00 ± 90.01 cells, which is statistically insignificantly higher than the control but three-fold higher in variance. In the long term, comparable values were found between AbnCBD and DMSO treated OHSCs (Figure 29).

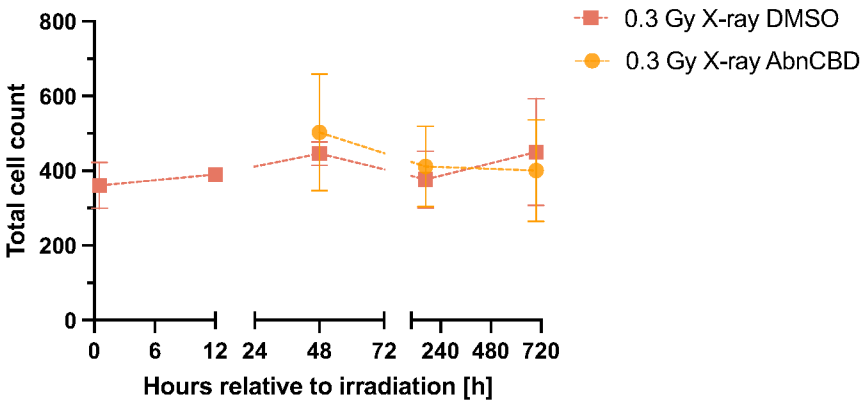

Figure 29 Total cell count in dentate gyrus of sham and 0.3 Gy X-ray irradiated OHSCs treated with 10 µM AbnCBD over the entire cultivation time. Cell numbers were determined by DAPI staining of 350 µm whole mount OHSCs. Error bars: mean ± SEM. N = 3, i = 1, s = 3. Statistics performed by unpaired t-test with Welch's correction, comparing irradiated samples at each time point to sham irradiated OHSC at associated experimental time point.

Microglial and PI+ cell densities were quantified in X-ray irradiated OHSCs treated with the cannabinoid receptor ligand AbnCBD (10 µM) or DMSO control (Figure 30).

In the early post-irradiation period, AbnCBD treatment was associated with an earlier increase in microglial density compared to DMSO control, observed between 48 hours and 7 days (Figure 30A). At 48 hours, approximately 7 % of all cells in the DG region were microglia in the AbnCBD-treated group, whereas this percentage dropped to around 3 % by day 7. A significant decrease in microglial density occurred from 48 hours to 7 days in both the AbnCBD-treated and irradiated OHSCs. By 29 days post-irradiation, both the AbnCBD-treated and control conditions demonstrated lower microglial densities relative to initial values. At 48 hours post-irradiation, the AbnCBD-treated group exhibited approximately a 60-fold increase in the percentage of PI+ cells compared to controls. However, this elevated cell death was transient, as PI+ cell percentages returned to control levels by 29 days (Figure 30C). The temporal changes in microglial density profiles were similar between the AbnCBD-treated and DMSO control OHSCs, showing only slight differences over the 29-day observation period (Figure 30B).

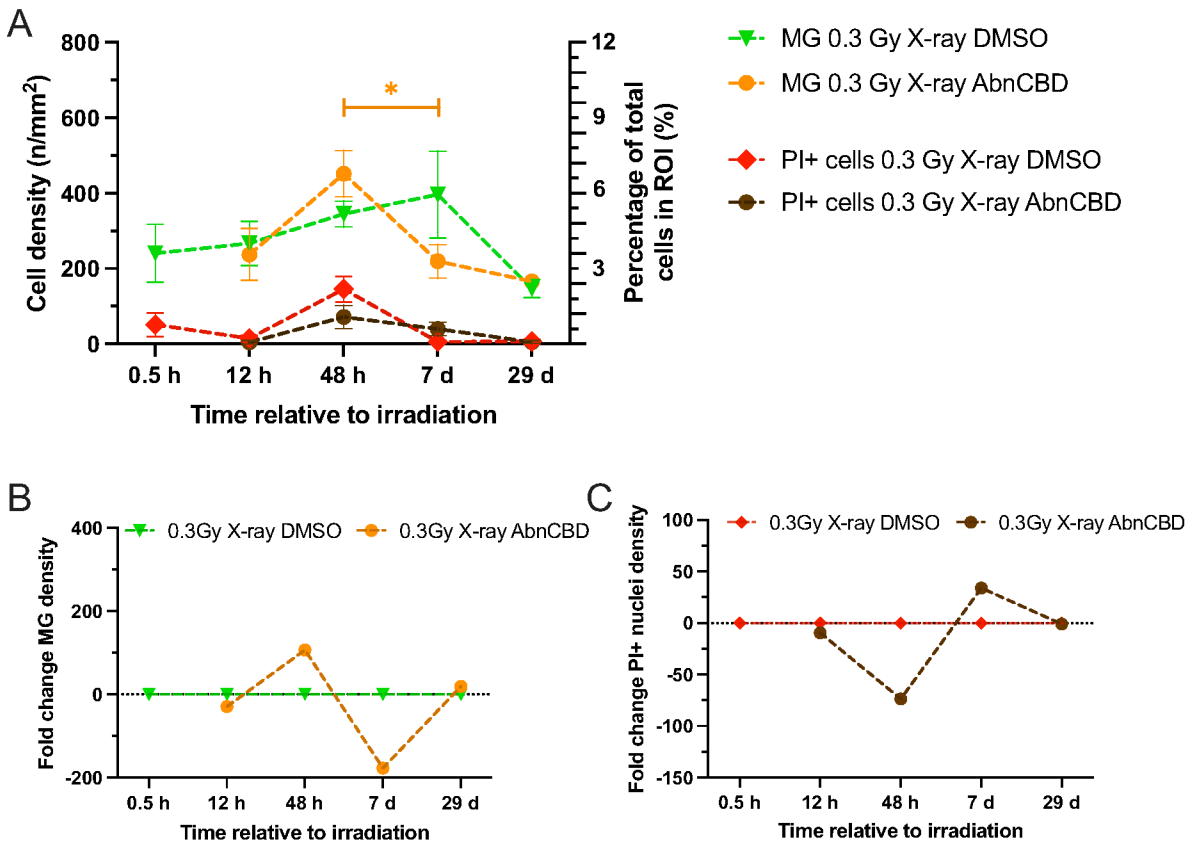

Figure 30 Microglial and cell death responses in X-ray irradiated hippocampal tissue following AbnCBD treatment. (A) Quantification of microglial (MG) density and PI-positive cell counts in the dentate gyrus of OHSCs exposed to 0.3 Gy X-rays and treated with either DMSO or 10 µM AbnCBD over 29 days. (B) Fold change in microglial density relative to 0.3 Gy X-ray irradiated DMSO controls. (C) Fold change in PI-positive cell density relative to 0.3 Gy X-ray irradiated DMSO controls. Cell densities were measured by analysing immunofluorescent images and normalized to the dentate gyrus area (mm2). Data represent mean ± SEM from three independent experiments with three internal replicates each (N=3, i=3, s=9 total samples). Statistical significance was determined using unpaired t-tests with Welch's correction, comparing each treatment group to the irradiated DMSO control within a given time point (*p < 0.05).

The proportional distribution of microglial morphological classes was analysed following 0.3 Gy X-ray irradiation and subsequent treatment with 10 µM AbnCBD. In the acute phase (0.5 – 48 h), DMSO control samples exhibited a relatively stable profile, with reactive microglia comprising the majority. AbnCBD treatment induced a shift in microglial phenotypes by 48 hours, characterized by a decrease in amoeboid cells and an increase in ramified morphology (Figure 31A). This treatment-related effect diminished during the extended 7 – 29 day observation, with both groups showing a more balanced distribution across the three classes (Figure 31B).

Quantitative analysis revealed that AbnCBD treatment was associated with a sustained reduction in the amoeboid microglial population compared to irradiated DMSO controls, while the reactive and ramified classes showed more modest fluctuations over time (Figure 31C, Figure 31D). The

control data from a previous measurement were included to facilitate comparability across experiments.

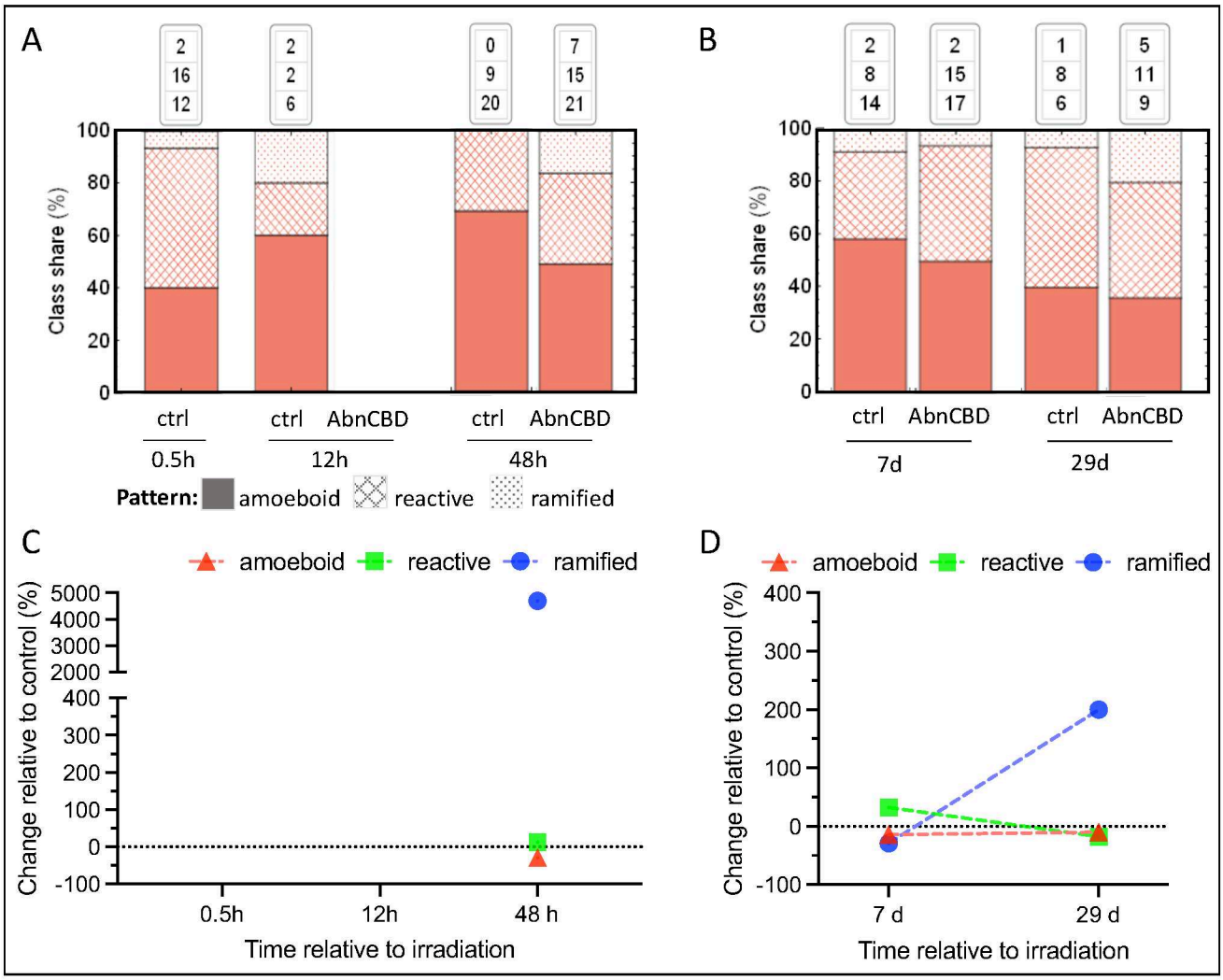

Figure 31 Temporal dynamics of microglial morphological changes following X-ray exposure and AbnCBD treatment. (A) Distribution of microglial morphological classes (amoeboid, reactive, and ramified) during the acute phase (0.5-48h) and (B) extended period (7-29d) post-irradiation in control (0.3 Gy X-ray + DMSO) and AbnCBD-treated samples. Numbers above bars indicate the absolute number of cells detected per class in 9 organotypic hippocampal slice cultures (OHSCs) across 3-4 independent experiments. (C) Fold change in morphological class distribution relative to 0.3 Gy X-ray irradiated DMSO controls during the acute observation period. (D) Fold change in morphological class distribution relative to 0.3 Gy X-ray irradiated DMSO controls during the extended observation period.

Pro-inflammatory cytokine levels were also determined for AbnCBD treatment post X-ray irradiation. X-ray irradiated OHSCs, treated with AbnCBD showed no significant deviations of IL-6 concentrations from the untreated controls over the course of the experiments (Figure 32). At 12 hours strong fluctuations between the treated conditions became apparent (20.53 ± 10.16). Forty-eight hours post X-ray irradiation, the AbnCBD treatment OHSCs exhibited slightly lower

IL- 6 concentrations compared to the control. The long term cultured OHSCs showed a similar trend with and without treatment.

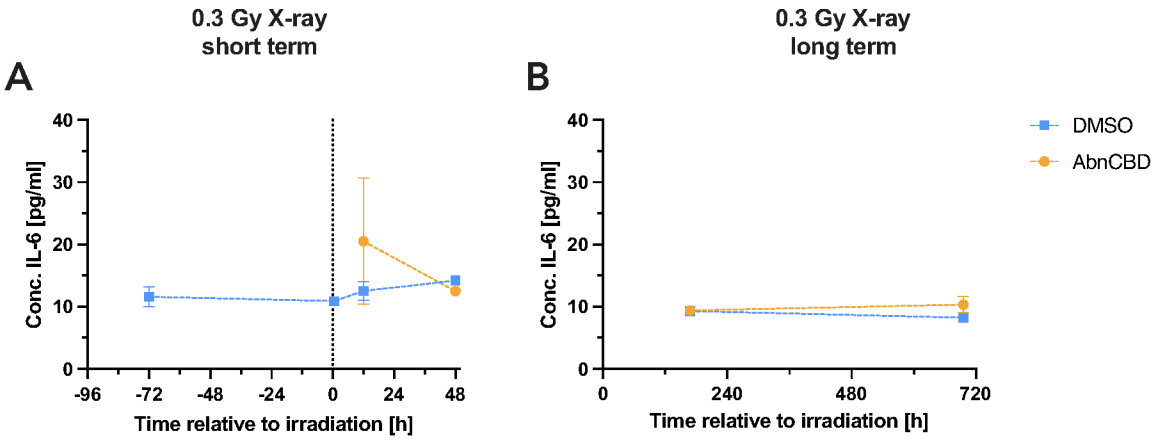

Figure 32 IL-6 concentration in sham and 0.3 Gy X-ray irradiated samples with and without the GPR55 receptor agonist GP1a. IL-6, was accumulated over a period of 72 h per sampling time point and was measured in pg/mL with a high-sensitivity ELISA assay. N = 3, i = 3, s = 9. Error bars: mean ± SEM. Statistics performed by unpaired t-test with Welch's correction, comparing each group to 0 Gy, sham irradiation control at corresponding time.

The genomic changes induced by AbnCBD treatment at the 12-hour time point were examined in detail (Figure 33). The gene expression analysis performed, exhibited results similar to those obtained with GP1a (Figure 28). The expression levels of cnr1 and gpr55 did not exhibit any discernible response to AbnCBD administration 12 hours post irradiation. Cnr2 expression increased with AbnCBD treatment (11.7 to 17.8) when compared to the control group.

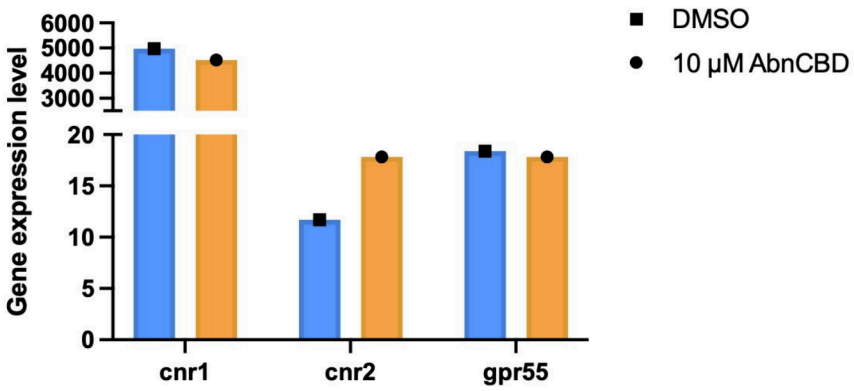

Figure 33 Gene expression of cnr1, cnr2 and gpr55 in AbnCBD treated, 0.3 Gy X-irradiated OHSCs 12 h post exposure. Gene expression was analyzed with RNA sequencing methods by Azenta Genewiz. N = 1, s = 3.

3.6 Impact of ^{56}Fe-ion Irradiation on Microglia

To examine the impact of high-LET radiation on microglia and their inflammatory response, OHSCs were cultured *in vitro* and exposed to 0.3 Gy ^{56}Fe-ion radiation at 1 GeV/n. The expression of different inflammatory signals of microglial cells was assessed and compared to the results of X-ray exposure from the preceding sections.

3.6.1 Cell survival in OHSCs post 0.3 Gy ^{56}Fe-ion irradiation

The total cell counts in the DG following irradiation with ^{56}Fe-ions was determined by DAPI nucleus staining with subsequent quantification of fluorescence signals (Figure 34). During the initial 12-hour period post irradiation, the cell numbers in the irradiated OHSCs were almost equal to the control values. However, a consistent, non-significant decrease in cell numbers was observed in the irradiated OHSCs (360.00 ± 39.51) compared to the controls, which also exhibited a high variability (425.33 ± 104.04) at subsequent measurement time points.

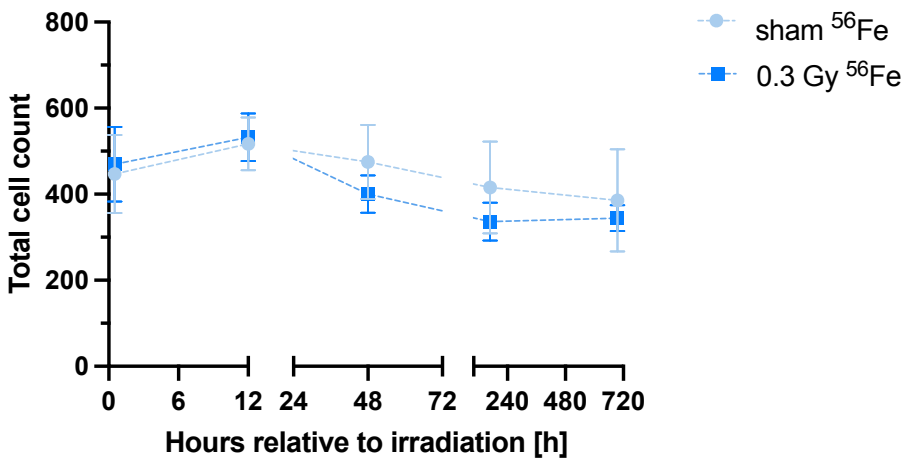

Figure 34 Total cell number in dentate gyrus of sham and 0.3 Gy ^{56}Fe-ion irradiated OHSCs. Cell numbers were determined by DAPI staining of 350 µm whole mount OHSCs. Error bars: mean ± SEM. N = 3, i = 3, s = 9. Statistics performed by unpaired t-test with Welch's correction, comparing irradiated samples at each time point to sham irradiated OHSC at associated experimental time point.

3.6.2 SPATIOTEMPORAL DYNAMICS OF MICROGLIAL POPULATION AND CELL DEATH IN THE DENTATE GYRUS FOLLOWING ^{56}FE- EXPOSURE

The graphs in Figure 35 show the temporal dynamics of microglia and PI+ cell densities in the DG region following exposure to 0.3 Gy ^{56}Fe-ion irradiation. Figure 35A reveals distinct patterns in the microglia population over time. Initially, at 12 hours post-irradiation, a significant reduction in microglia density was observed. This was followed by a rapid proliferation phase, with microglia density peaking around 500 cells/mm^2 (approximately 7.5 % of total cells) at 48 hours post-irradiation. Subsequently, from day 7 to day 29, the microglia density gradually decreased, eventually stabilizing around 200 cells/mm^2 (approximately 3.0 % of total cells). These temporal changes in microglia density illustrate the complex response of the microglia population to ^{56}Fe-ion irradiation, as shown by the green lines in Figure 35A. Compared to the sham-irradiated controls, the fold change in microglia density was minimal, as depicted in Figure 35B. Regarding PI+ cells, the density remained similar between the ^{56}Fe-ion irradiated and sham-irradiated samples across all time points, as indicated by the red lines in Figure 35A. However, Figure 35C shows that within the ^{56}Fe-ion irradiated group, the PI+ cell density was significantly lower in the DG region from day 7 to day 29 post-irradiation. Overall, the data suggests that while ^{56}Fe-ion irradiation induced a transient decrease in microglia density, the long-term microglia and PI+ cell densities were largely comparable between the irradiated and sham-irradiated conditions.

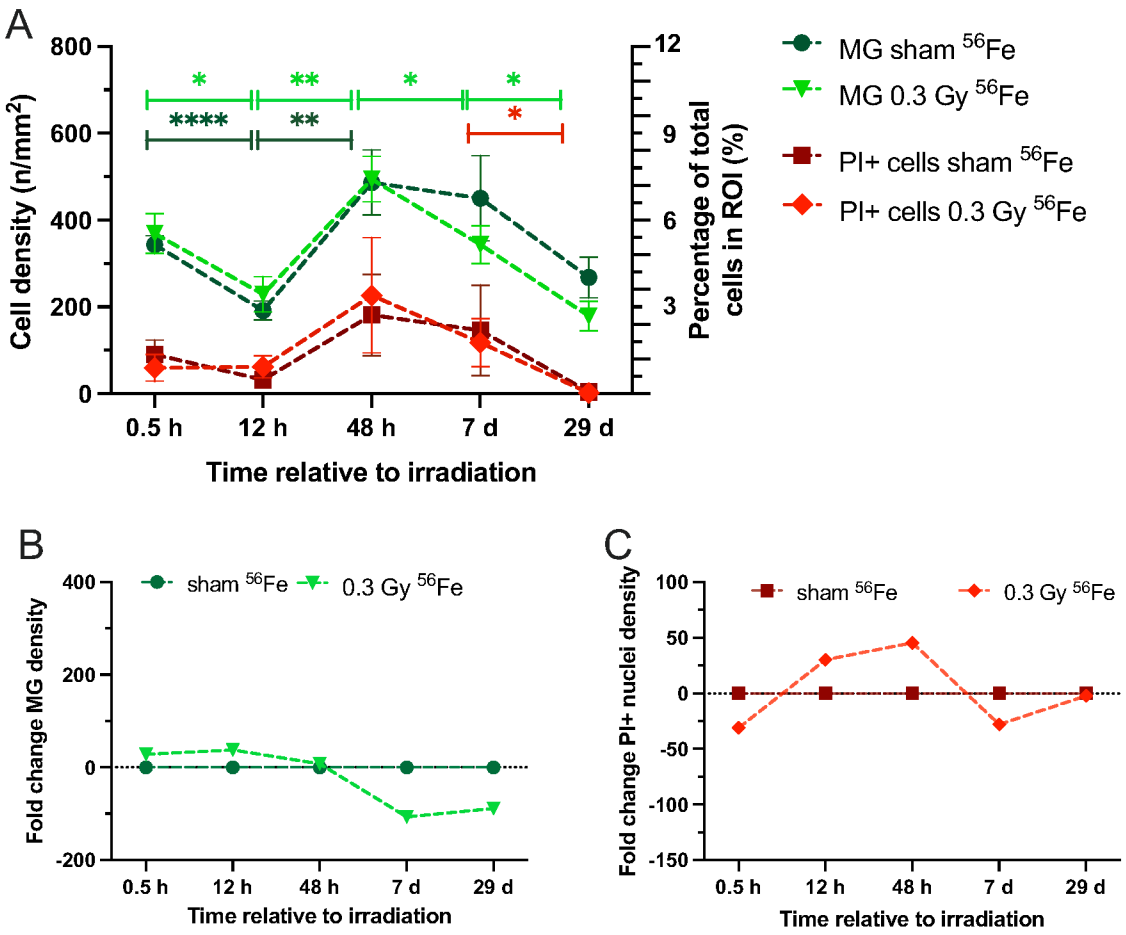

Figure 35 Microglia and PI+ cell density in dentate gyrus of OHSCs, (A) which were exposed to sham or 0.3 Gy ^{56}Fe-ion radiation and monitored over up to 29 days post exposure. Cell numbers were measured by analysis of immunofluorescent images and correlated with the area (mm2) of the associated dentate gyrus region. (B) Fold-change of microglia cell density compared to sham irradiated samples for each time point. (C) Fold change of PI+ cell density compared to sham irradiated samples for each time point. Error bars: mean ± SEM, N = 3, i = 3, s = 9. Statistics performed by unpaired t-test with Welch's correction, comparing each group to the DMSO control within one experimental time point. * $p < 0.05$, *** $p < 0.001$, **** $p < 0.0001$.

3.6.3 Effects of 0.3 Gy ^{56}Fe-ion radiation on microglia morphology

The analysis of microglial morphology following ^{56}Fe-ion irradiation revealed distinct temporal patterns in the distribution of amoeboid, reactive, and ramified phenotypes. At 0.5 hours post-irradiation, while the proportion of amoeboid microglia remained comparable between sham and irradiated samples, the irradiated group exhibited an increased percentage of reactive microglia and approximately 20 % reduction in ramified microglia compared to controls (Figure 36A). The 12-hour timepoint was characterized by a notable peak in amoeboid microglia in both experimental groups, with similar distribution patterns across all morphological classes. By 48 hours post-irradiation, the proportion of amoeboid cells in the irradiated group decreased

substantially from 60 % to 20 % compared to the 12-hour timepoint, falling below control levels. Concurrently, reactive microglia showed a 22 % increase in the irradiated group, comprising 69 % of the total microglial population. At 7 days post-irradiation, the DG of irradiated samples displayed an 18 % increase in ramified microglia and a 9 % decrease in amoeboid microglia relative to sham controls (Figure 36B). The 29-day timepoint showed the lowest proportion of amoeboid microglia across both experimental conditions. Additionally, the reactive microglial population in the irradiated group showed an approximate 29 % increase compared to controls and a 50 % increase relative to the 7-day timepoint (Figure 36B). Throughout the experimental period, the reactive microglial population in ^{56}Fe-ion irradiated OHSCs demonstrated pronounced fluctuations compared to controls (Figure 36C, Figure 36D). The most substantial differences in population distribution were observed in the ramified microglial category at 0.5 hours and 7 days post-irradiation, as indicated by the relative changes to control values shown in panels C and D. The quantitative analysis is supported by the cell counts provided in the numerical boxes above each timepoint in panels A and B, ensuring statistical validity of the observed morphological transitions.

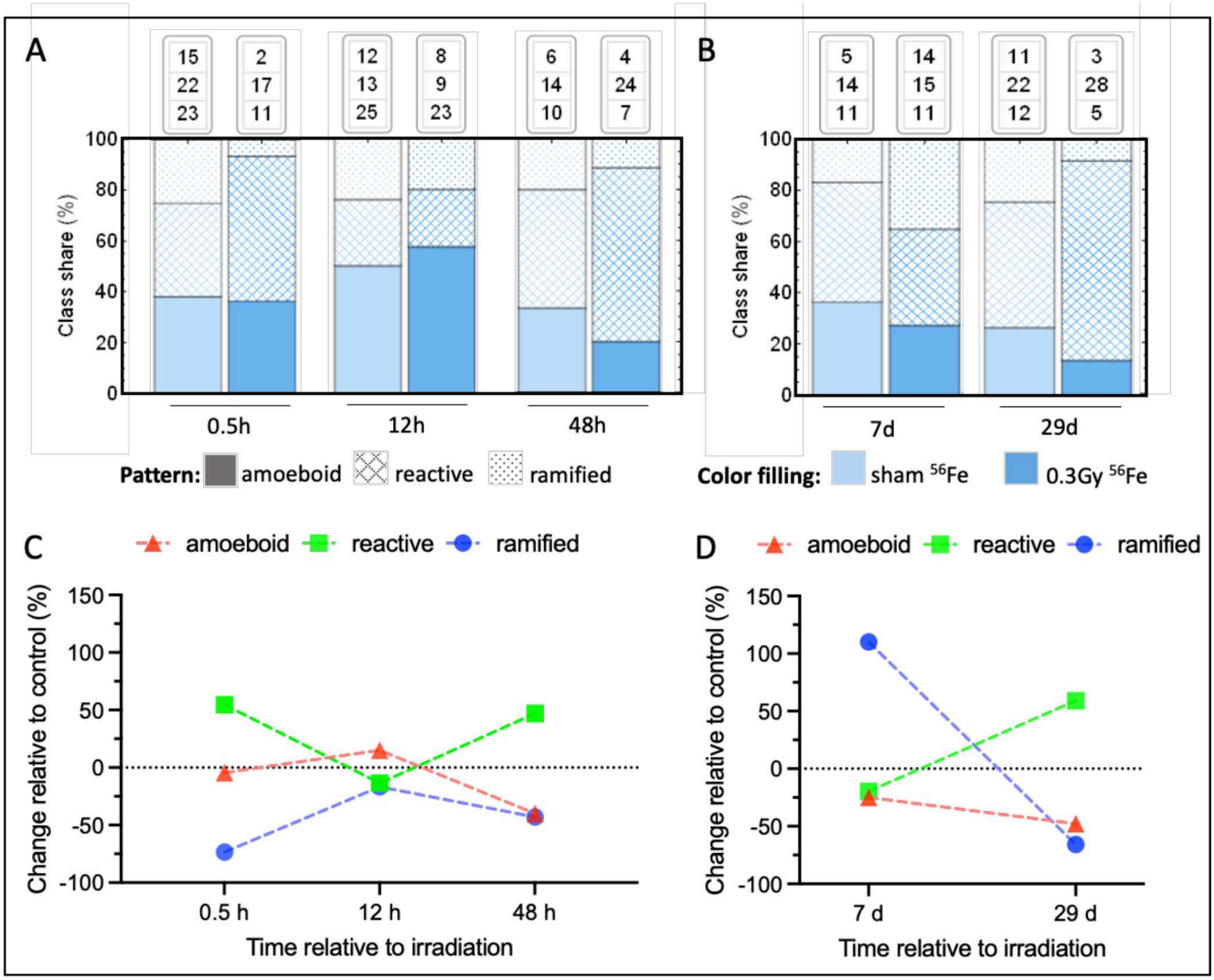

Figure 36 Morphological classification and dynamics of microglia after exposure to 0.3 Gy ^{56}Fe-ions. (A-B) Distribution of microglial morphological phenotypes (ramified, reactive, and amoeboid) in OHSCs following sham or 0.3 Gy ^{56}Fe-ion irradiation. (A) Short-term response (0.5 - 48 h) and (B) long-term response (7 - 29 d) post-irradiation showing class share percentages, with absolute cell counts per class indicated above bars. (C-D) Temporal changes in microglial subpopulations expressed as fold change relative to sham-irradiated controls for (C) short-term and (D) long-term observations. Morphological classification was performed using semi-automated list population with manually allocated training data (100 cells per class). Data represent mean values from 3-4 independent experiments, analyzing 9 OHSCs total with 6-45 microglia per condition. The analysis provides quantitative assessment of microglial morphological responses to low-dose IR over time.

3.6.4 Inflammatory cytokine IL-6 in ^{56}Fe-ion irradiated OHSCs

In the following chapter, the impact of 0.3 Gy ^{56}Fe-ion radiation on the pro-inflammatory marker IL-6 was investigated (Figure 37). In ^{56}Fe-ion irradiated samples, increased IL-6 levels were detected when compared to sham irradiated OHSCs over the 29-day observation period (Figure 37A-B). A significant increase in IL-6 levels was observed at 0.5 hours ($p = 0.002$) post irradiation, respectively. Differences at 12 hours were high but not statistically significant, due to high

variances between the experiments. Nonetheless, a clear increase 12 h post irradiation was detected. From 48 hours until the end of the measurements, the IL-6 values remained just above the control values and in the range as before irradiation (- 72 hours) (Figure 37B).

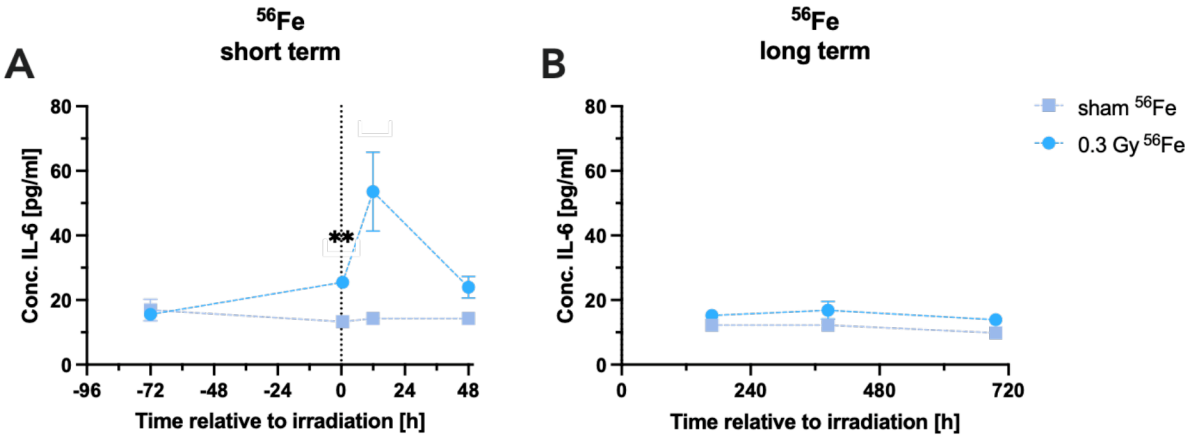

Figure 37 IL-6 concentration in OHSC supernatant over (A) short term and (B) long term observation period exposed to sham or 0.3 Gy ^{56}Fe-ions. IL-6, was accumulated over a period of 72 h per sampling time and measured in pg/mL with a high-sensitivity ELISA assay. Error bar: mean ± SEM. N = 3, i = 3, s = 9. Statistics performed by unpaired t-test with Welch's correction, comparing each group to 0 Gy, sham irradiation control at corresponding time ** $p < 0.001$.

The data in Figure 38 reveal a dose-dependent increase in IL-6 production following ^{56}Fe-ion irradiation. The 3.0 Gy dose consistently induced higher IL-6 levels compared to the 0.3 Gy dose and sham irradiation. A notable peak in IL-6 concentration was observed at 12 hours post-irradiation for both 0.3 Gy and 3.0 Gy doses, with the 3.0 Gy dose eliciting a particularly pronounced response. This peak was followed by a gradual decline in IL-6 levels, though they remained elevated compared to sham controls up to 48 hours post-irradiation. These results suggest that ^{56}Fe-ion radiation induces a rapid and dose-dependent inflammatory response in OHSCs, as indicated by increased IL-6 production, with the effect persisting for at least 48 hours after exposure.

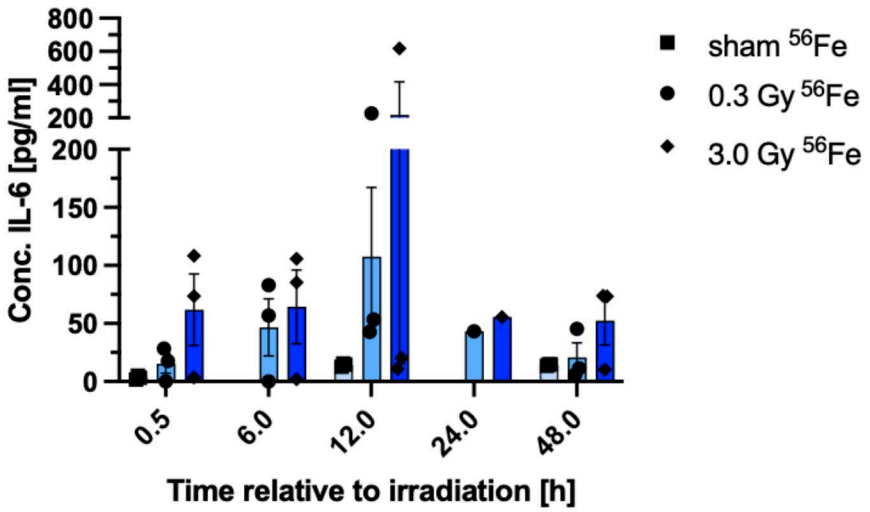

Figure 38 Temporal dynamics of IL-6 concentration in tissue culture supernatant of ^{56}Fe-ion irradiated OHSCs. OHSCs were exposed to sham irradiation

3.6.5 Effects of synthetic cannabinoid-receptor ligands on ^{56}Fe-ion irradiated OHSCs

The following investigated the effects of synthetic cannabinoid receptor ligand AbnCBD and GP1a on irradiated OHSCs, similar to previous studies conducted with X-rays. Specifically, this study examines the dose-dependent impact of GP1a and AbnCBD on the IL-6 concentration (Figure 39). The effect of 0.3 Gy or 3.0 Gy ^{56}Fe-ions on IL-6 concentration 12 hours post irradiation, did not reveal significant alterations in the IL-6 levels when compared to the DMSO control group. DMSO treated OHSCs showed a four-fold increase in IL-6 concentration from 14.29 ± 1.43 pg/mL to 53.54 ± 21.14 pg/mL after low-dose iron irradiation. A further ten-fold rise of the dose led to a decrease in IL-6 levels compared to 0.3 Gy irradiation dose. In contrast, AbnCBD treatment led to a dose-dependent increase in secreted IL-6 levels (sham = 39.41 ± 28.38 pg/mL, 0.3 Gy = 71.48 ± 43.149 pg/mL, 3.0 Gy = 98.65 pg/mL). The IL-6 levels of GP1a treated OHSCs varied from 16.92 ± 5.824 pg/mL to 82.65 ± 106.69 pg/mL and 62.33 pg/mL over increased radiation dose with high deviations at 0.3 Gy (Figure 39). Since 3.0 Gy ^{56}Fe-ion irradiation could only be tested in one run with three OHSCs, the results are only an indication of the trend.

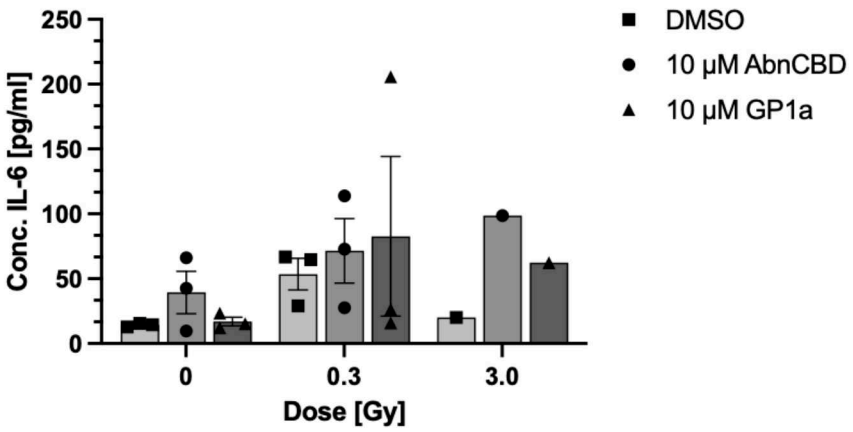

Figure 39 Dose-dependent IL-6 concentration in tissue culture supernatant of OHSC 12 h post ^{56}Fe-ion exposure and subsequent treatment with 10 µM of cannabinoid-receptor agonists GP1a and AbnCBD. Error bars: mean ± SD. N = 1-3, i = 1-3, s =3-9; Statistics performed by 2way ANOVA (Sidak's multiple comparison). Comparisons were conducted between treated sham vs. irradiated groups.

The following two chapters elucidate the specific effects of the each cannabinoid-receptor ligands GP1a and AbnCBD on ^{56}Fe-ion irradiated OHSCs.

3.6.5.1 Effects of GP1a treatment after exposure to 0.3 Gy ^{56}Fe-ion radiation

The effects of GP1a on ^{56}Fe-ion irradiated OHSCs were firstly investigated by measuring the total cell count (Figure 40). For the GP1a treated samples, there was a peak value of 501.33 ± 27.38 at 12 hours and a minimum value of 305.333 ± 75.72 at 7 days (168 h) with a minor increase at 29 days (696 h) post irradiation compared to the irradiated only controls. Overall, the trend of the total cell counts in GP1a treated OHSCs was not significantly different from the DMSO treated controls.

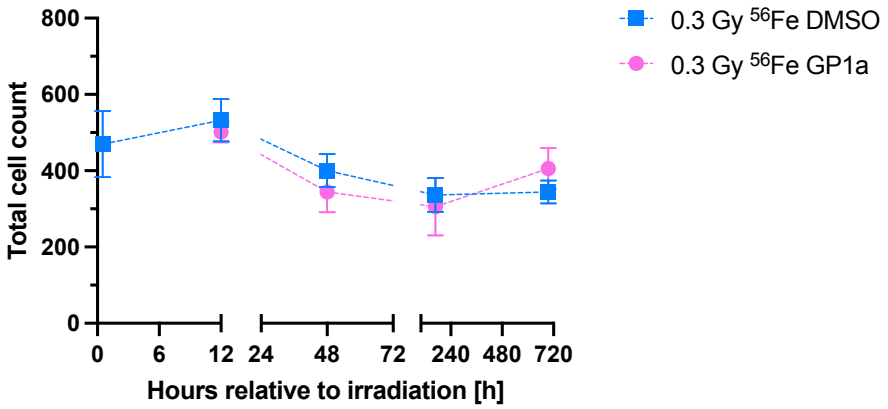

Figure 40 Total cell count in dentate gyrus of sham and 0.3 Gy ^{56}Fe-ion irradiated OHSCs treated with 10 µM GP1a over the entire cultivation time. Cell numbers were determined by DAPI staining of 350 µm whole mount OHSCs. Error bars: mean ± SEM. N = 3, i = 1, s = 3. Statistics performed by unpaired t-test with Welch's correction, comparing irradiated samples at each time point to sham irradiated OHSC at associated experimental time point.

The analysis of microglial and PI+ cell densities in OHSCs treated with 10 µM GP1a following 0.3 Gy ^{56}Fe -ion exposure revealed several temporal patterns (Figure 41A). Microglial cell density in GP1a-treated OHSCs maintained comparable levels to the DMSO control throughout the observation period, as demonstrated in panels A and B. The temporal profile showed an initial decrease in microglial density during the first 12 hours post-irradiation, notably without a corresponding increase in dead cell numbers (Figure 41A).

PI+ cell density measurements showed equivalent values between control and GP1a-treated samples at the 12-hour timepoint, followed by a marked decrease at 48 hours post-irradiation in GP1a-treated samples. Substantial variations were observed within experimental conditions, particularly prominent between 48 hours and 7 days post-irradiation, occurring independently of receptor antagonist treatment (Figure 41B). The long-term observations revealed high variability between experiments, with a notably large deviation at 29 days post-irradiation in GP1a-treated samples, where PI+ cells exhibited an approximately 40-fold increase relative to the irradiated, DMSO-treated control group (Figure 41C).

The density profiles of both microglia and PI+ cells demonstrated parallel trajectories throughout the experimental timeline. A notable observation was the significant reduction in microglial cells during the initial 12 hours following 0.3 Gy ^{56}Fe -ion irradiation, which occurred without a concurrent increase in cell death markers (Figure 41B).

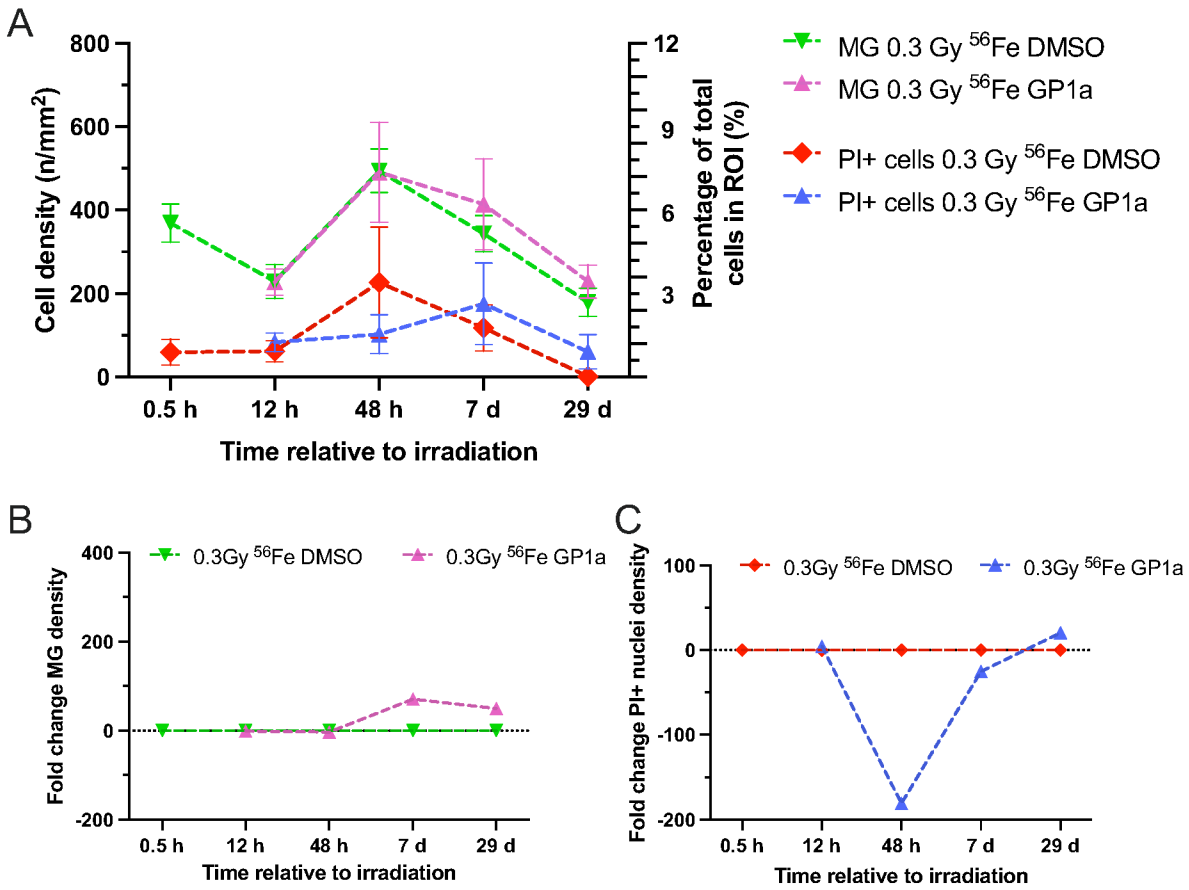

Figure 41 Microglia and PI+ cell densities in dentate gyrus of OHSCs treated with 10 µM GP1a. (A) Cell density dynamics following 0.3 Gy ^{56}Fe-ion exposure monitored over 29 days post-irradiation, quantified through immunofluorescent image analysis and normalized to dentate gyrus area (mm2). (B) Temporal changes in microglia cell density expressed as fold change relative to irradiated, DMSO-treated controls. (C) Fold change in PI+ cell density compared to irradiated, DMSO-treated controls across timepoints. Data represent mean ± SEM from three independent experiments (N = 3, i = 3, s = 9). Statistical analysis performed using unpaired t-test with Welch's correction, comparing GP1a treatment to DMSO control at each timepoint.

The distribution of morphological microglia classes across multiple timepoints of OHSCs treated with GP1a and exposed to 0.3 Gy ^{56}Fe-ion radiation is depicted in Figure 42. The data is displayed as both absolute proportions (panels A and B) and relative changes compared to controls (panels C and D).

In the acute phase (0.5 h - 48 h), the distribution patterns showed temporal dynamics. At 0.5 hours, control samples exhibited approximately 35 % amoeboid microglia, while at 12 hours both control and GP1a-treated samples demonstrated elevated amoeboid populations reaching 55 - 80 %. By 48 hours, the amoeboid population decreased to approximately 20 % in both conditions. The reactive phenotype constituted 40 - 60 % of the population across all acute timepoints, with slight variations between control and GP1a treatment. Ramified microglia showed the most pronounced

differences between conditions at 12 hours, where GP1a-treated samples displayed lower proportions compared to controls.

For chronic timepoints (7 d -29 d, Figure 42B), the distribution patterns evolved further. At 7 days, both conditions showed comparable proportions of all three phenotypes, with reactive microglia comprising approximately 40 % of the population. By 29 days, the distribution remained relatively stable in both conditions, though with slight variations in the reactive and ramified populations.

The relative changes normalized to controls (Figure 42C-D) revealed distinct temporal patterns for each morphological class. The amoeboid population in GP1a-treated samples showed a progressive increase from 12 hours to 48 hours (panel C), reaching approximately +65 % above control levels. The reactive population remained relatively stable around control levels, while the ramified population showed the most dramatic fluctuations, decreasing by approximately 80 % at 12 hours before returning to control levels by 48 hours. In the chronic phase (panel D), these trends partially reversed, with the ramified population showing an increase above control levels by 29 days, while the reactive population decreased below control levels.

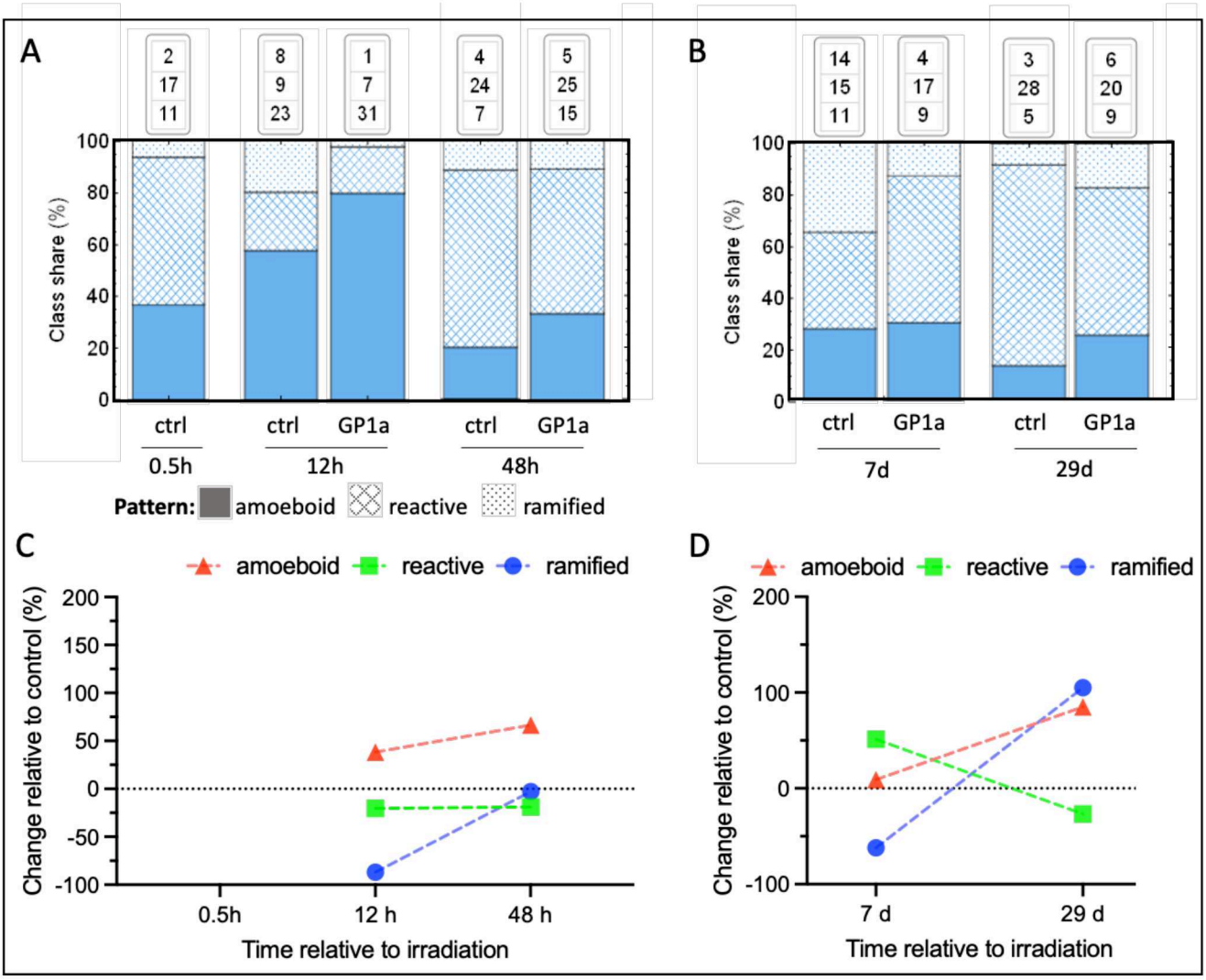

Figure 42 Temporal dynamics of microglial morphological classes following 0.3 Gy ^{56}Fe-ion radiation exposure and GP1a treatment. Distribution of microglial phenotypes (amoeboid, reactive, and ramified) OHSCs is shown as class share percentages for (A) acute phase (0.5 - 48 hours) and (B) chronic phase (7 - 29 days) post-irradiation. OHSCs were treated with either 10 µM GP1a or vehicle control (ctrl). Numbers above bars represent total cells analysed per condition. Analysis was performed using semi-automated classification based on training data from 100 manually classified cells per morphological category (n=3-31 OHSCs per condition, approximately 25-60 microglia per region of interest). (C, D) Relative changes in microglial subpopulations compared to time-matched controls, expressed as percentage change from control values for acute (C) and chronic (D) timepoints. Data points represent mean values for each morphological class. Treatment groups were compared to their respective vehicle-treated, sham-irradiated controls at each timepoint.

The IL-6 concentration of 0.3 Gy ^{56}Fe-ion irradiated and GP1a treated OHSCs were compared to their respective DMSO treated controls (Figure 43). The results for the short period after irradiation showed an increase but strong variances between the IL-6 concentrations of the conditions, especially after 12 hours (Figure 43A). In the long term, there is a consistently lower IL-6 concentration in the GP1a treated OHSCs, which was significant on days 7 and 29 ($p = 0.03$ and $p = 0.02$) (Figure 43B).

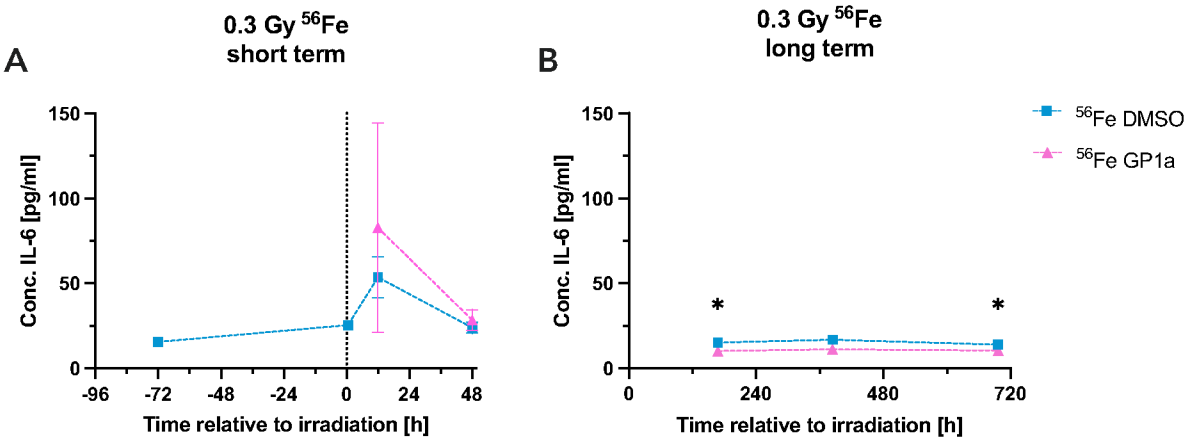

Figure 43 IL-6 concentration in 0.3 Gy to ^{56}Fe-ion radiation samples with and without 10 µM of CB2 receptor agonist GP1a. IL-6, was accumulated over a total period of 72 h per sampling time point and measured in pg/mL with a high-sensitivity ELISA assay. The data presented for -72 h and 0.5 h DMSO were collected during the same experimental procedure but recurring in this figure. N = 3, i = 3, s = 9. Error bars: mean ± SEM. Statistics performed by unpaired t-test with Welch's correction, comparing each group to 0.3 Gy DMSO controls at corresponding time. * $p < 0.05$.

3.6.5.2 Effects of AbnCBD treatment after exposure to ^{56}Fe-ion radiation

The total cell count was determined for the ^{56}Fe-ion irradiated and AbnCBD treated OHSCs (Figure 44). A high variance was observed in the AbnCBD-treated samples, but otherwise, there was no statistically significant difference compared to the untreated group. For both groups the maximum values around 600 cells were detected after 12 hours and then decreased to an average value of approx. 376 cells during the long-term observation period.

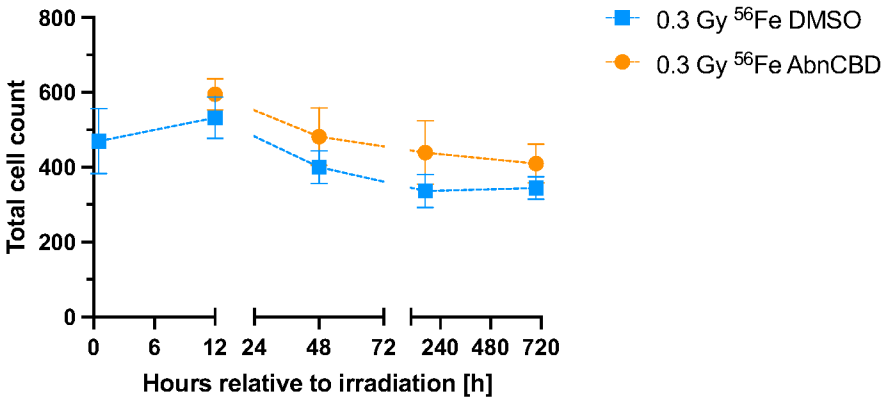

Figure 44 Total cell count in dentate gyrus of sham and 0.3 Gy ^{56}Fe-ion irradiated OHSCs treated with 10 µM AbnCBD over the entire cultivation time. Cell numbers were determined by DAPI staining of 350 µm whole mount OHSCs. Error bars: mean ± SEM. N = 3, i = 1, s = 3. Statistics performed by unpaired t-test with Welch's correction, comparing irradiated samples at each time point to sham irradiated OHSC at associated experimental time point.

The cell density analysis of ^{56}Fe-ion irradiated and AbnCBD-treated OHSCs is depicted in the following graph (Figure 45). The figure presents quantitative analyses of cell density dynamics in OHSCs following exposure to 0.3 Gy ^{56}Fe-ion radiation and treatment with AbnCBD or DMSO vehicle control over multiple timepoints (0.5 hours to 29 days). Data is presented as absolute cell densities (panel A) and relative changes compared to controls (panels B and C).

Panel A demonstrates temporal changes in both microglial and PI+ cell densities. The DMSO-treated control group showed initial microglial densities of approximately 375 cells/mm^2 at 0.5 hours, decreasing to about 225 cells/mm^2 at 12 hours, followed by a pronounced peak of approximately 500 cells/mm^2 at 48 hours. Subsequently, the density gradually declined to approximately 175 cells/mm^2 by 29 days. The AbnCBD-treated group exhibited consistently lower microglial densities compared to controls, particularly between 12 hours and 7 days post-irradiation, with the difference being statistically significant.

PI+ cell densities remained substantially lower in AbnCBD-treated samples compared to DMSO controls throughout the observation period. Control samples showed a peak PI+ cell density of approximately 225 cells/mm^2 at 48 hours, while AbnCBD-treated samples maintained consistently low PI+ cell densities below 50 cells/mm^2.

The fold change analysis (panels B and C) highlights these differences relative to controls. Panel B shows the relative changes in microglial density, with AbnCBD treatment resulting in reduced densities until 7 days post-irradiation, followed by a slight increase at 29 days. Panel C illustrates the marked reduction in PI+ cells in AbnCBD-treated samples, reaching a maximum decrease of approximately 150 % at 48 hours post-irradiation, followed by a gradual return to control levels by 29 days.

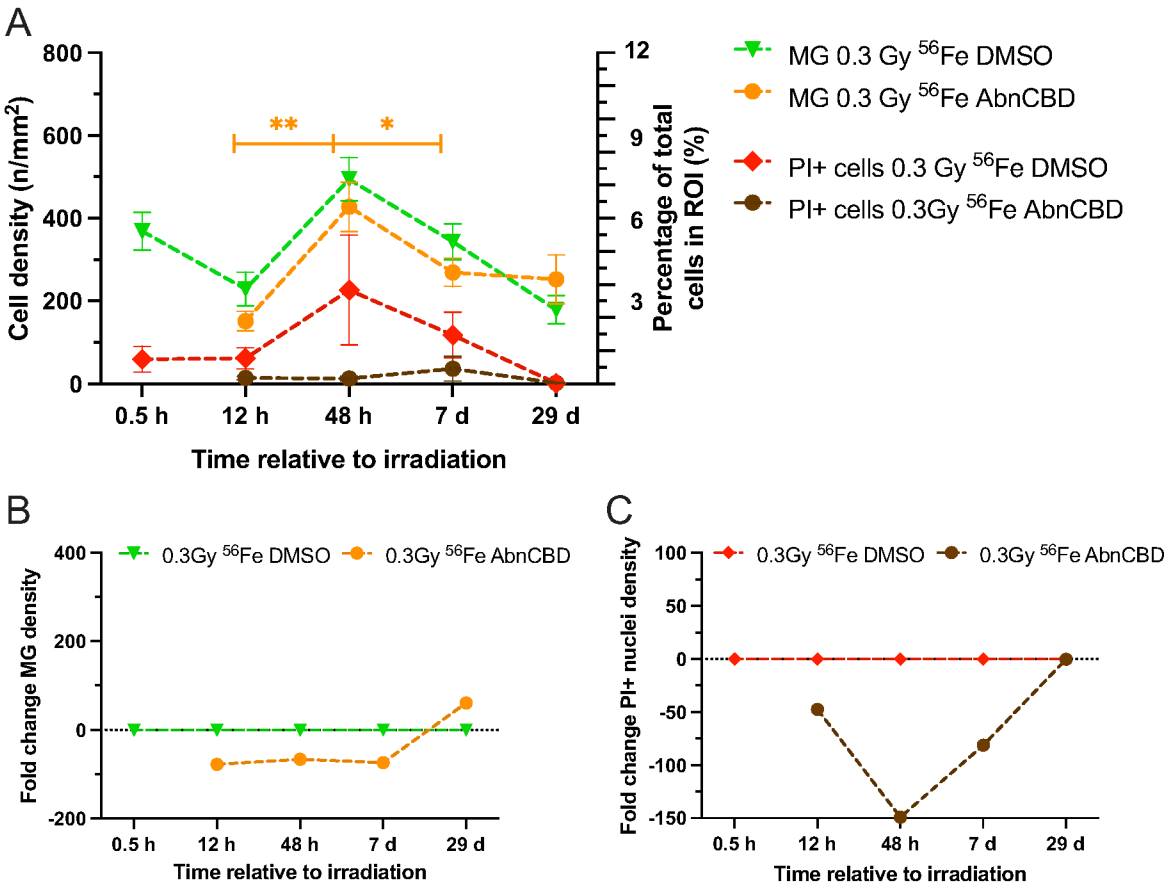

Figure 45 Temporal dynamics of microglia and cell death following ^{56}Fe-ion radiation exposure and AbnCBD treatment. (A) Quantitative analysis of microglia (MG) and propidium iodide-positive (PI+) cell densities in the dentate gyrus of OHSCs following 0.3 Gy ^{56}Fe-ion radiation exposure and treatment with either 10 µM AbnCBD or vehicle control (DMSO). Cell densities were monitored from 0.5 hours to 29 days post-irradiation and determined by automated analysis of immunofluorescent images, normalized to the dentate gyrus area (cells/mm^2). (B) Relative changes in microglial density expressed as fold change compared to time-matched, sham-irradiated controls. (C) Temporal profile of cell death, shown as fold change in PI+ cell density relative to sham-irradiated controls. Data represent mean ± SEM from three independent experiments (N=3) with three OHSCs per condition and nine regions of interest per slice (i=3, s=9). Statistical significance was determined using unpaired t-test with Welch's correction (*$p < 0.05$, **$p < 0.001$ compared to time-matched DMSO controls).

In the following section, the quantitative analyses of microglial morphological classes in OHSCs, irradiated with 0.3 Gy ^{56}Fe-ions and treated with 10 µM AbnCBD across multiple time points are presented (Figure 46). The data is displayed as both class-share percentages (panels A and B) and relative changes compared to DMSO treated controls (panels C and D).

In the acute phase (0.5 hours-48 hours, panel A), AbnCBD-treated samples exhibited distinct distribution patterns. At 12 hours post-irradiation, AbnCBD treatment resulted in approximately 75 % amoeboid microglia, compared to approximately 55 % in controls. Concurrently, the proportion of ramified microglia was approximately 10 % lower in AbnCBD-treated samples

compared to controls. At 48 hours, the pattern shifted, with AbnCBD-treated samples showing decreased reactive microglia proportions and increased ramified microglia compared to controls. During the chronic phase (7 - 29 days, Figure 46B), the distribution patterns evolved further. At 7 days, AbnCBD-treated samples showed reduced amoeboid microglia proportions compared to controls. By 29 days, all three morphological classes showed marked differences from controls, with AbnCBD treatment resulting in approximately 40 % amoeboid, 40 % reactive, and 20 % ramified microglia.

The relative changes normalized to controls (Figure 46 C and Figure 46D) revealed distinct temporal patterns. In the acute phase (panel C), ramified microglia showed the biggest change, increasing by approximately 175 % at 48 hours in AbnCBD-treated samples. During the chronic phase (Figure 46D), both amoeboid and ramified populations showed substantial increases (approximately 200 % and 150 % respectively) by 29 days, while the reactive population decreased by approximately 50 %.

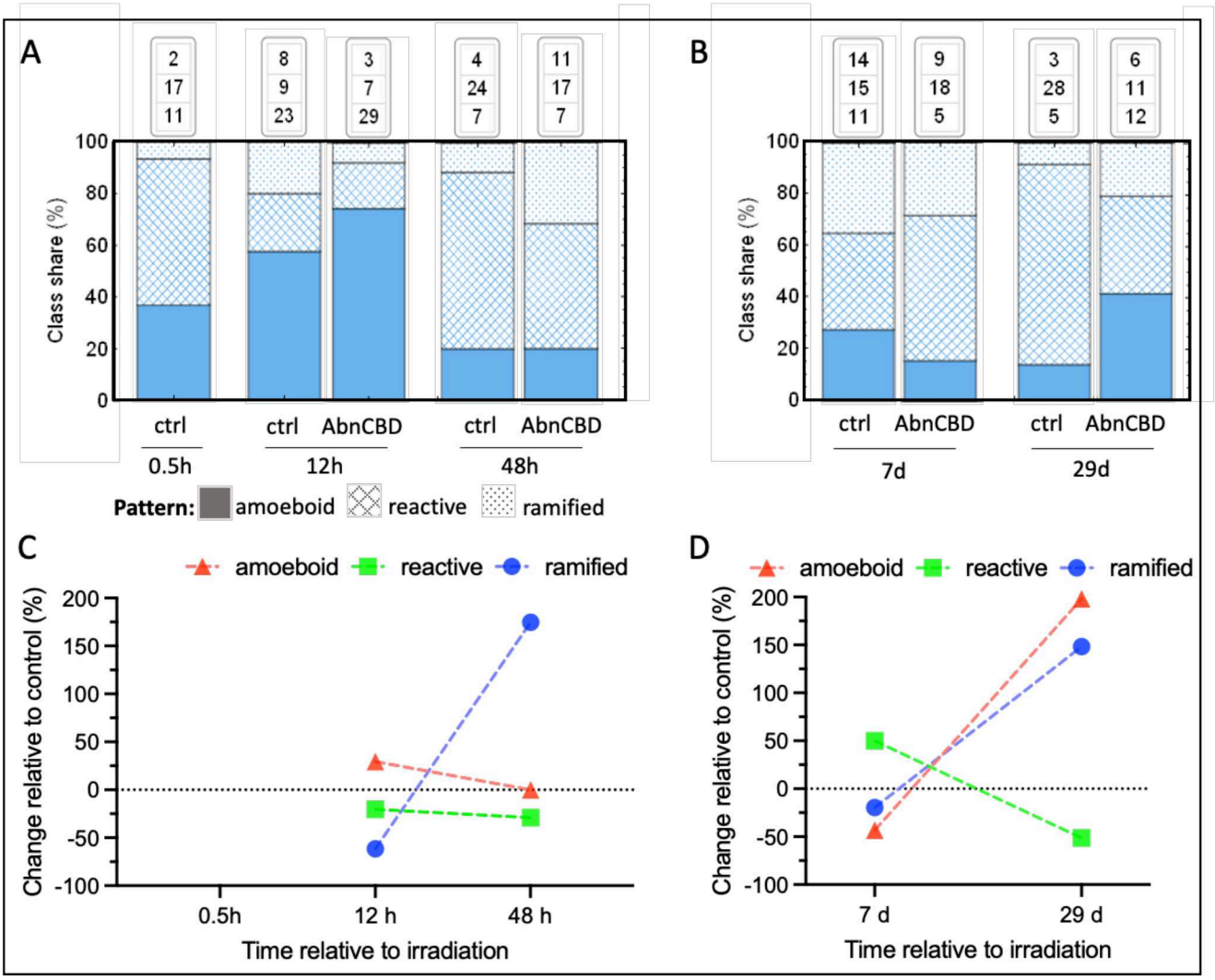

Figure 46 Temporal evolution of microglial morphological phenotypes following ^{56}Fe-ion radiation exposure and AbnCBD treatment. Quantitative analysis of microglial morphological classes (amoeboid, reactive, and ramified) in OHSCs following 0.3 Gy ^{56}Fe-ion radiation exposure and treatment with 10 µM AbnCBD or vehicle control. (A) Distribution of morphological classes during acute phase response (0.5 - 48 hours) and (B) chronic phase response (7 - 29 days) post-irradiation, expressed as percentage of total microglia population. Classification was performed using a semi-automated approach based on training data from 100 manually classified cells per morphological category. Numbers above bars indicate total cells analyzed per condition (3-4 independent experiments, 9 OHSCs per condition, approximately 25-60 microglia per region of interest). (C, D) Temporal changes in microglial subpopulations relative to time-matched, sham-irradiated controls, expressed as percentage change from control values for acute (C) and chronic (D) timepoints. Control measurements from previous experiments were included to enable direct comparability across timepoints.

The IL-6 secretion of AbnCBD treated OHSCs increased during the early period post irradiation and showed a high variance at 48 hours (Figure 47A). However, these differences were diminished from days 7 on when IL-6 concentration of AbnCBD treated OHSCs equaled the DMSO treated ones at very low concentrations below 29 pg/mL (Figure 47B).

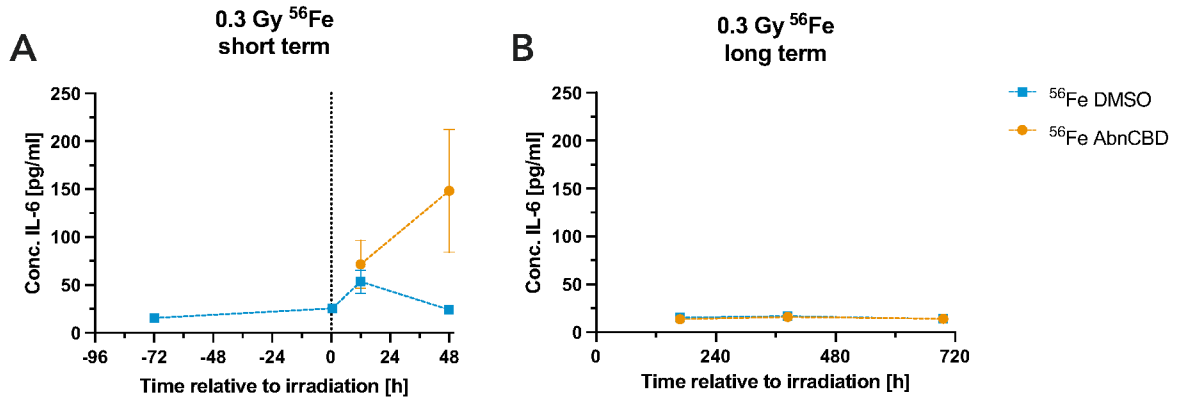

Figure 47 IL-6 concentration in 0.3 Gy to ^{56}Fe –ion radiation samples with and without 10 µM of CB2 receptor agonist AbnCBD. IL-6, was accumulated over a total period of 72 h per sampling time point and was measured with a high-sensitivity ELISA assay. The data presented for -72 hours and 0.5 hours DMSO were collected during the same experimental procedure but recurring in this figure. N = 3, i = 3, s = 9. Error bars: mean ± SEM. Statistics performed by unpaired t-test with Welch's correction, comparing each group to 0.3 Gy DMSO controls at corresponding time.

3.7 Summary of Biological Effects of Ionizing Radiation and Synthetic Cannabinoid-Receptor Ligand Treatment on OHSCs

The previous chapters provided a detailed analysis of the impact of a low, single dose of two types of radiation on the inflammatory response of microglia cells in the dentate gyrus of OHSCs. The following Table 7 provides a simplified summary of these results to compare the functional changes in microglia between loosely (X-ray) and densely (^{56}Fe-ions) ionizing radiation compared to their sham irradiated controls. The time point 0.5 hours was separated from the short and the long-term periods as an immediate time-point to the radiation and values within each group were combined into average values. All differences above 20 % were assigned to the next valuation level.

Analysis of differential responses to radiation exposure and cannabinoid receptor ligand treatment in hippocampal tissue reveals distinct temporal and treatment-specific patterns (Table 7). Following 0.3 Gy exposure to either X-ray or ^{56}Fe-ion irradiation, the tissue response patterns were monitored at early (12-48 hours) and late (7-29 days) timepoints, with an additional very early (0.5 hours) assessment for radiation-only effects.

In radiation conditions, X-ray exposure initially induced acute cell death (increased PI+ density) at 0.5 hours post-irradiation, accompanied by microglial activation (increased amoeboid morphology). This immediate response was followed by decreased cell death markers at later timepoints, with increased microglial density emerging at 7-29 days. Notably, X-ray exposure consistently decreased IL-6 expression across all timepoints. Gene expression analysis at 12 – 48 hours revealed decreased markers for neuronal differentiation (*otx2*), memory (*igf2*), and cognition (*stra6*), concurrent with increased G-protein receptor activity (*htr7*) and oxidative stress-induced cell death pathways (*mmp3*).

Table 7 Simplified summary of biological changes in the dentate gyrus of OHSCs exposed to 0.3 Gy X-ray or ^{56}Fe-ion radiation compared to sham irradiated controls. Responses were evaluated at three timepoints: very early (0.5 hours), early (12-48 hours), and late (7-29 days) post-irradiation. Parameters assessed include total cell population, cell death (PI+ density), microglial density and morphological states (amoeboid, reactive, ramified), inflammatory marker (IL-6), and gene expression related to neuronal differentiation (otx2), memory (igf2), cognition and learning (stra6), G-protein receptor activity (htr7), and oxidative stress-induced cell death (mmp3). Symbols indicate changes relative to non-irradiated controls: (+) increase, (-) decrease, (=) no change, (+/=) increase or no change, (-/=) decrease or no change, and gray boxes indicate parameters not assessed. The temporal and radiation type-specific responses suggest distinct mechanisms of radiation-induced effects between X-ray and ^{56}Fe-ion exposure.

Radiation	**X-ray** 0.3 Gy 0.5 h	**X-ray** 0.3 Gy 12 - 48 h	**X-ray** 0.3 Gy 7 - 29 d	**^{56}Fe** 0.3 Gy 0.5 h	**^{56}Fe** 0.3 Gy 12 - 48 h	**^{56}Fe** 0.3 Gy 7 - 29 d
Total cells	=	=	=	=	=	- / =
PI+ density (dead cells)	+	-	-	-	+ / =	- / =
Microglia density	=	=	+	=	=	- / =
amoeboid	+	=	=	=	=	=
reactive	=	=	=	+	=	=
ramified	=	=	=	-	=	=
IL-6	-	-	-	+	+	+ / =
neuronal cell differentiation *(otx2)*		-				
memory *(igf2)*		-				
cognition, learning *(stra6)*		-				
G-protein receptor activity *(htr7)*		+				
oxidative stress induced cell death *(mmp3)*		+				

Legend
+ → more than control
- → less than control
= → equal to control
+/= → more or equal to control
-/= → less or equal to control

^{56}Fe-ion irradiation exhibited a different temporal profile, characterized by sustained IL-6 elevation across all timepoints. Immediate microglial response (0.5 hours) showed increased reactive morphology with decreased ramification, while later timepoints (7 - 29 days) demonstrated reduced total cells, cell death markers, and microglial density.

Treatment with 10 µM GP1a following radiation exposure showed radiation type-specific effects (Table 3). Following X-ray exposure, GP1a treatment initially showed decreased or maintained total cell populations and cell death markers, while favouring ramified and reactive microglial states. Late-phase effects displayed increased cell death and IL-6 expression, with decreased ramified morphology. Under ^{56}Fe-ion radiation conditions, GP1a maintained stable total cell populations but showed limited efficacy in preventing late-phase cell death. The compound demonstrated suppressive effects on GPR55 expression following X-ray exposure.

Table 8 Simplified summary of biological effects in the dentate gyrus of OHSCs exposed to 0.3 Gy X-ray or ^{56}Fe-ion radiation with subsequent GP1a (10 µM) treatment compared to irradiated, DMSO controls. Responses were evaluated at early (12-48 hours) and late (7-29 days) timepoints post-irradiation. Parameters assessed include total cell population, cell death (PI+ density), microglial density and morphological states (amoeboid, reactive, ramified), inflammatory marker (IL-6), and cannabinoid receptor expression (CB1R, CB2R, GPR55). Symbols indicate changes relative to irradiated, vehicle-treated controls: (+) increase, (-) decrease, (=) no change, (+/=) increase or no change, (-/=) decrease or no change, (=/-) equal or decrease, and gray boxes indicate parameters not assessed. The differential responses between radiation types and timepoints suggest distinct cellular mechanisms in radiation-induced effects and their modulation by GP1a in the dentate gyrus.

10 µM GP1a	**X-ray** 0.3 Gy 12 - 48 h	**X-ray** 0.3 Gy 7 - 29 d	**^{56}Fe** 0.3 Gy 12 - 48 h	**^{56}Fe** 0.3 Gy 7 - 29 d
Total cells	**- / =**	**+ / =**	**=**	**=**
PI+ density (dead cells)	**- / =**	**+**	**= / -**	**+**
Microglia density	**=**	**- / =**	**=**	**=**
amoeboid	**-**	**=**	**=**	**=**
reactive	**+**	**=**	**=**	**=**
ramified	**+**	**-**	**=**	**=**
IL-6	**=**	**+**	**=**	**-**
***cnr1* (CB_1R)**	**=**			
***cnr2* (CB_2R)**	**=**			
***gpr55* (GPR55)**	**-**			
Legend	**+** → more than control **-** → less than control **=** → equal to control		**+/=** → more or equal to control **-/=** → less or equal to control	

AbnCBD treatment (10 µM) demonstrated distinct effects from GP1a (Table 9). With X-ray exposure, AbnCBD maintained total cell populations while increasing ramified microglial morphology and modulating IL-6 expression at early timepoints. CB2 receptor expression was elevated, suggesting engagement of anti-inflammatory pathways. Under ^{56}Fe-ion radiation conditions, AbnCBD treatment preserved total cell populations while preventing cell death, particularly at early timepoints.

Table 9 Simplified summary of biological effects in the dentate gyrus of OHSCs exposed to 0.3 Gy X-ray or 56Fe-ion radiation with subsequent abnormal cannabidiol (AbnCBD, 10 µM) treatment compared to irradiated, DMSO controls. Responses were evaluated at early (12-48 hours) and late (7-29 days) timepoints post-irradiation. Parameters assessed include total cell population, cell death (PI+ density), microglial density and morphological states (amoeboid, reactive, ramified), inflammatory marker (IL-6), and cannabinoid receptor expression (CB1R, CB2R, GPR55). Symbols indicate changes relative to irradiated, vehicle-treated controls: (+) increase, (-) decrease, (=) no change, (+/=) increase or no change, (-/=) decrease or no change, and gray boxes indicate parameters not assessed. The differential responses between radiation types and timepoints suggest distinct cellular mechanisms in radiation-induced effects and their modulation by AbnCBD in the dentate gyrus.

10 µM AbnCBD	**X-ray** 0.3 Gy 12 - 48 h	**X-ray** 0.3 Gy 7 - 29 d	**^{56}Fe** 0.3 Gy 12 - 48 h	**^{56}Fe** 0.3 Gy 7 - 29 d
Total cells	=	=	+	+
PI+ density (dead cells)	-	+ / =	-	-
Microglia density	=	- / =	=	=
amoeboid	-	=	=	=
reactive	=	=	=	=
ramified	+	=	=	=
IL-6	+ / =	=	+	=
***cnr1* (CB_1R)**	=			
***cnr2* (CB_2R)**	+			
***gpr55* (GPR55)**	=			
Legend	+ → more than control - → less than control = → equal to control		+/= → more or equal to control -/= → less or equal to control	

These findings demonstrate complex, temporal- and radiation type-dependent responses in hippocampal tissue, with differential modulation by cannabinoid compounds, highlighting the intricate nature of radiation-induced effects and potential therapeutic interventions.

4 DISCUSSION, CONCLUSIONS AND OUTLOOKS

Space radiation presents a significant health risks to astronauts during missions beyond Low-Earth Orbit, particularly concerning CNS damage. While spacecraft provide some mechanical radiation protection, additional biopharmaceutical countermeasures are essential to cover the residual exposure risks and comprehensively safeguard astronaut health during prolonged space missions. This dissertation investigated how endocannabinoid system-targeting agents protect against radiation-induced damage from low-dose X-ray and ^{56}Fe-ion exposure, using murine organotypic hippocampal slice cultures.

4.1 OHSCs as a Model System for Neuroinflammation

OHSCs were employed as an experimental model due to their exceptional capacity to preserve hippocampal cytoarchitecture and recapitulate *in vivo* neuronal circuits, providing an unparalleled platform for investigating neuroinflammatory processes (Stoppini et al., 1991). During cultivation, the CA3 region demonstrated pronounced vulnerability, serving as the initial locus of necrosis following radiation exposure (Figure 6). This observation is strongly supported by multiple comprehensive studies that identified N-methyl-D-aspartate (NMDA) receptor-mediated excitotoxicity as a primary mechanism of neurodegeneration in CA3 (Concannon et al., 2008; Liang et al., 2020; Scharfman, 2007). The high density of mossy fiber terminals and heightened glutamate receptor expression in this region renders it particularly susceptible to excitotoxic damage, as demonstrated in both ischemic and radiation injury models (Holopainen et al., 2004; Koyama & Ikegaya, 2018). The convergence of critical neuronal pathways within this region may confer particular susceptibility to metabolic and excitotoxic insults, underscoring the necessity for targeted interventions to maintain hippocampal integrity.

OHSCs definitively replicate human CNS immune responses, as evidenced by comparable cytokine profiles and microglial activation patterns (Holopainen, 2005; Timmerman et al., 2018; Warden et al., 2023). This remarkable fidelity enhances their translational relevance, effectively bridging the gap between preclinical models and human clinical studies. The cultivation of intact OHSCs was consistently successful when stringent contamination safety protocols were maintained throughout the experimental timeline and when dissection was performed with precise technique—avoiding tissue overhangs and preventing excessive cutting depth into regions

intended for preservation. This methodological precision was critical for maintaining tissue viability and experimental reproducibility.

Notably, OHSCs represent a highly accessible and responsive model system for quantifying neuroinflammatory reactions to various stressors, offering substantial advantages over conventional *in vivo* approaches. The system permits direct visualization of cellular responses, simplified manipulation of the extracellular environment, and longitudinal monitoring capabilities that are challenging to achieve in traditional models. In our hands, OHSCs demonstrated remarkable long-term viability, with successful cultivation extending over 42 days, enabling comprehensive temporal studies of neuroinflammatory progression and resolution. Additionally, OHSCs strongly align with the 3Rs principles of animal research (replacement, reduction, refinement), significantly reducing animal usage while facilitating high-throughput screening of neuroprotective agents and inflammatory modulators.

4.1.1 Optimal conditions for OHSC stability

The study emphasized the critical importance of experimental protocols for maintaining OHSC viability. Early medium changes (e.g., 2 hours post-preparation) deviated from traditional methods (Stoppini et al., 1991), facilitating the removal of pro-inflammatory cytokines and accelerating tissue recovery. These adjustments significantly enhanced tissue stability, with full homeostasis achieved by 14 days *in vitro*. Consistent medium changes and adherence to optimized handling protocols were vital in preventing necrotic degeneration, underscoring the importance of experimental precision.

4.1.2 Innovations in microglial visualization

This study implemented methodological refinements for the visualization of microglial morphology. The transition from ionized calcium-binding adaptor molecule 1 (IBA1) immunofluorescence to isolectin B4 (IB_4) lectin staining facilitated improved imaging of thicker tissue sections (350 µm), enabling more comprehensive three-dimensional assessment of microglial architecture. The enhanced resolution and decreased inter-sample variability observed with this technique addresses previous methodological limitations, providing a more robust

analytical framework for the quantitative evaluation of microglial dynamics in response to inflammatory stimuli.

4.1.3 STRESS RESPONSE AND CELLULAR RESILIENCE

A critical component of this investigation was the systematic evaluation of OHSC stress responses during transportation and cultivation. The analysis of these responses revealed several important findings with implications for both terrestrial and space-based research applications.

4.1.3.1 Transport and Cultivation Stress Responses

Sham X-ray transport controls demonstrated remarkable cellular stability within OHSCs during the acute post-transport period (≤ 48 hours) (Figure 11). Quantitative analysis revealed a significant increase in total cell number between days 7 and 29 post-transport, despite unchanged microglial density during this interval (Figure 11B). Importantly, IL-6 concentrations and PI+ cell counts remained constant, indicating the absence of inflammatory activation in response to transport-induced mechanical stress (Figure 12, Figure 13C-D). These findings contrast with previous reports by Sheppard et al., 2018, which established correlations between neuroinflammation and microglia-mediated synaptic disruption. The here presented data instead demonstrate significant OHSC resilience to controlled mechanical stress, with no detectable neuroinflammatory responses or synaptic compromise over extended post-transport periods, highlighting the importance of optimized transport protocols in neuroinflammation studies.

The temporal dynamics of microglial responses were characterized by distinct patterns. During the initial 48 hours following transport to the heavy-ion accelerator facility, we observed significant fluctuations in microglial density (Figure 11, Figure 13). A marked decrease in microglial density at 12 hours post-transport likely resulted from extended extracellular exposure during transportation. Notably, microglial density increased significantly between 12 and 48 hours without concomitant elevations in IL-6 or PI+ cells, suggesting that the initial stress response did not precipitate cellular death, inflammatory cascade activation, or microglial proliferation. These observations align with findings from Li, Han, and Wang 2016, confirming that OHSCs exhibit dynamic yet resilient microglial responses to acute stressors, with subsequent stabilization following initial perturbations.

4.1.3.2 Neurogenesis Dynamics in OHSCs

The significant increase in total cell number observed at 29 days post-transport may be attributable to intrinsic neurogenic processes within the hippocampal formation. Multiple lines of evidence support the hypothesis that this cellular expansion reflects endogenous neurogenic rhythms preserved within the OHSC system. (Kamada et al., 2015) demonstrated that hippocampal slice cultures maintain neurogenic capacity for extended periods, with peaks of neuroblast proliferation occurring in cyclical patterns approximately every 28 - 30 days. This timeframe corresponds closely with our observation of increased cellularity at day 29. Additionally, (Diaz et al., 2013) documented that OHSCs preserve the neurogenic niche of the DG, including maintenance of neural stem cell populations capable of generating new neurons even under *ex vivo* conditions.

The observed fluctuations in microglial density may also play a regulatory role in this neurogenic response. Microglial dynamics in the DG have been shown to modulate neural progenitor cell proliferation through the release of specific cytokines and growth factors. (Sierra et al., 2010) demonstrated that microglia regulate the balance between proliferation and apoptosis in the neurogenic niche, while Sato (2020) established that transient changes in microglial density can trigger compensatory neurogenesis through the release of insulin-like growth factor-1 (IGF-1) and brain-derived neurotrophic factor (BDNF)(K. Sato, 2015). The initial decrease followed by recovery of microglial density observed in our study may have initiated such a compensatory neurogenic response, manifesting as increased total cell numbers at the 29-day timepoint.

Additionally, (Gerlach et al., 2016) reported that temporary microglial depletion in the hippocampus leads to enhanced neurogenesis with a delayed onset of approximately 3 - 4 weeks, consistent with our observations. This effect appears to be mediated through reduced phagocytic activity and altered inflammatory signaling in the neurogenic niche. Our findings thus suggest that OHSCs maintain complex neuroimmune interactions that regulate neurogenesis, even under ex vivo conditions, further validating their utility as models for studying neuroinflammatory processes and neurogenic responses.

The established stability of OHSCs over 42 days in controlled environments suggests potential applications beyond conventional ground-based research paradigms. The microgravity environment of orbital platforms, including the International Space Station (ISS) and commercial research initiatives such as Yuri, presents unique opportunities to investigate the combined effects

of space radiation and altered gravitational forces on neural tissues. Given increasing accessibility to biological payload allocations on space missions, OHSCs represent a promising model system for examining neuroinflammatory and neurodegenerative processes under spaceflight conditions.

Integration of OHSCs into microgravity studies would facilitate investigation of potential synergistic effects between radiation-induced cellular damage and gravity-dependent neurobiological mechanisms. Such research has significant implications for both fundamental neuroscience and applied space medicine, potentially informing the development of neuroprotective countermeasures for long-duration missions beyond low Earth orbit.

4.1.4 Transport conditions and cannabinoid treatments: microglial dynamics and viability

Transport conditions influenced microglial density dynamics, particularly in heavy-ion accelerator sham controls where microglial density was persistently reduced. Despite stable IL-6 concentrations across all transport and treatment groups, microglial survival was impaired under extended transport conditions, highlighting the critical impact of environmental factors on cellular responses (Figure 13). Interestingly, the PI+ cell density remained relatively stable across all transport conditions. Both the X-ray and accelerator transport controls demonstrated similar dead cell rates, peaking at less than 3 % within 48 hours post-transport before returning to baseline levels by day 29.

4.2 Novel Microglial Morphological Classification

A novel classification system for microglial morphologies was developed using Nearest Centroid analysis, incorporating three key parameters: soma area, territorial area, and primary branch number. This approach revealed three distinct microglial phenotypes:

1. **Ramified Microglia**: Characterized by the smallest soma size (median 90 μm^2) and largest territorial area (median 1400 μm^2), representing a baseline surveillance state.
2. **Reactive Microglia**: Exhibiting intermediate soma size and territorial area, with notable cellular interactions and active engulfment processes.

3. **Amoeboid Microglia**: Displaying larger soma areas and reduced territorial sizes, indicative of an activated inflammatory state.

This classification enhances our understanding of microglial plasticity in response to radiation-induced stress, providing a quantitative framework for future investigations (Figure 10, Table 3). It is important to note that microglia are highly dynamic cells that continuously modify their morphology in response to their microenvironment and functional requirements. Therefore, any classification system represents merely a snapshot of a continuously evolving spectrum of phenotypes, with the strict differentiation and assignment through NC analysis to one of the three classes serving as a methodological approach to capture a specific moment in time.

NC analysis provides a robust and automated approach for classifying microglial morphology based on key quantitative morphological parameters. This method, widely used in image-based cell classification (Abdolhoseini et al., 2019) , relies on computing the Euclidean distance of individual cells to predefined centroids representing distinct morphological states. Our implementation of convex hulls around each centroid class further enhances this approach by establishing clear decision boundaries while acknowledging the continuous nature of morphological transitions. This geometric representation allows for the identification of cells in transitional states at hull boundaries and provides a quantitative measure of how typical a given cell is within its assigned phenotype, respecting the dynamic reality of microglial morphological plasticity. By training the algorithm on a reference dataset of manually classified microglia, NC analysis enables high-throughput, unbiased categorization of microglial phenotypes, improving reproducibility and reducing observer bias (Heindl et al., 2018).

For effective NC-based classification, confocal images must be acquired under standardized conditions to ensure comparability. This includes maintaining consistent imaging parameters such as laser intensity, z-stack resolution, and image scaling. Additionally, automated segmentation and preprocessing techniques, such as thresholding and watershed algorithms, help delineate individual microglial cells from the background (Khakpour et al., 2022; C. J. Murray et al., 2024).

Beyond morphology, automated confocal image analysis accelerates experimental throughput, allowing rapid assessment of radiation-induced changes across large datasets. When integrated with machine learning approaches, NC-based classification can further refine microglial subtype characterization, revealing subtle morphological transitions that might be overlooked in manual

analysis (Young & Morrison, 2018). This methodological framework is particularly advantageous for space radiation studies, where large-scale image datasets require efficient, high-throughput analysis pipelines.

Thus, NC analysis, combined with automated confocal image processing, presents a powerful tool for neuroinflammatory research, enabling standardized, objective classification of microglial states across experimental conditions. This approach enhances the interpretability of experimental findings and facilitates comparisons across different models of CNS damage, including space radiation exposure.

4.3 GP1a: A CB2 Receptor Ligand with Biased Signaling and Anti-Inflammatory Potential

GP1a, a synthetic CB2 receptor ligand, exhibits a biased signaling profile favoring G-protein pathways over β-arrestin recruitment, potentially allowing for inflammation modulation with reduced side effects Patel et al., 2023; Soethoudt et al., 2017. Our data demonstrated that GP1a-treated OHSCs maintained stable IL-6 concentrations and showed reduced microglial density during the short-term period post-irradiation. However, by day 29, GP1a-treated OHSCs exhibited a significant increase in PI-positive cells (≥ 6 %), indicative of potential long-term cytotoxic effects (Figure 13C, purple asterisks).

The data reveal a complex temporal relationship between GP1a treatment, microglial modulation, and cell death. While GP1a initially demonstrates anti-inflammatory properties by stabilizing IL-6 levels, the subsequent increase in PI-positive cells at day 29 suggests a delayed cytotoxic effect. This time-shifted pattern of cell death may be mechanistically linked to the early modulation of microglial activity by GP1a. Specifically, the initial suppression of microglial activation through CB2 receptor agonism might compromise the tissue's ability to maintain homeostasis under ongoing stress conditions, manifesting as increased cell death during later timepoints.

These findings underscore the complexity of targeting CB2 receptors for neuroinflammatory modulation and highlight the importance of monitoring long-term outcomes when evaluating potential therapeutic applications. The observed biphasic response—initial anti-inflammatory effects followed by delayed cytotoxicity—suggests that the timing and duration of CB2 receptor modulation are critical factors in determining overall tissue health and resilience.

4.4 AbnCBD: Cannabinoid Isomer with Neuroprotective and Anti-Inflammatory Effects

The endocannabinoid system plays a pivotal role in maintaining central nervous system homeostasis. Comprising cannabinoid receptors (CB1 and CB2) and endogenous ligands, it regulates inflammation, neuroprotection, and immune responses. Notably, CB2 receptors are highly expressed on microglia, particularly during inflammatory activation, while CB1 receptors and GPR55—an atypical cannabinoid receptor—play ancillary roles in modulating microglial activity.

AbnCBD, a synthetic isomer of cannabidiol, uniquely exerts its effects primarily through GPR55, which modulates pro-inflammatory responses and enhances neuroprotection. Unlike CB1 and CB2 agonists, AbnCBD selectively reduces pro-inflammatory mediators, such as tumor necrosis factor α (TNFα) and nitrite, while maintaining stable IL-6 concentrations (Grabiec et al., 2012; von Widdern et al., 2020) Notably, AbnCBD has demonstrated neuroprotective effects without triggering inflammation in both astrocytic-microglial co-cultures and CB2 receptor knockout models (Kong et al., 2014; Y. Li & Kim, 2016).

Our findings corroborate AbnCBD's neuroprotective profile within OHSCs. Cultures treated with AbnCBD showed stable microglial densities, lower PI-positive cell densities during the critical 48-hour period, and stable IL-6 concentrations over 29 days (Figure 14). These results suggest that AbnCBD neither induces neurotoxicity nor triggers inflammation, effectively maintaining neuronal homeostasis. Furthermore, sham Fe-transport controls treated with AbnCBD showed no significant differences in microglial density, IL-6 concentrations, or cell viability compared to untreated controls. This highlights AbnCBD's non-immunogenic nature and utility in inflammation-related studies, where minimizing confounding immune responses is critical (Kozela et al., 2011).

Cannabinoid treatments (AbnCBD and GP1a) did not induce inflammation or neurotoxicity in sham-irradiated transport controls, further supporting their safety profiles. However, the contrasting microglial dynamics observed under different transport scenarios underscore the importance of minimizing stress during tissue handling to ensure reliable assessment of pharmacological interventions. These results reinforce the utility of AbnCBD and GP1a in inflammation-related studies, while emphasizing the need for stringent control of experimental conditions.

4.5 Low-Dose X-Rays: Neurobiological Effects in Radiobiological and Space Research

Low-dose X-ray radiation provides a critical reference in space radiation research, offering baseline neurobiological insights. While high doses are common in clinical settings, low-dose exposure can disrupt neurogenesis and trigger neuroinflammation, particularly in the hippocampus. The DG, with its ongoing neurogenesis, shows particular vulnerability, exhibiting radiation-induced impairments in neuronal development (Fiorica et al., 2022; Y. Liu et al., 2023). Chronic neuroinflammation through glial activation compounds this damage (Boyd et al., 2021c; Schmal et al., 2021). These established dose-response relationships make low-dose X-rays valuable for comparison with heavy ions, enabling predictive models for neurocognitive risks and informing radioprotective strategies (Acharya et al., 2015; Turnquist et al., 2020).

4.5.1 Immediate effects: 0.5 hours post X-ray irradiation

X-ray exposure (0.3 Gy) induced immediate changes in the dentate gyrus of OHSCs despite stable overall cell counts (~ 400 cells) Figure 15. Microglial density decreased significantly by ~35 % (from 350 to 230 cells/mm^2, Figure 14D) compared to sham controls, while cell death modestly increased as evidenced by propidium iodide staining (approximately +50 fold change) (Figure 16F). This suggests activation of radiation-induced cell death pathways mediated by DNA damage and p53 activation (Fei & El-Deiry, 2003).

IL-6 levels remained stable at ~12 pg/ml, contrasting with *in vivo* studies that typically report immediate pro-inflammatory cytokine surges (W. H. Lee et al., 2010) . This discrepancy likely reflects either the isolated nature of the OHSC model, which lacks systemic inflammatory influences, or rapid activation of the ATM kinase pathway that may transiently suppress pro-inflammatory responses through modulation of NF-κB signaling (Hinz et al., 2010; Song et al., 2019).

Microglial morphology shifted markedly, with amoeboid microglia doubling compared to controls, indicating early activation (Figure 17). Concurrently, ramified microglia declined sharply to one-third of baseline levels. This pattern differs from typical *in vivo* responses, where both microglial types often increase after irradiation (Acharya et al., 2016). The amoeboid microglia likely migrated to radiation-damaged sites to facilitate tissue recovery, while the pronounced reduction

in ramified microglia suggests an enhanced localized response in the OHSC model, possibly due to the absence of blood-brain barrier constraints (Ronaldson & Davis, 2020).

The combination of stable IL-6 levels with increased amoeboid and decreased ramified microglia highlights the dentate gyrus's unique immune environment, potentially reflecting its immune-privileged status designed to protect the neural stem cell niche (Louveau et al., 2015; Prinz et al., 2021b). These early dynamics likely represent a "post-stress state" that balances neuroprotection and inflammation.

4.5.1.1 Conclusion, immediately Post X-ray irradiation

The immediate effects of 0.3 Gy X-ray exposure demonstrate a complex response involving microglial depletion (Mizumatsu et al., 2003; Morganti et al., 2012), increased cell death (Fike et al., 2007), and atypical inflammatory modulation (Han et al., 2016). ATM-p53 signaling likely coordinates these processes (Herzog et al., 1998; Marples & Collis, 2008), regulating DNA repair, apoptosis, and cytokine production (Narayanan et al., 2017). The involvement of p53 is further supported by the observed pattern of selective cell death combined with the preservation of overall tissue integrity, a hallmark of p53-mediated apoptotic responses to radiation-induced DNA damage (Fei & El-Deiry, 2003). While microglia show early activation, their capacity to resolve inflammation appears compromised. These findings emphasize the intricate relationship between cellular survival and inflammation in the dentate gyrus and highlight the importance of anatomical context when interpreting neural responses to radiation.

4.5.2 SHORT-TERM EFFECTS: 12- 48 HOURS POST X-RAY IRRADIATION

We investigated the short-term effects (12 and 48 hours) of 0.3 Gy X-ray irradiation on OHSCs, focusing on microglial activity, cell death, inflammatory cytokine profiles, and gene expression dynamics. These time points extend beyond the immediate post-irradiation phase (0.5 hours) previously analyzed and provide insights into delayed neuroinflammatory processes.

At 12 hours post-irradiation, overall cell counts in the dentate gyrus remained unchanged compared to controls, while microglial density decreased modestly to 280 cells/mm^2. Microglial morphology also changed; while over 50 % of microglia were amoeboid in both groups at 12 hours, irradiated OHSCs exhibited only 60 % amoeboid microglia by 48 hours compared to 80 % in sham controls. This suggests slower microglial activation in irradiated samples, reflecting a more sustained neuroinflammatory response.

These results align with *in vivo* studies showing that brain irradiation induces rapid microglial activation, followed by partial resolution Acharya et al., 2015; Boyd et al., 2021b). Irradiated OHSCs exhibited delayed yet persistent microglial activation, with reactive microglia persisting and ramified microglia absent at 48 hours (Figure 17).

IL-6 levels demonstrated a distinct temporal increase in irradiated OHSCs. While IL-6 concentration rose from 12 pg/ml at 0.5 hours to 17 pg/ml at 12 hours and reached 19 pg/ml at 48 hours, this rise was significantly attenuated compared to sham-irradiated cultures (Figure 18A). These findings suggest that low-dose irradiation induces a modulated inflammatory response in isolated hippocampal tissue, likely due to the absence of systemic inflammatory mediators.

The delayed increase in IL-6 levels parallels prior research, which identified biphasic inflammatory responses in neural tissues subjected to low-dose radiation, attributed to dose-dependent activation of NF-κB signaling pathways (Taniguchi & Karin, 2018). Additionally, studies on *ex vivo* brain models reported threshold effects in IL-6 expression (Gan et al., 2023; Montay-Gruel et al., 2019).

Contrary to the initial reduction in dead cells observed earlier, PI+ cell density increased to 60 cells/mm^2 at 12 hours and peaked at 120 cells/mm^2 by 48 hours (Figure 16). This delayed trajectory of cell death is consistent with apoptosis-driven neurotoxicity reported in irradiated

hippocampal cultures (Turnquist et al., 2020). The data suggest that while low-dose irradiation may initially trigger protective cellular responses, sustained exposure leads to cumulative cellular stress and apoptosis.

RNA sequencing at 12 hours post-irradiation revealed significant changes in gene expression. Downregulated genes included OTX2, MUC2, LOX, IGF2, STRA6, and RET, many involved in neurogenesis, neurodevelopment, and extracellular matrix remodeling (Figure 20). For example, OTX2 plays a crucial role in regulating hippocampal development, and its suppression may signal impaired neuroprotective mechanisms. Similarly, IGF2, a promoter of neurogenesis and synaptic plasticity, showed reduced expression (Fitzgerald et al., 2023).

Conversely, upregulated genes included VEGFD, MSR1, HTR7, IFI203, NMBR, and MMP3, all associated with inflammation, angiogenesis, and tissue remodeling (Table 6). Notably, VEGFD and MMP3 are critical mediators of vascular remodeling and extracellular matrix degradation, processes integral to post-injury tissue repair but also implicated in blood-brain barrier disruption (Kim & Hwang, 2011).

Irradiation did not alter the expression of genes encoding cannabinoid receptors CB1, CB2, and GPR55, which modulate neuroinflammation (Haspula & Clark, 2020). This contrasts with in vivo studies where higher radiation doses significantly upregulated cannabinoid receptor expression Lee et al., 2017).

4.5.2.1 Conclusion, short-term post X-ray irradiation

Exposure to 0.3 Gy X-ray induces a delayed, dynamic response in OHSCs. Microglial activation and IL-6 levels increase slowly but remain attenuated relative to sham controls (Figure 18, Figure 19). Gene expression shifts toward tissue remodeling and cellular stress pathways, with downregulation of neurogenic regulators and upregulation of inflammatory mediators. The absence of systemic inflammatory influences in OHSCs likely shapes these unique dynamics, characterized by prolonged neuroinflammation and adaptation toward tissue repair.

4.5.3 LONG-TERM EFFECTS: 7- 29 DAYS POST X-RAY IRRADIATION

We investigated the long-term impact of 0.3 Gy X-ray irradiation on OHSCs at 7 and 29 days post-irradiation. Our findings highlight key differences in microglial dynamics, cytokine expression, and cell viability relative to sham-irradiated controls.

Cell viability remained stable throughout the observation period, with total cell counts comparable to those in sham-irradiated controls. Furthermore, the density of PI+ cells was similar to or even lower than in sham-irradiated OHSCs, indicating minimal radiation-induced cytotoxicity at these time points (Figure 16). These results are consistent with studies by Antonelli et al., 2021, who reported that low-dose irradiation may activate protective pathways such as Sonic Hedgehog (Shh) signaling, promoting neurogenesis and cellular repair. The Shh pathway, known to mitigate pro-inflammatory responses, likely played a role in maintaining tissue integrity in our irradiated OHSC model.

Interestingly, while an increase in microglial activation was noted at 7 days, microglial density normalized by 29 days, and IL-6 concentrations were significantly lower than in sham-irradiated controls at both time points (Figure 18B). This transient nature of microglial activation contrasts with *in vivo* findings by Constanzo et al., 2020, where neuroinflammation persisted, contributing to long-term cognitive deficits. The discrepancy may stem from systemic influences in whole-animal models, absent in the isolated OHSC system. Without systemic inflammatory inputs, OHSCs may resolve inflammation more efficiently, allowing a faster return to homeostasis.

Our results parallel findings by Ung et al., (2021), who observed dose-dependent long-term effects of radiation on glial cell function. While higher doses led to sustained neuroinflammation and behavioral changes, our data suggest that at 0.3 Gy, hippocampal tissue demonstrates resilience, with microglial density and morphology returning to baseline by 29 days (Figure 16). This recovery pattern underscores a threshold-dependent effect, wherein low doses may elicit transient inflammation that resolves over time.

A novel aspect of our study is the observed reduction in IL-6 levels at long-term time points, in contrast to both Costanzo's and Ung's findings, where IL-6 remained elevated in irradiated brain tissue. This suggests that the OHSC model might uniquely capture the resolution phase of

neuroinflammation, offering a more nuanced view of tissue recovery in the absence of systemic immune interactions.

We further evaluated the role of cannabinoid receptor ligands, AbnCBD and GP1a, in modulating microglial responses to 0.3 Gy X-ray irradiation in OHSCs. GP1a, a CB2 receptor antagonist, did not significantly alter total cell counts or microglial density over the long term (Figure 23). However, an increase in PI+ cells was observed at later time points, indicating delayed apoptotic activity (

Figure 24). Notably, GP1a treatment at 48 hours resulted in reduced amoeboid microglia and increased reactive and ramified microglia, suggesting a shift towards tissue repair and anti-inflammatory states. Despite these morphological changes, elevated IL-6 levels persisted in the long-term phase, indicating a delay in inflammation resolution (Figure 26). These findings align with previous research on CB2 antagonism, where blocking CB2 was associated with prolonged inflammatory responses (Soethoudt et al., 2017; Turcotte et al., 2016).

In contrast, AbnCBD, a potential GPR55 agonist, produced more consistent effects. Total cell counts remained stable, and microglial density decreased significantly between 48 hours and 7 days post-irradiation (Figure 29). AbnCBD treatment resulted in fewer amoeboid microglia and a balanced distribution of reactive and ramified microglia, indicating effective modulation of the inflammatory response without exacerbating neuroinflammation. IL-6 levels remained low, supporting AbnCBD's anti-inflammatory role (Figure 32). These observations are consistent with studies demonstrating that GPR55 activation can promote neuroprotection by reducing microglial activation and limiting inflammatory signaling (Celorrio et al., 2017).

4.5.3.1 Conclusion, long-term post X-ray irradiation

Our long-term study of low-dose X-ray irradiation on OHSCs reveals transient microglial activation, minimal cell death, and reduced IL-6 expression over time, suggesting a resilient response to low-dose radiation. The differential effects of GP1a and AbnCBD on microglial morphology and cytokine levels provide insights into the distinct roles of CB2 and GPR55 receptors in neuroinflammatory regulation. GP1a's delayed apoptotic activity and persistent IL-6 elevation contrast with AbnCBD's stabilizing effects, highlighting the therapeutic potential of targeting GPR55 for modulating radiation-induced neuroinflammation. These findings underscore the importance of dose, timing, and model-specific factors in interpreting radiation responses.

4.6 Low-Dose ^{56}Fe-ions: Neurobiological Effects in Radiobiological and Space Research

^{56}Fe-ion radiation is a key component of space radiation, particularly concerning long-term missions beyond earth's protective magnetic field, such as Mars expeditions. Unlike X-rays, ^{56}Fe-ions exhibit high LET, producing dense ionization tracks that cause complex DNA damage, oxidative stress, and persistent neuroinflammatory responses. These unique properties make ^{56}Fe-ion radiation crucial for understanding space environment effects on biological systems.
In neuronal tissues, ^{56}Fe-ion exposure has been linked to hippocampal dysfunction, which is vital for memory and learning (Impey et al., 2016; Ung, 2020). Evidence indicates that ^{56}Fe-ions can impair synaptic plasticity, inhibit neurogenesis, and sustain chronic neuroinflammation through microglial and astrocytic activation (Rola et al., 2008a; Schmal & Rübe, 2022). This is particularly relevant for space missions, where astronauts are continuously exposed to galactic cosmic rays, in which ^{56}Fe-ions are a significant component.

Due to the limited feasibility of shielding against high-LET radiation in space, understanding the biological effects of ^{56}Fe-ions is essential for designing countermeasures, including neuroprotective strategies, to reduce the cognitive risks associated with prolonged space travel.

4.6.1 Immediate Effects: 0.5 hours post ^{56}Fe-ion irradiation

Our data demonstrated that despite comparable total cell counts between ^{56}Fe-irradiated OHSCs and sham controls, ^{56}Fe-irradiated samples showed higher PI+cell density than X-ray-exposed cultures. This paradoxical finding—preservation of total cell population alongside increased localized cell death—points to a biphasic response involving both damage induction and protective mechanisms (Cucinotta & Cacao, 2017; Held et al., 2016)

We propose that ^{56}Fe-ion irradiation causes clustered DNA damage and mitochondrial dysfunction, triggering the release of mitochondrial DNA (mtDNA) fragments that act as DAMPs. Our observation of significantly higher microglial density in the DG of ^{56}Fe-irradiated OHSCs compared to X-ray-irradiated samples supports this damage-sensing response. The 20 % increase in reactive microglia in ^{56}Fe-irradiated cultures (versus sham controls) and the concomitant reduction of ramified microglia to approximately one-quarter of sham levels (Figure 36) directly reflect this activation process. These activated microglia likely respond to DAMPs through dual signaling cascades: the cytosolic DNA sensor cyclic GMP-AMP synthase (cGAS)-STING pathway

and the endosomal Toll-like receptor 9 (TLR9) pathway (De Los Santos, 2021; Shimura et al., 2016).

The mechanistic link between microglial activation and cytokine production is evidenced by our IL-6 measurements. We detected significantly elevated IL-6 levels at 0.5 hours post-irradiation in ^{56}Fe-irradiated OHSCs compared to pre-irradiation levels. Critically, while X-ray exposure produced dose-dependent IL-6 increases, ^{56}Fe-ions showed a non-linear response where IL-6 levels at 3.0 Gy decreased toward sham levels rather than continuing to rise. This unexpected threshold effect supports our hypothesis that protective autophagy mechanisms are activated at higher ^{56}Fe-ion doses (Gan et al., 2023; Lumniczky et al., 2017).

We propose that selective mitophagy is rapidly upregulated to clear damaged mitochondria and limit DAMP release. This process could help limit the extent of inflammation by reducing the availability of DAMPs (Gómez-Virgilio et al., 2022). The heterogeneous energy deposition characteristic of ^{56}Fe-ions creates distinct microenvironments within the tissue where autophagy induction varies in intensity, explaining our experimental observation of localized cell death alongside overall tissue preservation (Autsavapromporn et al., 2011; Kamada et al., 2015). The rapid activation of this process (within 0.5 hours) suggests pre-primed autophagy machinery in neural tissue specifically responsive to high-LET radiation insults.

This interpretation aligns with recent advances in radiation biophysics literature. The role of autophagy in modulating radiation-induced neuroinflammation is supported by studies showing that autophagy can regulate both inflammation and cell survival under stress conditions (Kempuraj & Mohan, 2022). Similarly, research has established that TLR9 stimulation by mtDNA triggers neuroinflammatory responses comparable to our measured IL-6 elevation (Girdhani et al., 2013; Helm & Fournier, 2023).

Comparing our results to peer publications reveals both confirmatory and novel aspects. Our observed paradoxical maintenance of total cell counts despite increased PI-positive cells aligns with models of spatially heterogeneous damage from high-LET radiation (Alloni et al., 2012). However, our finding of decreased IL-6 at higher ^{56}Fe-ion doses differs from strictly dose-dependent responses, suggesting unique space radiation effects not captured in traditional paradigms (Mathur et al., 2017).

4.6.1.1 Conclusion, immediately Post ^{56}Fe-ion irradiation

These findings have significant implications for space radiation protection. Our observed early activation of autophagy (as inferred from the IL-6 threshold effect and cell survival patterns) suggests a potential therapeutic window for pharmacological intervention. The rapid induction of autophagy within 0.5 hours post-irradiation, as suggested by our observed changes in cellular and cytokine responses, may set the stage for long-term neuroprotective effects (Averbeck & Rodriguez-Lafrasse, 2021).

To validate this mechanism, future studies should quantify autophagy markers such as LC3-II and p62 in ^{56}Fe-irradiated OHSCs, assess mtDNA release, and employ autophagy modulators to establish causality between autophagy and the observed IL-6 dynamics we've documented (Roy et al., 2022).

4.6.2 SHORT-TERM EFFECTS: 12- 48 HOURS POST ^{56}FE-ION IRRADIATION

Investigation into the effects of ^{56}Fe-ion radiation on OHSCs reveals a complex neuroimmune response that diverges significantly from conventional radiation paradigms. The distinct patterns of microglial activation, cell survival, and inflammatory signaling following heavy ion exposure provide critical insights into the unique challenges of space radiation and potential neuroprotective strategies.

The remarkable preservation of total cell numbers in ^{56}Fe-irradiated OHSCs, contrasting with the transient decline observed after X-ray exposure, suggests the activation of adaptive mechanisms specific to high-LET radiation. This resilience may reflect the engagement of distinct DNA repair pathways and stress responses that are preferentially activated by clustered DNA damage characteristic of heavy ion tracks (Cucinotta & Durante, 2006). The biphasic microglial response—initial reduction followed by substantial proliferation—indicates a coordinated neuroimmune reaction that likely contributes to this cellular preservation. This observation corroborates prior studies by Wang et al. (2022), which highlighted a prolonged pro-inflammatory microglial phenotype following heavy ion exposure compared to low-LET radiation.

Perhaps most striking is the heterogeneous microglial activation pattern observed 48 hours post-^{56}Fe irradiation. The simultaneous presence of amoeboid, reactive, and ramified microglia suggests that the CNS maintains functional diversity within its immune compartment even under severe radiation stress (Figure 17, Figure 36). This phenotypic heterogeneity may represent an evolutionary adaptation that allows the brain to simultaneously engage in debris clearance, inflammatory signaling, and homeostatic surveillance. Such functional compartmentalization contrasts with the more uniform microglial activation following X-ray exposure and aligns with recent reconceptualizations of microglia as highly specialized cells capable of context-dependent responses (Prinz et al., 2021b). This heterogeneous response aligns with findings by Gupta et al.,(2017) and Chen et al., (2023), who reported that heavy ion radiation elicits more complex microglial activation patterns than low-LET radiation.

The persistence of ramified microglia amidst a predominantly activated population supports the concept proposed by Vidal-Itriago et al., (2022) that microglia exhibit a spectrum of activation states, allowing for fine-tuned responses to environmental stressors. The non-linear dose-response observed in IL-6 production challenges the linear no-threshold model often applied in

radiation protection. The variability at lower doses suggests threshold effects or complex signaling networks that buffer inflammatory responses until reaching a critical activation level. The elevated IL-6 concentration, particularly at higher doses, aligns with findings by Acharya et al., (2015), who reported distinct cytokine upregulation following heavy ion exposure. This has significant implications for establishing radiation exposure limits for astronauts, particularly during long-duration missions where cumulative low-dose exposure predominates.

Our pharmacological interventions yield particularly nuanced insights regarding microglial modulation as a countermeasure strategy. The differential effects of GP1a and AbnCBD—both reducing cell death despite contrasting effects on microglial morphology and density—suggest that the functional consequences of microglial activation states are more complex than previously appreciated. The CB2 receptor agonist GP1a appears to enhance microglial phagocytic capacity without exacerbating inflammatory damage, while AbnCBD promotes microglial heterogeneity with enhanced homeostatic surveillance capacity. These findings challenge the traditional view of microglial activation as uniformly detrimental following radiation exposure.

The coincidence of increased microglial density and elevated IL-6 with reduced cell death in AbnCBD-treated cultures is particularly noteworthy. This apparent paradox suggests that controlled neuroinflammation may facilitate tissue recovery when appropriately regulated. Rather than pursuing blanket anti-inflammatory strategies, our results indicate that maintaining microglial functional diversity while promoting specific activation states may offer superior neuroprotection against heavy ion radiation effects.

These findings have broader implications for understanding CNS radiation responses beyond space travel. The unique microglial activation patterns observed following ^{56}Fe irradiation may inform therapeutic approaches for conditions characterized by chronic neuroinflammation, including neurodegenerative diseases and cancer radiotherapy complications. These findings contrast previous research by (Parihar et al., 2016), which linked space radiation exposure to long-term cognitive impairments, by suggesting that differential microglial activation may contribute to persistent neuroinflammatory states that could be therapeutically targeted. The cannabinoid signaling system, given its differential effects on microglial phenotype and function, represents a promising target for modulating neuroimmune responses in these contexts.

4.6.2.1 Conclusion, short-term post ^{56}Fe-ion irradiation

The distinctive neuroimmune response to high-LET ^{56}Fe radiation, characterized by microglial heterogeneity and complex inflammatory dynamics, challenges conventional radiobiological paradigms. The findings demonstrate that heavy ion exposure induces a unique pattern of microglial activation that differs fundamentally from X-ray effects. Cannabinoid receptor modulation differentially altered these responses, with both CB2 and atypical cannabinoid receptor agonists reducing cell death despite divergent effects on microglial morphology and cytokine production. This suggests that controlled neuroinflammation with preserved microglial functional diversity may promote CNS adaptation to radiation stress. Collectively, our results highlight the need to reconsider fundamental radiobiological concepts when addressing space radiation risks, emphasizing cell-type specific responses, adaptive tissue-level coordination, and the potential for targeted neuroimmune modulation as a countermeasure strategy.

4.6.3 LONG-TERM EFFECTS: 7– 29 DAYS POST ^{56}FE-ION IRRADIATION

The long-term effects of 0.3 Gy ^{56}Fe-ion irradiation on OHSCs revealed distinct patterns in microglial activation, morphology, and inflammatory regulation compared to X-ray irradiation. Despite similar total cell counts across ^{56}Fe-ion irradiated, sham, and X-ray irradiated OHSCs at 7- and 29-days post-irradiation, microglial density remained persistently elevated in ^{56}Fe-ion irradiated samples (Figure 35). This prolonged microglial activation suggests a sustained neuroinflammatory response, consistent with prior studies on high-LET radiation exposure (Betlazar et al., 2016; Voshart et al., 2024).

At 7 days post-irradiation, the morphological analysis revealed that ^{56}Fe-ion irradiated OHSCs exhibited a higher proportion of ramified microglia compared to X-ray irradiated samples, where amoeboid microglia dominated (Figure 36). This indicates a more regulated immune response to ^{56}Fe-ions, with microglia transitioning to a reactive but less inflammatory phenotype. These findings align with Sorokina et al. (2021), who reported prolonged microglial activation with fewer amoeboid pro-inflammatory phenotypes following heavy ion radiation (Sorokina et al., 2021).

By 29 days, the proportion of ramified microglia across radiation types became comparable, yet ^{56}Fe-irradiated OHSCs maintained elevated reactive microglial levels, while X-ray irradiated cultures exhibited a higher proportion of amoeboid microglia (Figure 36). This divergence highlights a slower resolution of inflammation following ^{56}Fe-ion exposure, potentially reflecting differences in energy deposition and tissue damage repair mechanisms. Rienecker et al. (2021) similarly described persistent, multifaceted microglial responses after high-LET radiation, supporting the notion that heavy ion exposure induces a prolonged yet regulated inflammatory state (Rienecker et al., 2021).

Interestingly, long-term IL-6 concentrations in ^{56}Fe-ion irradiated OHSCs showed no significant changes compared to sham controls in the dentate gyrus, contrasting with *in vivo* studies where chronic IL-6 elevation is typically observed (Cacao & Cucinotta, 2016). Other studies using a human tumor cell line have reported elevated IL-6 levels exclusively 4- 24 hours after a single dose IR (Di Maggio et al., 2015). This discrepancy may result from th isolated nature of the OHSC model, which lacks systemic inflammatory influences present in whole-organism models. Additionally, the persistent shift in microglial morphology towards a neuroprotective phenotype observed in

^{56}Fe-irradiated samples could explain the stable IL-6 levels. Notably, the DG region of the hippocampus is known to be under particular surveillance and protection by microglial cells, given its crucial role in neurogenesis and synaptic plasticity (Sierra et al., 2010). Microglia in this region actively regulate neuronal development, prune synapses, and respond to environmental stressors to maintain homeostasis (Gemma & Bachstetter, 2013). The sustained presence of neuroprotective microglial phenotypes in the DG following heavy-ion irradiation may therefore contribute to a controlled inflammatory response, preventing excessive cytokine release while still supporting tissue repair and neural integrity (Kreutzberg, 1996).Our findings suggest that in the absence of systemic feedback, microglial responses in ^{56}Fe-ion irradiated OHSCs can achieve localized immune regulation, potentially mitigating chronic inflammation.

The anti-inflammatory potential of the CB2 receptor antagonist GP1a was assessed by administering 10 µM GP1a every three days over the 29-day culture period. Despite no significant differences in total cell count (Figure 40) or microglial density (Figure 41) between treated and untreated ^{56}Fe-irradiated OHSCs, a key finding emerged at 29 days: GP1a-treated samples exhibited a marked reduction in PI-positive dead cells compared to untreated samples (Figure 41). This suggests a protective effect of GP1a against long-term radiation-induced cell death, a phenomenon not observed in X-ray irradiated OHSCs.

At 29 days, both treated and untreated ^{56}Fe-irradiated OHSCs exhibited fewer than 40 % amoeboid microglia and comparable levels of reactive and ramified microglia. In contrast, X-ray irradiated OHSCs retained a higher proportion of amoeboid microglia (~40 –60 %), suggesting that GP1a facilitates a more effective resolution of neuroinflammation following ^{56}Fe-ion exposure. Reduced IL-6 levels in GP1a-treated samples further support this hypothesis (Figure 43). These findings imply that CB2 receptor activation by GP1a primes microglia to adopt a neuroprotective, tissue-repairing state rather than merely suppressing inflammation, as proposed by Vuic et al. (2022) (Vuic et al., 2022).

The GPR55 agonist AbnCBD was also evaluated for its anti-inflammatory potential by administering 10 µM AbnCBD regularly over 29 days following 0.3 Gy ^{56}Fe-ion irradiation. AbnCBD-treated OHSCs showed stable total cell counts (Figure 44) and comparable microglial density (Figure 45) to untreated samples but displayed distinct patterns in IL-6 concentration.

At long-term time points, IL-6 levels in AbnCBD-treated OHSCs were comparable to untreated samples but higher than in X-ray irradiated cultures, suggesting a unique inflammatory regulation

mediated by GPR55 (Figure 32, Figure 47). This pattern supports the concept of "homeostatic recalibration," where GPR55 activation does not entirely suppress inflammation but instead promotes a balanced, adaptive immune state (Martínez-Pinilla et al., 2019). Studies involving GPR55 antagonists have shown that modulating this receptor can significantly influence cytokine production and glial function, highlighting its potential role in glial-neuronal crosstalk and neuroprotection (Saliba et al., 2021; Sun et al., 2024).

IL-6 levels to AbnCBD treatment indicates that moderate GPR55 activation may induce adaptive immune responses, while either excessive activation or complete antagonism could yield different inflammatory outcomes (Apweiler et al., 2024). These findings underscore the complexity of GPR55-mediated signaling in neuroinflammatory regulation and suggest that precise modulation of this receptor could offer therapeutic benefits in radiation-induced neuropathologies.

4.6.3.1 Conclusion, long-term post ^{56}Fe-ion irradiation

Long-term measurements after the exposure to 0.3 Gy ^{56}Fe-ion radiation elicits a sustained yet regulated neuroinflammatory response, characterized by persistent microglial activation, morphological diversity, and stable IL-6 levels. The distinct responses to cannabinoid receptor ligands GP1a and AbnCBD highlight their differential roles in modulating microglial behavior and inflammatory regulation. GP1a promoted resolution of neuroinflammation and reduced radiation-induced cell death, while AbnCBD facilitated a homeostatic recalibration of the inflammatory environment through GPR55 activation. These findings offer valuable insights into the mechanisms of neuroinflammatory regulation following heavy ion radiation and suggest potential avenues for developing targeted neuroprotective therapies for space radiation exposure.

4.7 SUMMARY OF KEY FINDINGS

This study investigated the effects of low-dose X-ray and ^{56}Fe-ion radiation on organotypic hippocampal slice cultures, focusing on neuroinflammation and the modulatory role of cannabinoid receptor ligands. X-ray irradiation induced characteristic inflammatory responses in OHSCs, while ^{56}Fe-ion irradiation triggered more pronounced neuroinflammation with slower resolution. The cannabinoid receptor ligands GP1a (CB2 agonist) and AbnCBD (GPR55 agonist) demonstrated anti-inflammatory effects in ^{56}Fe-ion irradiated OHSCs. GP1a significantly reduced long-term IL-6 levels and microglial activation, whereas AbnCBD modulated GPR55-mediated microglial activation and phenotype transitions.

4.7.1 IMPLICATIONS FOR NEUROINFLAMMATION RESEARCH

These findings highlight that radiation-induced neuroinflammation varies based on radiation type, and cannabinoid receptor ligands show promise in mitigating these effects. Specifically, the ATM-p53 signaling pathway appears to orchestrate the acute radiation response, regulating DNA repair mechanisms, apoptotic pathways, and inflammatory mediaton (Herzog et al., 1998; Marples & Collis, 2008). The neuroinflammatory response differs significantly between radiation qualities, with heavy ions inducing more persistent microglial activation and elevated pro-inflammatory cytokine levels compared to X-rays (Impey et al., 2016; Kiffer et al., 2018). The effectiveness of CB2 antagonist GP1a and GPR55 agonist AbnCBD in reducing microglial activation and IL-6 production, particularly following heavy ion exposure, suggests that targeted receptor modulation could provide effective countermeasures against radiation-induced neuroinflammation. These therapeutic approaches could potentially reduce long-term cognitive deficits resulting from space radiation or radiotherapy (Raber et al., 2019).

4.7.2 NOVEL CONTRIBUTIONS

The study makes several novel contributions, including a comparative analysis of low-dose X-ray and ^{56}Fe-ion radiation effects on hippocampal slice cultures, a detailed examination of morphological microglial responses over time, and an investigation of GP1a and AbnCBD's roles in modulating radiation effects through CB2 and GPR55 receptors, with a semi-automated quantification method.

4.7.3 FUTURE DIRECTIONS

Future research directions should focus on elucidating the molecular mechanisms of GP1a and AbnCBD's neuroprotective effects, investigating their long-term impacts on cognitive function *in vivo*, exploring the effects of higher radiation doses and chronic versus acute exposure, and studying the interplay between different cannabinoid receptors for developing targeted neuroprotective strategies. This work paves the way for advancing our understanding of radiation-induced neuroinflammation and the potential of cannabinoid receptor ligands as therapeutic agents in contexts where radiation exposure is a concern.

5 LIST OF TABLES

6 LIST OF FIGURES

7 LIST OF ABBREVIATIONS

Abbreviation	Meaning
Δ9-THC	Tetrahydrocannabinol
2-AG	2-arachidonoylglycerol
AEA	N-arachidonoylethanolamide
AbnCBD	Abnormal cannabidiol
AC	Adenylyl cyclase
ATM	Ataxia-telangiectasia mutated kinase
BBB	Blood-brain barrier
BBI	Bowman-Birk inhibitor
BNL	Brookhaven National Laboratory
C	Carbon
Ca	Calcium
CA	Cornu ammonis
CBXR	Cannabinoid receptor
CBD	Cannabidiol
cAMP	Cyclic adenosine monophosphate
cDNA	Complementary DNA
CNS	Central nervous system
DAMP	Damage-associated molecular pattern
DAPI	4′,6-Diamidin-2-phenylindol
DEG	Differentially expressed gene
DG	Dentate gyrus
DIV	Days in vitro
DNA	Desoxyribonucleic acid
DNA-PKcs	DNA-dependent protein kinase catalytic subunit
EC	Entorhinal cortex
ECS	Endocannabinoid system
Ethyol	Aminothiol amifostine
EtOH	Ethanol
Fe	Iron
GFAP	Glial fibrillary acidic protein
GCL	Granular cell layer
GDP	Guanosine diphosphate
GO	Gene ontology
GP1a	N-(piperidin-1-yl)-1-(2,4-dichlorophenyl)-1,4-dihydro-6-methylindeno (1,2-c) pyrazole-3-carboxamide
GPR55	G-protein-coupled receptor 55
GSI/FAIR	Facility for Antiproton and Ion Research in Europe GmbH
GTP	Guanosine triphosphate
GCR	Galactic cosmic radiation
H	Hydrogen
He	Helium
HF	Hippocampal formation
HRP	Horseradish peroxidase

HSP	Heat shock protein
HZE	High atomic number and energy particles
IBA1	Ionized calcium-binding adapter molecule 1
IB4	*Griffonia Simplicifolia Lectin I* (GSL I) isolectin B4
ICRP	International Commission on Radiological Protection
IL	Interleukin
IR	Ionizing radiation
ISS	International Space Station
LET	Linear energy transfer
LEO	Low Earth orbit
MAPK	Mitogen-activated protein kinase
MEZ	Medical experimental center
Mmu	*Mus musculus*
ML	Molecular layer
NAC	N-acetyl cysteine
NC	Nearest centroid
Ne	Neon
NeuN	Neuronal nuclear antigen
NGS	Normal goat serum
NSPC	Neural stem and progenitor cell
NSRL	NASA Space Radiation Laboratory
NRF2	Nuclear factor erythroid 2-related factor 2
NSC	Neuronal stem cell
O	Oxygen
OD	Optical density
OHSC	Organotypic entorhinal hippocampal slice culture
PBST	Phosphate-buffered saline with Tween
PE	Polyethylene
PI	Propidium iodide
PFA	Paraformaldehyde
PL	Polymorphic cell layer
PP	Perforant pathway
PPAR	Peroxisome proliferator-activated receptor
PRR	Pattern recognition receptor
RBE	Relative biological effectiveness
RFU	Relative fluorescent unit
RGLC	Radial glia-like cell
RhoA	Ras homolog gene family member A
ROCK	Rho-associated protein kinase
ROS	Reactive oxygen species
scRNA-seq	Single-cell RNA sequencing
SeM	L-Selenomethionine
SEP	Solar energetic particles
SGZ	Subgranular zone
Shh	Sonic hedgehog
Si	Silicon
SPE	Solar particle event
Sting	Stimulator of interferon genes

Sub	Subiculum
Sv	Sievert
SVZ	Subventricular zone
TLR	Toll-like receptor

8 REFERENCES

Abdolhoseini, M., Kluge, M. G., Walker, F. R., & Johnson, S. J. (2019). segmentation, tracing, and Quantification of Microglial Cells from 3D Image Stacks. *Scientific Reports*. https://doi.org/10.1038/s41598-019-44917-6

Acharya, M. M., Baulch, J. E., Klein, P. M., Baddour, A. A. D., Apodaca, L. A., Kramár, E. A., Alikhani, L., Garcia, C., Angulo, M. C., Batra, R. S., Fallgren, C. M., Borak, T. B., Stark, C. E. L., Wood, M. A., Britten, R. A., Soltesz, I., & Limoli, C. L. (2019). New concerns for neurocognitive function during deep space exposures to chronic, low dose-rate, neutron radiation. *ENeuro*, *6*(4). https://doi.org/10.1523/ENEURO.0094-19.2019

Acharya, M. M., Green, K. N., Allen, B. D., Najafi, A. R., Syage, A., Minasyan, H., Le, M. T., Kawashita, T., Giedzinski, E., Parihar, V. K., West, B. L., Baulch, J. E., & Limoli, C. L. (2016). Elimination of microglia improves cognitive function following cranial irradiation. *Scientific Reports*, *6*. https://doi.org/10.1038/SREP31545

Acharya, M. M., Patel, N. H., Craver, B. M., Tran, K. K., Giedzinski, E., Tseng, B. P., Parihar, V. K., & Limoli, C. L. (2015). Consequences of Low Dose Ionizing Radiation Exposure on the Hippocampal Microenvironment. *PLoS ONE*, *10*(6). https://doi.org/10.1371/JOURNAL.PONE.0128316

Acsády, L., Kamondi, A., Sík, A., Freund, T., & Buzsáki, G. (1998). GABAergic cells are the major postsynaptic targets of mossy fibers in the rat hippocampus. *The Journal of Neuroscience : The Official Journal of the Society for Neuroscience*, *18*(9), 3386–3403. https://doi.org/10.1523/JNEUROSCI.18-09-03386.1998

Alloni, D., Campa, A., Friedland, W., Mariotti, L., & Ottolenghi, A. (2012). Track structure, radiation quality and initial radiobiological events: considerations based on the PARTRAC code experience. *International Journal of Radiation Biology*, *88*(1–2), 77–86. https://doi.org/10.3109/09553002.2011.627976

Altman, J., & Das, G. D. (1965). Autoradiographic and Histoloaical Evidence of Postnatal Hippocampal Neurogenesis in Rats ’. *Journal of Comparative Neurology*, *124*(3), 319–336.

Amaral, D. G. (1978). A golgi study of cell types in the hilar region of the hippocampus in the rat. *Journal of Comparative Neurology*, *182*(5), 851–914. https://doi.org/10.1002/CNE.901820508

Amaral, D. G., Scharfman, H. E., & Lavenex, P. (2007). The dentate gyrus: fundamental neuroanatomical organization (dentate gyrus for dummies). *Progress in Brain Research*, *163*, 3. https://doi.org/10.1016/S0079-6123(07)63001-5

Andersen, P., Morris, R., Amaral, D., Bliss, T., & O’Keefe, J. (2007). *The Hippocampus Book*. Oxford UNIVERSITY PRESS. https://books.google.de/books?hl=en&lr=&id=hSs_RETVWlIC&oi=fnd&pg=PR11&ots=A_-bvuIGPt&sig=a7dX0AE50H-WO04g-QxAkSIXEiY&redir_esc=y#v=onepage&q&f=false

Antonelli, F., Casciati, A., Belles, M., Serra, N., Linares Vidal, M. V., Marino, C., Mancuso, M., & Pazzaglia, S. (2021). Long-term effects of ionizing radiation on the hippocampus: Linking effects of the sonic hedgehog pathway activation with radiation response. *International Journal of Molecular Sciences*, *22*(22). https://doi.org/10.3390/IJMS222212605/S1

Apweiler, M., Saliba, S. W., Sun, L., Streyczek, J., Normann, C., Hellwig, S., Bräse, S., & Fiebich, B. L. (2024). Modulation of neuroinflammation and oxidative stress by targeting

GPR55 – new approaches in the treatment of psychiatric disorders. *Molecular Psychiatry 2024*, 1–10. https://doi.org/10.1038/s41380-024-02614-5

Askew, K., Li, K., Olmos-Alonso, A., Garcia-Moreno, F., Liang, Y., Richardson, P., Tipton, T., Chapman, M. A., Riecken, K., Beccari, S., Sierra, A., Molnár, Z., Cragg, M. S., Garaschuk, O., Perry, V. H., & Gomez-Nicola, D. (2017). Coupled Proliferation and Apoptosis Maintain the Rapid Turnover of Microglia in the Adult Brain. *Cell Reports*, *18*(2), 391–405. https://doi.org/10.1016/J.CELREP.2016.12.041

Ativie, F., Komorowska, J. A., Beins, E., Albayram, Ö., Zimmer, T., Zimmer, A., Tejera, D., Heneka, M., & Bilkei-Gorzo, A. (2018). Cannabinoid 1 Receptor Signaling on Hippocampal GABAergic Neurons Influences Microglial Activity. *Frontiers in Molecular Neuroscience*, *11*, 295. https://doi.org/10.3389/FNMOL.2018.00295/BIBTEX

Atwood, B. K., & MacKie, K. (2010). CB2: a cannabinoid receptor with an identity crisis. *British Journal of Pharmacology*, *160*(3), 467–479. https://doi.org/10.1111/J.1476-5381.2010.00729.X

Autsavapromporn, N., De Toledo, S. M., Little, J. B., Jay-Gerin, J. P., Harris, A. L., & Azzam, E. I. (2011). The role of gap junction communication and oxidative stress in the propagation of toxic effects among high-dose α-particle-irradiated human cells. *Radiation Research*, *175*(3), 347–357. https://doi.org/10.1667/RR2372.1

Averbeck, D., & Rodriguez-Lafrasse, C. (2021). Role of Mitochondria in Radiation Responses: Epigenetic, Metabolic, and Signaling Impacts. *International Journal of Molecular Sciences*, *22*(20), 22. https://doi.org/10.3390/IJMS222011047

Belcher, E. K., Sweet, T. B., Karaahmet, B., Dionisio-Santos, D. A., Owlett, L. D., Leffler, K. A., Janelsins, M. C., Williams, J. P., Olschowka, J. A., & O'Banion, M. K. (2020). Cranial irradiation acutely and persistently impairs injury-induced microglial proliferation. *Brain, Behavior, & Immunity - Health*, *4*. https://doi.org/10.1016/J.BBIH.2020.100057

Bennett, F. C., Bennett, M. L., Yaqoob, F., Mulinyawe, S. B., Grant, G. A., Hayden Gephart, M., Plowey, E. D., & Barres, B. A. (2018). A Combination of Ontogeny and CNS Environment Establishes Microglial Identity. *Neuron*, *98*(6), 1170-1183.e8. https://doi.org/10.1016/J.NEURON.2018.05.014

Betlazar, C., Middleton, R. J., Banati, R. B., & Liu, G. J. (2016). The impact of high and low dose ionising radiation on the central nervous system. *Redox Biology*, *9*, 144–156. https://doi.org/10.1016/J.REDOX.2016.08.002

Borst, K., Dumas, A. A., & Prinz, M. (2021). Microglia: Immune and non-immune functions. *Immunity*, *54*(10), 2194–2208. https://doi.org/10.1016/J.IMMUNI.2021.09.014

Bosier, B., Muccioli, G. G., Hermans, E., & Lambert, D. M. (2010). Functionally selective cannabinoid receptor signalling: therapeutic implications and opportunities. *Biochemical Pharmacology*, *80*(1), 1–12. https://doi.org/10.1016/J.BCP.2010.02.013

Boyd, A., Byrne, S., Middleton, R. J., Banati, R. B., & Liu, G. J. (2021a). Control of Neuroinflammation through Radiation-Induced Microglial Changes. *Cells 2021, Vol. 10, Page 2381*, *10*(9), 2381. https://doi.org/10.3390/CELLS10092381

Boyd, A., Byrne, S., Middleton, R. J., Banati, R. B., & Liu, G. J. (2021b). Control of Neuroinflammation through Radiation-Induced Microglial Changes. *Cells 2021, Vol. 10, Page 2381*, *10*(9), 2381. https://doi.org/10.3390/CELLS10092381

Britten, R. A., Davis, L. K., Jewell, J. S., Miller, V. D., Hadley, M. M., Sanford, L. D., Machida, M., & Lonart, G. (2014). Exposure to Mission Relevant Doses of 1 GeV/Nucleon 56 Fe Particles Leads to Impairment of Attentional Set-Shifting Performance in Socially Mature Rats. *RADIATION RESEARCH*, *182*, 292–298. https://doi.org/10.1667/RR3766.1

Cacao, E., & Cucinotta, F. A. (2016). Modeling Heavy-Ion Impairment of Hippocampal Neurogenesis after Acute and Fractionated Irradiation. *Radiation Research*, *186*(6), 624–637. https://doi.org/10.1667/RR14569.1

Carson, M. J., Doose, J. M., Melchior, B., Schmid, C. D., & Ploix, C. C. (2006). CNS immune privilege: hiding in plain sight. *Immunological Reviews*, *213*(1), 48–65. https://doi.org/10.1111/J.1600-065X.2006.00441.X

Celorrio, M., Rojo-Bustamante, E., Fernández-Suárez, D., Sáez, E., Estella-Hermoso de Mendoza, A., Müller, C. E., Ramírez, M. J., Oyarzábal, J., Franco, R., & Aymerich, M. S. (2017). GPR55: A therapeutic target for Parkinson's disease? *Neuropharmacology*, *125*, 319–332. https://doi.org/10.1016/j.neuropharm.2017.08.017

Chen, Z., Li, Y., Rasheed, M., Wang, H., Lei, R., Zhao, T., Deng, Y., & Ma, H. (2023). Altered expression of inflammation-associated molecules in striatum: an implication for sensitivity to heavy ion radiations. *Frontiers in Cellular Neuroscience*, *17*. https://doi.org/10.3389/FNCEL.2023.1252958

Chew, M. T., Nisbet, A., Jones, B., Suzuki, M., Matsufuji, N., Murakami, T., & Bradley, D. A. (2019). Ion beams for space radiation radiobiological effect studies. *Radiation Physics and Chemistry*, *165*. https://doi.org/10.1016/j.radphyschem.2019.108373

Clément, G. R., Boyle, R. D., George, K. A., Nelson, G. A., Reschke, M. F., Williams, T. J., & Paloski, W. H. (2020). Challenges to the central nervous system during human spaceflight missions to Mars. *Journal of Neurophysiology*, *123*(5), 2037–2063. https://doi.org/10.1152/JN.00476.2019

Committee on Assessment of Strategies for Managing Cancer Risks Associated with Radiation Exposure During Crewed Space Missions, Board on Health Sciences Policy, Board on Health Care Services, Health and Medicine Division, Nuclear and Radiation Studies Board, & Division on Earth and Life Studies. (2021). Space radiation and astronaut health. *Space Radiation and Astronaut Health*, 1–128. https://doi.org/10.17226/26155

Committee on the evaluation of radiation shielding for space exploration. (2008). Managing space radiation risk in the new era of space exploration. In *Managing Space Radiation Risk in the New Era of Space Exploration*. National Academies Press. https://doi.org/10.17226/12045

Concannon, C. G., Ward, M. W., Bonner, H. P., Kuroki, K., Tuffy, L. P., Bonner, C. T., Woods, I., Engel, T., Henshall, D. C., & Prehn, J. H. M. (2008). NMDA receptor-mediated excitotoxic neuronal apoptosis in vitro and in vivo occurs in an ER stress and PUMA independent manner. *Journal of Neurochemistry*, *105*(3), 891–903. https://doi.org/10.1111/J.1471-4159.2007.05187.X

Constanzo, J., Midavaine, É., Fouquet, J., Lepage, M., Descoteaux, M., Kirby, K., Tremblay, L., Masson-Côté, L., Geha, S., Longpré, J. M., Paquette, B., & Sarret, P. (2020). Brain irradiation leads to persistent neuroinflammation and long-term neurocognitive dysfunction in a region-specific manner. *Progress in Neuro-Psychopharmacology and Biological Psychiatry*, *102*, 109954. https://doi.org/10.1016/J.PNPBP.2020.109954

Cool, D. A., Kase, K. R., & Boice, J. D. (2019). NCRP Report no.180-management of exposure to ionizing radiation: NCRP radiation protection guidance for the United States. *Journal of Radiological Protection : Official Journal of the Society for Radiological Protection*, *39*(3), 966–977. https://doi.org/10.1088/1361-6498/AB1826

Cucinotta, F. A., & Cacao, E. (2017). Non-Targeted Effects Models Predict Significantly Higher Mars Mission Cancer Risk than Targeted Effects Models. *Scientific Reports 2017 7:1*, *7*(1), 1–11. https://doi.org/10.1038/s41598-017-02087-3

Cucinotta, F. A., & Cacao, E. (2019). Risks of cognitive detriments after low dose heavy ion and proton exposures. In *International Journal of Radiation Biology* (Vol. 95, Issue 7,

pp. 985–998). Taylor and Francis Ltd. https://doi.org/10.1080/09553002.2019.1623427

Cucinotta, F. A., & Durante, M. (2006). *Essay Cancer risk from exposure to galactic cosmic rays: implications for space exploration by human beings*. http://oncology.thelancet.comVol

Cucinotta, F. A., Kim, M.-H. Y., & Chappell, L. J. (2011). *Space radiation cancer risk projections and uncertainties - 2010.* http://www.sti.nasa.gov

Cucinotta, F. A., Nikjoo, H., & Goodhead, D. T. (2000). Model for Radial Dependence of Frequency Distributions for Energy Imparted in Nanometer Volumes from HZE Particles. *Radiation Research*, *153*(4), 459–468. https://bioone.org/journals/radiation-research/volume-153/issue-4/0033-7587(2000)153%5b0459%3aMFRDOF%5d2.0.CO%3b2/Model-for-Radial-Dependence-of-Frequency-Distributions-for-Energy-Imparted/10.1667/0033-7587(2000)153[0459:MFRDOF]2.0.CO;2.short

Daneman, R., & Prat, A. (2015). The blood-brain barrier. *Cold Spring Harbor Perspectives in Biology*, *7*(1). https://doi.org/10.1101/CSHPERSPECT.A020412

Davis, C. M., Allen, A. R., & Bowles, D. E. (2021). Consequences of space radiation on the brain and cardiovascular system. *Journal of Environmental Science and Health, Part C: Toxicology and Carcinogenesis*, *39*(2), 180–218. https://doi.org/10.1080/26896583.2021.1891825

De Los Santos, C. (2021). *Space Radiation: An Important Concern for Human Spaceflight*. Space Radiation Analysis Group (SRAG), Johnson Space Center,NASA. https://srag.jsc.nasa.gov/SpaceRadiation/Why/Why.cfm

Delbridge, A. R. D., Huh, D., Brickelmaier, M., Burns, J. C., Roberts, C., Challa, R., Raymond, N., Cullen, P., Carlile, T. M., Ennis, K. A., Liu, M., Sun, C., Allaire, N. E., Foos, M., Tsai, H.-H., Franchimont, N., Ransohoff, R. M., Butts, C., & Mingueneau, M. (2020). Organotypic Brain Slice Culture Microglia Exhibit Molecular Similarity to Acutely-Isolated Adult Microglia and Provide a Platform to Study Neuroinflammation. *Frontiers in Cellular Neuroscience*, *0*, 444. https://doi.org/10.3389/FNCEL.2020.592005

Di Maggio, F. M., Minafra, L., Forte, G. I., Cammarata, F. P., Lio, D., Messa, C., Gilardi, M. C., & Bravatà, V. (2015). Portrait of inflammatory response to ionizing radiation treatment. *Journal of Inflammation (United Kingdom)*, *12*(1), 1–11. https://doi.org/10.1186/S12950-015-0058-3/FIGURES/1

Diaz, S. L., Narboux-Nême, N., Trowbridge, S., Scotto-Lomassese, S., Kleine Borgmann, F. B., Jessberger, S., Giros, B., Maroteaux, L., Deneris, E., & Gaspar, P. (2013). Paradoxical increase in survival of newborn neurons in the dentate gyrus of mice with constitutive depletion of serotonin. *European Journal of Neuroscience*, *38*(5), 2650–2658. https://doi.org/10.1111/EJN.12297

Durante, M. (2014). Space radiation protection: Destination Mars. In *Life Sciences in Space Research* (Vol. 1, Issue 1, pp. 2–9). Elsevier Ltd. https://doi.org/10.1016/j.lssr.2014.01.002

Durante, M., & Bruno, C. (2010). Impact of rocket propulsion technology on the radiation risk in missions to Mars. *The European Physical Journal D 2010 60:1*, *60*(1), 215–218. https://doi.org/10.1140/EPJD/E2010-00035-6

Durante, M., & Cucinotta, F. A. (2008). Heavy ion carcinogenesis and human space exploration. *Nature Reviews | Cancer*, *8*, 465–472.

Elgart, S. R., Little, M. P., Chappell, L. J., Milder, C. M., Shavers, M. R., Huff, J. L., & Patel, Z. S. (2018). Radiation Exposure and Mortality from Cardiovascular Disease and Cancer in Early NASA Astronauts. *Scientific Reports*, *8*(1). https://doi.org/10.1038/s41598-018-25467-9

Fei, P., & El-Deiry, W. S. (2003). P53 and radiation responses. *Oncogene*, *22*(37), 5774–5783. https://doi.org/10.1038/SJ.ONC.1206677

Fike, J. R., Rola, R., & Limoli, C. L. (2007). Radiation response of neural precursor cells. *Neurosurgery Clinics of North America*, *18*(1), 115–127. https://doi.org/10.1016/J.NEC.2006.10.010

Fiorica, F., Giorgi, C., Rödel, F., Schmal, Z., & Rübe, C. E. (2022). Region-Specific Effects of Fractionated Low-Dose Versus Single-Dose Radiation on Hippocampal Neurogenesis and Neuroinflammation. *Cancers*, *14*(22), 5477–5477. https://doi.org/10.3390/CANCERS14225477

Fitzgerald, G. S., Chuchta, T. G., & McNay, E. C. (2023). Insulin-like growth factor-2 is a promising candidate for the treatment and prevention of Alzheimer's disease. *CNS Neuroscience & Therapeutics*, *29*(6), 1449–1469. https://doi.org/10.1111/CNS.14160

Fujita, Y., & Yamashita, T. (2021). Neuroprotective function of microglia in the developing brain. *Neuronal Signaling*, *5*(1), 20200024. https://doi.org/10.1042/NS20200024

Gähwiler, B. H., Capogna, M., Debanne, D., McKinney, R. A., & Thompson, S. M. (1997). Organotypic slice cultures: a technique has come of age. *Trends in Neurosciences*, *20*(10), 471–477. https://doi.org/10.1016/S0166-2236(97)01122-3

Galatro, T. F., Holtman, I. R., Lerario, A. M., Vainchtein, I. D., Brouwer, N., Sola, P. R., Veras, M. M., Pereira, T. F., Leite, R. E. P., Möller, T., Wes, P. D., Sogayar, M. C., Laman, J. D., Den Dunnen, W., Pasqualucci, C. A., Oba-Shinjo, S. M., Boddeke, E. W. G. M., Marie, S. K. N., & Eggen, B. J. L. (2017). Transcriptomic analysis of purified human cortical microglia reveals age-associated changes. *Nature Neuroscience*, *20*(8), 1162–1171. https://doi.org/10.1038/NN.4597

Gan, C., Li, W., Xu, J., Pang, L., Tang, L., Yu, S., Li, A., Ge, H., Huang, R., & Cheng, H. (2023). Advances in the study of the molecular biological mechanisms of radiation-induced brain injury. *American Journal of Cancer Research*, *13*(8), 3275. /pmc/articles/PMC10492106/

Gemma, C., & Bachstetter, A. D. (2013). The role of microglia in adult hippocampal neurogenesis. *Frontiers in Cellular Neuroscience*, *7*(NOV), 46146. https://doi.org/10.3389/FNCEL.2013.00229/BIBTEX

Gerlach, J., Donkels, C., Münzner, G., & Haas, C. A. (2016). Persistent gliosis interferes with neurogenesis in organotypic hippocampal slice cultures. *Frontiers in Cellular Neuroscience*, *10*(MAY), 181549. https://doi.org/10.3389/FNCEL.2016.00131/BIBTEX

Ginhoux, F., & Guilliams, M. (2016). Tissue-Resident Macrophage Ontogeny and Homeostasis. *Immunity*, *44*(3), 439–449. https://doi.org/10.1016/J.IMMUNI.2016.02.024

Girdhani, S., Sachs, R., & Hlatky, L. (2013). Biological effects of proton radiation: what we know and don't know. *Radiation Research*, *179*(3), 257–272. https://doi.org/10.1667/RR2839.1

Gómez-Virgilio, L., Silva-Lucero, M. D. C., Flores-Morelos, D. S., Gallardo-Nieto, J., Lopez-Toledo, G., Abarca-Fernandez, A. M., Zacapala-Gómez, A. E., Luna-Muñoz, J., Montiel-Sosa, F., Soto-Rojas, L. O., Pacheco-Herrero, M., & Cardenas-Aguayo, M. D. C. (2022). Autophagy: A Key Regulator of Homeostasis and Disease: An Overview of Molecular Mechanisms and Modulators. *Cells*, *11*(15). https://doi.org/10.3390/CELLS11152262

Gosselin, D., Skola, D., Coufal, N. G., Holtman, I. R., Schlachetzki, J. C. M., Sajti, E., Jaeger, B. N., O'Connor, C., Fitzpatrick, C., Pasillas, M. P., Pena, M., Adair, A., Gonda, D. D., Levy, M. L., Ransohoff, R. M., Gage, F. H., & Glass, C. K. (2017). An environment-dependent

transcriptional network specifies human microglia identity. *Science (New York, N.Y.)*, *356*(6344), 1248–1259. https://doi.org/10.1126/SCIENCE.AAL3222

Grabiec, U., Koch, M., Kallendrusch, S., Kraft, R., Hill, K., Merkwitz, C., Ghadban, C., Lutz, B., Straiker, A., & Dehghani, F. (2012). The endocannabinoid N-arachidonoyldopamine (NADA) exerts neuroprotective effects after excitotoxic neuronal damage via cannabinoid receptor 1 (CB 1). *Neuropharmacology*, *62*(4), 1797–1807. https://doi.org/10.1016/j.neuropharm.2011.11.023

Guan, J., Stewart, J., Ware, J. H., Zhou, Z., Donahue, J. J., & Kennedy, A. R. (2006). Effects of dietary supplements on the space radiation-induced reduction in total antioxidant status in CBA mice. *Radiation Research*, *165*(4), 373–378. https://doi.org/10.1667/RR3523.1

Guo, J., Zeitlin, C., Wimmer-Schweingruber, R. F., Hassler, D. M., Posner, A., Heber, B., Köhler, J., Rafkin, S., Ehresmann, B., Appel, J. K., Böhm, E., Böttcher, S., Burmeister, S., Brinza, D. E., Lohf, H., Martin, C., & Reitz, G. (2015). Variations of dose rate observed by MSL/RAD in transit to Mars. *Astronomy and Astrophysics*, *577*. https://doi.org/10.1051/0004-6361/201525680

Gupta, M., Mishra, S. K., Kumar, B. S. H., Khushu, S., & Rana, P. (2017). Early detection of whole body radiation induced microstructural and neuroinflammatory changes in hippocampus: A diffusion tensor imaging and gene expression study. *Journal of Neuroscience Research*, *95*(4), 1067–1078. https://doi.org/10.1002/JNR.23833

Hall, E. J., & Giaccia, A. J. (2019). *Radiobiology for the radiologist* (8th ed.). Wolters Kluwer.

Han, W., Umekawa, T., Zhou, K., Zhang, X. M., Ohshima, M., Dominguez, C. A., Harris, R. A., Zhu, C., & Blomgren, K. (2016). Cranial irradiation induces transient microglia accumulation, followed by long-lasting inflammation and loss of microglia. *Oncotarget*, *7*(50), 82305–82323. https://doi.org/10.18632/ONCOTARGET.12929

Haspula, D., & Clark, M. A. (2020). Cannabinoid Receptors: An Update on Cell Signaling, Pathophysiological Roles and Therapeutic Opportunities in Neurological, Cardiovascular, and Inflammatory Diseases. *International Journal of Molecular Sciences*, *21*(20), 1–65. https://doi.org/10.3390/IJMS21207693

Heindl, S., Gesierich, B., Benakis, C., Llovera, G., Duering, M., & Liesz, A. (2018). Automated Morphological Analysis of Microglia After Stroke. *Frontiers in Cellular Neuroscience*, *0*, 106. https://doi.org/10.3389/FNCEL.2018.00106

Held, K. D., Kawamura, H., Kaminuma, T., Paz, A. E. S., Yoshida, Y., Liu, Q., Willers, H., & Takahashi, A. (2016). Effects of charged particles on human tumor cells. *Frontiers in Oncology*, *6*(FEB), 173722. https://doi.org/10.3389/FONC.2016.00023/BIBTEX

Helm, A., & Fournier, C. (2023). High-LET charged particles: radiobiology and application for new approaches in radiotherapy. *Strahlentherapie Und Onkologie*, *199*(12), 1225. https://doi.org/10.1007/S00066-023-02158-7

Herkenham, M., Lynn, A. B., Johnson, M. R., Melvin, L. S., De Costa, B. R., & Rice, K. C. (1991). Characterization and localization of cannabinoid receptors in rat brain: a quantitative in vitro autoradiographic study. *The Journal of Neuroscience : The Official Journal of the Society for Neuroscience*, *11*(2), 563–583. https://doi.org/10.1523/JNEUROSCI.11-02-00563.1991

Herzog, K.-H., Chong, M. J., Kapsetaki, M., Morgan, J. I., McKinnon, P. J., Herzog, K.-H., Chong, M. J., Kapsetaki, M., Morgan, J. I., & McKinnon, P. J. (1998). Requirement for Atm in Ionizing Radiation-Induced Cell Death in the Developing Central Nervous System. *Sci*, *280*(5366), 1089. https://doi.org/10.1126/SCIENCE.280.5366.1089

Heuskin, A. C., Osseiran, A. I., Tang, J., & Costes, S. V. (2016). Simulating Space Radiation-Induced Breast Tumor Incidence Using Automata. *Radiation Research*, *186*(1), 27–38. https://doi.org/10.1667/RR14338.1

Hinz, M., Stilmann, M., Arslan, S. Ç., Khanna, K. K., Dittmar, G., & Scheidereit, C. (2010). A cytoplasmic ATM-TRAF6-cIAP1 module links nuclear DNA damage signaling to ubiquitin-mediated NF-κB activation. *Molecular Cell*, *40*(1), 63–74. https://doi.org/10.1016/J.MOLCEL.2010.09.008

Hladik, D., & Tapio, S. (2016). Effects of ionizing radiation on the mammalian brain. *Mutation Research*, *770*, 219–230. https://doi.org/10.1016/J.MRREV.2016.08.003

Holopainen, I. E. (2005). Organotypic Hippocampal Slice Cultures: A Model System to Study Basic Cellular and Molecular Mechanisms of Neuronal Cell Death, Neuroprotection, and Synaptic Plasticity. *Neurochemical Research*, *30*(12), 1521–1528. https://doi.org/10.1007/S11064-005-8829-5

Holopainen, I. E., Järvelä, J., Lopez-Picon, F. R., Pelliniemi, L. J., & Kukko-Lukjanov, T. K. (2004). Mechanisms of kainate-induced region-specific neuronal death in immature organotypic hippocampal slice cultures. *Neurochemistry International*, *45*(1), 1–10. https://doi.org/10.1016/J.NEUINT.2004.01.005

Humpel, C. (2015). Organotypic brain slice cultures: A review. *Neuroscience*, *305*, 86–98. https://doi.org/10.1016/J.NEUROSCIENCE.2015.07.086

ICRP Publication103. (2007). *Annals of the ICRP Published on behalf of the International Commission on Radiological Protection*.

Impey, S., Jopson, T., Pelz, C., Tafessu, A., Fareh, F., Zuloaga, D., Marzulla, T., Riparip, L. K., Stewart, B., Rosi, S., Turker, M. S., & Raber, J. (2016). Short- and long-term effects of 56Fe irradiation on cognition and hippocampal DNA methylation and gene expression. *BMC Genomics*, *17*(1). https://doi.org/10.1186/S12864-016-3110-7

Jain, S., LaFrancois, J. J., Botterill, J. J., Alcantara-Gonzalez, D., Scharfman, H. E., & Helen Scharfman, C. E. (2019). Adult neurogenesis in the mouse dentate gyrus protects the hippocampus from neuronal injury following severe seizures. *Hippocampus*, *29*, 638–709. https://doi.org/10.1002/hipo.23062

Kamada, T., Tsujii, H., Blakely, E. A., Debus, J., De Neve, W., Durante, M., Jäkel, O., Mayer, R., Orecchia, R., Pötter, R., Vatnitsky, S., & Chu, W. T. (2015). Carbon ion radiotherapy in Japan: an assessment of 20 years of clinical experience. *The Lancet. Oncology*, *16*(2), e93–e100. https://doi.org/10.1016/S1470-2045(14)70412-7

Kano, M., Ohno-Shosaku, T., Hashimotodani, Y., Uchigashima, M., & Watanabe, M. (2009). Endocannabinoid-mediated control of synaptic transmission. *Physiological Reviews*, *89*(1), 309–380. https://doi.org/10.1152/PHYSREV.00019.2008

Kempermann, G., Gast, D., Kronenberg, G., Yamaguchi, M., & Gage, F. H. (2003). Early determination and long-term persistence of adult-generated new neurons in the hippocampus of mice. *Development*, *130*(2), 391–399. https://doi.org/10.1242/DEV.00203

Kempermann, G., Jessberger, S., Steiner, B., & Kronenberg, G. (2004). Milestones of neuronal development in the adult hippocampus. *Trends in Neurosciences*, *27*(8), 447–452. https://doi.org/10.1016/J.TINS.2004.05.013

Kempuraj, D., & Mohan, R. R. (2022). Autophagy in Extracellular Matrix and Wound Healing Modulation in the Cornea. *Biomedicines*, *10*(2). https://doi.org/10.3390/BIOMEDICINES10020339

Kennedy, A. R., & Wan, X. S. (2011). Countermeasures for space radiation induced adverse biologic effects. *Advances in Space Research*, *48*(9), 1460–1479. https://doi.org/10.1016/J.ASR.2011.07.007

Kennedy, A. R., Zhou, Z., Donahue, J. J., & Ware, J. H. (2006). Protection against adverse biological effects induced by space radiation by the Bowman-Birk inhibitor and antioxidants. *Radiation Research*, *166*(2), 327–332. https://doi.org/10.1667/RR3599.1

Kiffer, F., Howe, A. K., Carr, H., Wang, J., Alexander, T., Anderson, J. E., Groves, T., Seawright, J. W., Sridharan, V., Carter, G., Boerma, M., & Allen, A. R. (2018). Late effects of 1H irradiation on hippocampal physiology. *Life Sciences in Space Research*, *17*, 51–62. https://doi.org/10.1016/J.LSSR.2018.03.004

Kigerl, K. A., Gensel, J. C., Ankeny, D. P., Alexander, J. K., Donnelly, D. J., & Popovich, P. G. (2009). Identification of two distinct macrophage subsets with divergent effects causing either neurotoxicity or regeneration in the injured mouse spinal cord. *The Journal of Neuroscience : The Official Journal of the Society for Neuroscience*, *29*(43), 13435–13444. https://doi.org/10.1523/JNEUROSCI.3257-09.2009

Kim, E. M., & Hwang, O. (2011). Role of matrix metalloproteinase-3 in neurodegeneration. *Journal of Neurochemistry*, *116*(1), 22–32. https://doi.org/10.1111/J.1471-4159.2010.07082.X

Klein, P. M., Parihar, V. K., Szabo, G. G., Zöldi, M., Angulo, M. C., Allen, B. D., Amin, A. N., Nguyen, Q. A., Katona, I., Baulch, J. E., Limoli, C. L., & Soltesz, I. (2021). Detrimental impacts of mixed-ion radiation on nervous system function. *Neurobiology of Disease*, *151*, 105252. https://doi.org/10.1016/J.NBD.2021.105252

Kong, W., Li, H., Tuma, R. F., & Ganea, D. (2014). Selective CB2 receptor activation ameliorates EAE by reducing Th17 differentiation and immune cell accumulation in the CNS. *Cellular Immunology*, *287*(1), 1–17. https://doi.org/10.1016/j.cellimm.2013.11.002

Kouvaris, J. R., Kouloulias, V. E., & Vlahos, L. J. (2007). Amifostine: the first selective-target and broad-spectrum radioprotector. *The Oncologist*, *12*(6), 738–747. https://doi.org/10.1634/THEONCOLOGIST.12-6-738

Koyama, R., & Ikegaya, Y. (2018). The molecular and cellular mechanisms of axon guidance in mossy fiber sprouting. *Frontiers in Neurology*, *9*(MAY), 357272. https://doi.org/10.3389/FNEUR.2018.00382/BIBTEX

Kozela, E., Lev, N., Kaushansky, N., Eilam, R., Rimmerman, N., Levy, R., Ben-Nun, A., Juknat, A., & Vogel, Z. (2011). Cannabidiol inhibits pathogenic T cells, decreases spinal microglial activation and ameliorates multiple sclerosis-like disease in C57BL/6 mice. *British Journal of Pharmacology*, *163*(7), 1507. https://doi.org/10.1111/J.1476-5381.2011.01379.X

Krämer, M. (1995). Calculation of heavy-ion track structure. *Nuclear Instruments and Methods in Physics Research Section B: Beam Interactions with Materials and Atoms*, *105*(1–4), 14–20. https://doi.org/10.1016/0168-583X(95)00538-2

Kreutzberg, G. W. (1996). Microglia: a sensor for pathological events in the CNS. *Trends in Neurosciences*, *19*(8), 312–318. https://doi.org/10.1016/0166-2236(96)10049-7

Krohn, R. M., Parsons, S. A., Fichna, J., Patel, K. D., Yates, R. M., Sharkey, K. A., & Storr, M. A. (2016). Abnormal cannabidiol attenuates experimental colitis in mice, promotes wound healing and inhibits neutrophil recruitment. *Journal of Inflammation (United Kingdom)*, *13*(1). https://doi.org/10.1186/s12950-016-0129-0

Krukowski, K., Grue, K., Becker, M., Elizarraras, E., Frias, E. S., Halvorsen, A., Koenig-Zanoff, M., Frattini, V., Nimmagadda, H., Feng, X., Jones, T., Nelson, G., Ferguson, A. R., & Rosi, S. (2021). The impact of deep space radiation on cognitive performance: From biological sex to biomarkers to countermeasures. *Science Advances*, *7*(42), 6702–6717. https://doi.org/10.1126/SCIADV.ABG6702/SUPPL_FILE/SCIADV.ABG6702_SM.PDF

Krukowski, K., Grue, K., Frias, E. S., Pietrykowski, J., Jones, T., Nelson, G., & Rosi, S. (2018). Female mice are protected from space radiation-induced maladaptive responses. *Brain, Behavior, and Immunity*, *74*, 106. https://doi.org/10.1016/J.BBI.2018.08.008

Lee, S. H., Dudok, B., Parihar, V. K., Jung, K. M., Zöldi, M., Kang, Y. J., Maroso, M., Alexander, A. L., Nelson, G. A., Piomelli, D., Katona, I., Limoli, C. L., & Soltesz, I. (2017). Neurophysiology of space travel: energetic solar particles cause cell type-specific plasticity of neurotransmission. *Brain Structure and Function*, *222*(5), 2345–2357. https://doi.org/10.1007/s00429-016-1345-3

Lee, W. H., Sonntag, W. E., Mitschelen, M., Yan, H., & Lee, Y. W. (2010). Irradiation induces regionally specific alterations in pro-inflammatory environments in rat brain. *International Journal of Radiation Biology*, *86*(2), 132. https://doi.org/10.3109/09553000903419346

Li, M., Gonon, G., Buonanno, M., Autsavapromporn, N., De Toledo, S. M., Pain, D., & Azzam, E. I. (2014). Health risks of space exploration: targeted and nontargeted oxidative injury by high-charge and high-energy particles. *Antioxidants & Redox Signaling*, *20*(9), 1501–1523. https://doi.org/10.1089/ARS.2013.5649

Li, Q., Han, X., & Wang, J. (2016). Organotypic Hippocampal Slices as Models for Stroke and Traumatic Brain Injury. *Molecular Neurobiology*, *53*(6), 4226–4237. https://doi.org/10.1007/S12035-015-9362-4

Li, Y., & Kim, J. (2016). Deletion of CB2 cannabinoid receptors reduces synaptic transmission and long-term potentiation in the mouse hippocampus. *Hippocampus*, *26*(3), 275–281. https://doi.org/10.1002/HIPO.22558

Liang, X., Hsu, L. M., Lu, H., Ash, J. A., Rapp, P. R., & Yang, Y. (2020). Functional Connectivity of Hippocampal CA3 Predicts Neurocognitive Aging via CA1-Frontal Circuit. *Cerebral Cortex (New York, N.Y. : 1991)*, *30*(8), 4297–4305. https://doi.org/10.1093/CERCOR/BHAA008

Limoli, C. (2020). Can a comparison of clinical and deep space irradiation scenarios shed light on the radiation response of the brain? *The British Journal of Radiology*, *93*(1115). https://doi.org/10.1259/BJR.20200245

Liu, B., Hinshaw, R. G., Le, K. X., Park, M. A., Wang, S., Belanger, A. P., Dubey, S., Frost, J. L., Shi, Q., Holton, P., Trojanczyk, L., Reiser, V., Jones, P. A., Trigg, W., Di Carli, M. F., Lorello, P., Caldarone, B. J., Williams, J. P., O'Banion, M. K., & Lemere, C. A. (2019). Space-like 56Fe irradiation manifests mild, early sex-specific behavioral and neuropathological changes in wildtype and Alzheimer's-like transgenic mice. *Scientific Reports*, *9*(1). https://doi.org/10.1038/s41598-019-48615-1

Liu, Q., Huang, Y., Duan, M., Yang, Q., Ren, B., & Tang, F. (2022). Microglia as Therapeutic Target for Radiation-Induced Brain Injury. *International Journal of Molecular Sciences*, *23*(15). https://doi.org/10.3390/IJMS23158286

Liu, Y., Ma, H., Wang, Y., Ren, B., Liu, L., Sun, A., & Tang, F. (2023). Neonatal exposure to low-dose X-ray causes behavioral defects and abnormal hippocampal development in mice. *IUBMB Life*, *75*(6), 530–547. https://doi.org/10.1002/IUB.2703

Lomax, M. E., Folkes, L. K., & O'Neill, P. (2013). Biological consequences of radiation-induced DNA damage: relevance to radiotherapy. *Clinical Oncology (Royal College of Radiologists (Great Britain))*, *25*(10), 578–585. https://doi.org/10.1016/J.CLON.2013.06.007

Lorente de Nó, R. (1934). Studies on the structure of the cerebral cortex. II. Continuation of the study of the ammonic system. - PsycNET. *Journal Für Psychologie Und Neurologie*, *46*, 113–177. https://psycnet.apa.org/record/1935-01111-001

Louveau, A., Smirnov, I., Keyes, T. J., Eccles, J. D., Rouhani, S. J., Peske, J. D., Derecki, N. C., Castle, D., Mandell, J. W., Lee, K. S., Harris, T. H., & Kipnis, J. (2015). Structural and functional features of central nervous system lymphatic vessels. *Nature 2015 523:7560*, *523*(7560), 337–341. https://doi.org/10.1038/nature14432

Lumniczky, K., Szatmári, T., & Sáfrány, G. (2017). Ionizing radiation-induced immune and inflammatory reactions in the brain. *Frontiers in Immunology*, *8*(MAY), 517. https://doi.org/10.3389/FIMMU.2017.00517/BIBTEX

Maier, P., Hartmann, L., Wenz, F., & Herskind, C. (2016). Cellular Pathways in Response to Ionizing Radiation and Their Targetability for Tumor Radiosensitization. *International Journal of Molecular Sciences 2016, Vol. 17, Page 102*, *17*(1), 102. https://doi.org/10.3390/IJMS17010102

Marples, B., & Collis, S. J. (2008). Low-dose hyper-radiosensitivity: past, present, and future. *International Journal of Radiation Oncology, Biology, Physics*, *70*(5), 1310–1318. https://doi.org/10.1016/J.IJROBP.2007.11.071

Martinez, F. O., & Gordon, S. (2014). The M1 and M2 paradigm of macrophage activation: time for reassessment. *F1000Prime Reports*, *6*, 13. https://doi.org/10.12703/P6-13

Martínez-Pinilla, E., Aguinaga, D., Navarro, G., Rico, A. J., Oyarzábal, J., Sánchez-Arias, J. A., Lanciego, J. L., & Franco, R. (2019). Targeting CB1 and GPR55 Endocannabinoid Receptors as a Potential Neuroprotective Approach for Parkinson's Disease. *Molecular Neurobiology*, *56*(8), 5900–5910. https://doi.org/10.1007/S12035-019-1495-4/FIGURES/10

Mathur, V., Burai, R., Vest, R. T., Bonanno, L. N., Lehallier, B., Zardeneta, M. E., Mistry, K. N., Do, D., Marsh, S. E., Abud, E. M., Blurton-Jones, M., Li, L., Lashuel, H. A., & Wyss-Coray, T. (2017). Activation of the STING-Dependent Type I Interferon Response Reduces Microglial Reactivity and Neuroinflammation. *Neuron*, *96*(6), 1290-1302.e6. https://doi.org/10.1016/J.NEURON.2017.11.032

Merlini, M., Rafalski, V. A., Ma, K., Kim, K. Y., Bushong, E. A., Rios Coronado, P. E., Yan, Z., Mendiola, A. S., Sozmen, E. G., Ryu, J. K., Haberl, M. G., Madany, M., Sampson, D. N., Petersen, M. A., Bardehle, S., Tognatta, R., Dean, T., Acevedo, R. M., Cabriga, B., … Akassoglou, K. (2020). Microglial Gi-dependent dynamics regulate brain network hyperexcitability. *Nature Neuroscience 2020 24:1*, *24*(1), 19–23. https://doi.org/10.1038/s41593-020-00756-7

Mewaldt, R. A. (1994). Galactic cosmic ray composition and energy spectra. *Advances in Space Research : The Official Journal of the Committee on Space Research (COSPAR)*, *14*(10), 737–747. https://doi.org/10.1016/0273-1177(94)90536-3

Mildner, A., Schmidt, H., Nitsche, M., Merkler, D., Hanisch, U. K., Mack, M., Heikenwalder, M., Brück, W., Priller, J., & Prinz, M. (2007). Microglia in the adult brain arise from Ly-6ChiCCR2+ monocytes only under defined host conditions. *Nature Neuroscience*, *10*(12), 1544–1553. https://doi.org/10.1038/NN2015

Mizumatsu, S., Monje, M. L., Monhardt, D. R., Rola, R., Palmer, T. D., & Fike, J. R. (2003). Extreme Sensitivity of Adult Neurogenesis to Low Doses of X-Irradiation1 | Cancer Research | American Association for Cancer Research. *Cancer Research*, *Volume 63*(Issue 14). https://aacrjournals.org/cancerres/article/63/14/4021/510158/Extreme-Sensitivity-of-Adult-Neurogenesis-to-Low

Montay-Gruel, P., Acharya, M. M., Petersson, K., Alikhani, L., Yakkala, C., Allen, B. D., Ollivier, J., Petit, B., Jorge, P. G., Syage, A. R., Nguyen, T. A., Baddour, A. A. D., Lu, C., Singh, P., Moeckli, R., Bochud, F., Germond, J. F., Froidevaux, P., Bailat, C., … Limoli, C. L. (2019). Long-term neurocognitive benefits of FLASH radiotherapy driven by reduced reactive oxygen species. *Proceedings of the National Academy of Sciences of the United States of America*, *116*(22), 10943–10951. https://doi.org/10.1073/PNAS.1901777116

Moreno-Villanueva, M., Wong, M., Lu, T., Zhang, Y., & Wu, H. (2017). Interplay of space radiation and microgravity in DNA damage and DNA damage response. *NPJ Microgravity*, *3*(1). https://doi.org/10.1038/S41526-017-0019-7

Morganti, J. M., Nash, K. R., Grimmig, B. A., Ranjit, S., Small, B., Bickford, P. C., & Gemma, C. (2012). The Soluble Isoform of CX3CL1 Is Necessary for Neuroprotection in a Mouse Model of Parkinson's Disease. *The Journal of Neuroscience*, *32*(42), 14592. https://doi.org/10.1523/JNEUROSCI.0539-12.2012

Muller, D., Toni, N., Buchs, P.-A., Parisi, L., & Stoppini, L. (2003). Interface Organotypic Hippocampal Slice Cultures. In *Protocols for Neural Cell Culture* (pp. 13–27). Humana Press. https://doi.org/10.1385/1-59259-207-4:13

Murray, P. J., Allen, J. E., Biswas, S. K., Fisher, E. A., Gilroy, D. W., Goerdt, S., Gordon, S., Hamilton, J. A., Ivashkiv, L. B., Lawrence, T., Locati, M., Mantovani, A., Martinez, F. O., Mege, J. L., Mosser, D. M., Natoli, G., Saeij, J. P., Schultze, J. L., Shirey, K. A., … Wynn, T. A. (2014). Macrophage activation and polarization: nomenclature and experimental guidelines. *Immunity*, *41*(1), 14–20. https://doi.org/10.1016/J.IMMUNI.2014.06.008

Naito, M., Kitamura, H., Koike, M., Kusano, H., Kusumoto, T., Uchihori, Y., Endo, T., Hagiwara, Y., Kiyono, N., Kodama, H., Matsuo, S., Mikoshiba, R., Takami, Y., Yamanaka, M., Akiyama, H., Nishimura, W., & Kodaira, S. (2021). Applicability of composite materials for space radiation shielding of spacecraft. *Life Sciences in Space Research*, *31*, 71–79. https://doi.org/10.1016/J.LSSR.2021.08.004

Naito, M., Kodaira, S., Ogawara, R., Tobita, K., Someya, Y., Kusumoto, T., Kusano, H., Kitamura, H., Koike, M., Uchihori, Y., Yamanaka, M., Mikoshiba, R., Endo, T., Kiyono, N., Hagiwara, Y., Kodama, H., Matsuo, S., Takami, Y., Sato, T., & Orimo, S. ichi. (2020). Investigation of shielding material properties for effective space radiation protection. *Life Sciences in Space Research*, *26*, 69–76. https://doi.org/10.1016/J.LSSR.2020.05.001

Narayanan, I. V., Paulsen, M. T., Bedi, K., Berg, N., Ljungman, E. A., Francia, S., Veloso, A., Magnuson, B., Di Fagagna, F. D. A., Wilson, T. E., & Ljungman, M. (2017). Transcriptional and post-transcriptional regulation of the ionizing radiation response by ATM and p53. *Scientific Reports*, *7*. https://doi.org/10.1038/SREP43598

Norbury, J. W., Schimmerling, W., Slaba, T. C., Azzam, E. I., Badavi, F. F., Baiocco, G., Benton, E., Bindi, V., Blakely, E. A., Blattnig, S. R., Boothman, D. A., Borak, T. B., Britten, R. A., Curtis, S., Dingfelder, M., Durante, M., Dynan, W. S., Eisch, A. J., Robin Elgart, S., … Zeitlin, C. J. (2016). Galactic cosmic ray simulation at the NASA Space Radiation Laboratory. *Life Sciences in Space Research*, *8*, 38–51. https://doi.org/10.1016/j.lssr.2016.02.001

Papez, J. W. (1995). A proposed mechanism of emotion. 1937. *The Journal of Neuropsychiatry and Clinical Neurosciences*, *7*(1), 103–112. https://doi.org/10.1176/JNP.7.1.103

Parihar, V. K., Allen, B. D., Caressi, C., Kwok, S., Chu, E., Tran, K. K., Chmielewski, N. N., Giedzinski, E., Acharya, M. M., Britten, R. A., Baulch, J. E., & Limoli, C. L. (2016). Cosmic radiation exposure and persistent cognitive dysfunction. *Scientific Reports 2016 6:1*, *6*(1), 1–14. https://doi.org/10.1038/srep34774

Parihar, V. K., Allen, B., Tran, K. K., Macaraeg, T. G., Chu, E. M., Kwok, S. F., Chmielewski, N. N., Craver, B. M., Baulch, J. E., Acharya, M. M., Cucinotta, F. A., & Limoli, C. L. (2015). What happens to your brain on the way to Mars. *Science Advances*, *1*(4). https://doi.org/10.1126/SCIADV.1400256/SUPPL_FILE/1400256_SM.PDF

Parihar, V. K., Maroso, M., Syage, A., Allen, B. D., Angulo, M. C., Soltesz, S., & Limoli, C. L. (2018). Persistent nature of alterations in cognition and neuronal circuit excitability

after exposure to simulated cosmic radiation in mice. *Experimental Neurology*, *305*, 44–55. https://doi.org/10.1016/J.EXPNEUROL.2018.03.009

Patel, M., Grimsey, N. L., Banister, S. D., Finlay, D. B., & Glass, M. (2023). Evaluating signaling bias for synthetic cannabinoid receptor agonists at the cannabinoid CB2 receptor. *Pharmacology Research & Perspectives*, *11*(6). https://doi.org/10.1002/PRP2.1157

Prinz, M., Masuda, T., Wheeler, M. A., & Quintana, F. J. (2021a). Microglia and Central Nervous System–Associated Macrophages—From Origin to Disease Modulation. *Annual Review of Immunology*, *39*, 251. https://doi.org/10.1146/ANNUREV-IMMUNOL-093019-110159

Prinz, M., Masuda, T., Wheeler, M. A., & Quintana, F. J. (2021b). Microglia and Central Nervous System-Associated Macrophages-From Origin to Disease Modulation. *Annual Review of Immunology*, *39*, 251–277. https://doi.org/10.1146/ANNUREV-IMMUNOL-093019-110159

Raber, J., Yamazaki, J., Torres, E. R. S., Kirchoff, N., Stagaman, K., Sharpton, T., Turker, M. S., & Kronenberg, A. (2019). Combined Effects of Three High-Energy Charged Particle Beams Important for Space Flight on Brain, Behavioral and Cognitive Endpoints in B6D2F1 Female and Male Mice. *Frontiers in Physiology*, *10*(MAR), 179. https://doi.org/10.3389/FPHYS.2019.00179

Ransohoff, R. M. (2016). A polarizing question: do M1 and M2 microglia exist? *Nature Neuroscience*, *19*(8), 987–991. https://doi.org/10.1038/NN.4338

Ribak, C. E., Seress, L., & Amaral, D. G. (1985). The development, ultrastructure and synaptic connections of the mossy cells of the dentate gyrus. *Journal of Neurocytology 1985 14:5*, *14*(5), 835–857. https://doi.org/10.1007/BF01170832

Rienecker, K. D. A., Paladini, M. S., Grue, K., Krukowski, K., & Rosi, S. (2021). Microglia: Ally and Enemy in Deep Space. *Neuroscience & Biobehavioral Reviews*, *126*, 509–514. https://doi.org/10.1016/J.NEUBIOREV.2021.03.036

Rivera, P. D., Shih, H. Y., Leblanc, J. A., Cole, M. G., Amaral, W. Z., Mukherjee, S., Zhang, S., Lucero, M. C., Decarolis, N. A., Chen, B. P., & Eisch, A. J. (2013). Acute and fractionated exposure to high-LET (56)Fe HZE-particle radiation both result in similar long-term deficits in adult hippocampal neurogenesis. *Radiation Research*, *180*(6), 658–667. https://doi.org/10.1667/RR13480.1

Robinson, N. T. M., Descamps, L. A. L., Russell, L. E., Buchholz, M. O., Bicknell, B. A., Antonov, G. K., Lau, J. Y. N., Nutbrown, R., Schmidt-Hieber, C., & Häusser, M. (2020). Targeted Activation of Hippocampal Place Cells Drives Memory-Guided Spatial Behavior. *Cell*, *183*(7), 2041–2042. https://doi.org/10.1016/j.cell.2020.12.010

Robledo-Menendez, A., Vella, M., Grandes, P., & Soria-Gomez, E. (2022). Cannabinoid control of hippocampal functions: the where matters. *The FEBS Journal*, *289*(8), 2162–2175. https://doi.org/10.1111/FEBS.15907

Rola, R., Fishman, K., Baure, J., Rosi, S., Lamborn, K. R., Obenaus, A., Nelson, G. A., & Fike, J. R. (2008a). Hippocampal neurogenesis and neuroinflammation after cranial irradiation with 56Fe particles. *Radiation Research*, *169*(6), 626–632. https://doi.org/10.1667/RR1263.1

Rola, R., Fishman, K., Baure, J., Rosi, S., Lamborn, K. R., Obenaus, A., Nelson, G. A., & Fike, J. R. (2008b). Hippocampal neurogenesis and neuroinflammation after cranial irradiation with 56Fe particles. *Radiation Research*, *169*(6), 626–632. https://doi.org/10.1667/RR1263.1

Rola, R., Otsuka, S., Obenaus, A., Nelson, G. A., Limoli, C. L., VandenBerg, S. R., & Fike, J. R. (2004). Indicators of hippocampal neurogenesis are altered by 56Fe-particle

irradiation in a dose-dependent manner. *Radiation Research*, *162*(4), 442–446. https://doi.org/10.1667/RR3234

Ronaldson, P. T., & Davis, T. P. (2020). Regulation of blood–brain barrier integrity by microglia in health and disease: A therapeutic opportunity. *Journal of Cerebral Blood Flow & Metabolism*, *40*(1 Suppl), S6. https://doi.org/10.1177/0271678X20951995

Roy, A., Bera, S., Saso, L., & Dwarakanath, B. S. (2022). Role of autophagy in tumor response to radiation: Implications for improving radiotherapy. *Frontiers in Oncology*, *12*. https://doi.org/10.3389/FONC.2022.957373

Ruiz, S., Buyukturkoglu, K., Rana, M., Birbaumer, N., & Sitaram, R. (2014). Real-time fMRI brain computer interfaces: Self-regulation of single brain regions to networks. *Biological Psychology*, *95*, 4–20. https://doi.org/10.1016/j.biopsycho.2013.04.010

Saliba, S. W., Gläser, F., Deckers, A., Keil, A., Hurrle, T., Apweiler, M., Ferver, F., Volz, N., Endres, D., Bräse, S., & Fiebich, B. L. (2021). Effects of a Novel GPR55 Antagonist on the Arachidonic Acid Cascade in LPS-Activated Primary Microglial Cells. *International Journal of Molecular Sciences*, *22*(5), 1–16. https://doi.org/10.3390/IJMS22052503

Sato, K. (2015). Effects of Microglia on Neurogenesis. *Glia*, *63*(8), 1394–1405. https://doi.org/10.1002/GLIA.22858

Sato, W., Zhu, X., Rana, M., Yan, B., Zhu, Y., Gao, H., Tong, L., Li, Z., Wang, L., Zhang, C., & Yang, Q. (2019). *Emotion Regulation of Hippocampus Using Real-Time fMRI Neurofeedback in Healthy Human*. https://doi.org/10.3389/fnhum.2019.00242

Sawzdargo, M., Nguyen, T., Lee, D. K., Lynch, K. R., Cheng, R., Heng, H. H. Q., George, S. R., & O'Dowd, B. F. (1999). Identification and cloning of three novel human G protein-coupled receptor genes GPR52, ΨGPR53 and GPR55: GPR55 is extensively expressed in human brain. *Molecular Brain Research*, *64*(2), 193–198. https://doi.org/10.1016/S0169-328X(98)00277-0

Scharfman, H. E. (2007). The CA3 "backprojection" to the dentate gyrus. *Progress in Brain Research*, *163*, 627–637. https://doi.org/10.1016/S0079-6123(07)63034-9

Schmal, Z., Hammer, B., Müller, A., & Rübe, C. E. (2021). Fractionated Low-Dose Radiation Induces Long-Lasting Inflammatory Responses in the Hippocampal Stem Cell Niche. *International Journal of Radiation Oncology Biology Physics*, *111*(5), 1262–1275. https://doi.org/10.1016/j.ijrobp.2021.07.007

Schmal, Z., & Rübe, C. E. (2022). Region-Specific Effects of Fractionated Low-Dose Versus Single-Dose Radiation on Hippocampal Neurogenesis and Neuroinflammation. *Cancers*, *14*(22). https://doi.org/10.3390/CANCERS14225477

Scholz, M. (2003). Effects of ion radiation on cells and tissues. *Advances in Polymer Science*, *162*, 95–155. https://doi.org/10.1007/3-540-45668-6_4/COVER

Schuy, C., Weber, U., & Durante, M. (2020). Hybrid Active-Passive Space Radiation Simulation Concept for GSI and the Future FAIR Facility. *Frontiers in Physics*, *8*, 337. https://doi.org/10.3389/fphy.2020.00337

Schwartz, M., & Baruch, K. (2014). The resolution of neuroinflammation in neurodegeneration: leukocyte recruitment via the choroid plexus. *The EMBO Journal*, *33*(1), 7–22. https://doi.org/10.1002/EMBJ.201386609

Seed, T., Kumar, S., Whitnall, M., Srinivasan, V., Singh, V., Elliott, T., Landauer, M., Miller, A., Chang, C. M., Inal, C., Deen, J., Gehlhaus, M., Jackson, W., Hilyard, E., Pendergrass, J., Toles, R., Villa, V., Miner, V., Stewart, M., … Farrell, C. (2002). New strategies for the prevention of radiation injury: possible implications for countering radiation hazards of long-term space travel. *Journal of Radiation Research*, *43 Suppl*. https://doi.org/10.1269/JRR.43.S239

Sheppard, O., Coleman, M. P., Durrant, C. S., & authors, more. (2018). Microglia-dependent presynaptic disruption in an organotypic hippocampal slice culture model of neuroinflammation. *BioRxiv*, 502559. https://doi.org/10.1101/502559

Shimura, T., Sasatani, M., Kamiya, K., Kawai, H., Inaba, Y., & Kunugita, N. (2016). Mitochondrial reactive oxygen species perturb AKT/cyclin D1 cell cycle signaling via oxidative inactivation of PP2A in lowdose irradiated human fibroblasts. *Oncotarget*, *7*(3), 3559–3570. https://doi.org/10.18632/ONCOTARGET.6518

Sierra, A., Encinas, J. M., Deudero, J. J. P., Chancey, J. H., Enikolopov, G., Overstreet-Wadiche, L. S., Tsirka, S. E., & Maletic-Savatic, M. (2010). Microglia shape adult hippocampal neurogenesis through apoptosis-coupled phagocytosis. *Cell Stem Cell*, *7*(4), 483–495. https://doi.org/10.1016/J.STEM.2010.08.014

Simonsen, L. C., Slaba, T. C., Guida, P., & Rusek, A. (2020). NASA's first ground-based galactic cosmic ray simulator: Enabling a new era in space radiobiology research. *PLoS Biology*, *18*(5). https://doi.org/10.1371/journal.pbio.3000669

Simpson, J. A. (1983). ELEMENTAL AND ISOTOPIC COMPOSITION OF THE GALACTIC COSMIC RAYS. In *Ann. Rev. Nucl. Part. Sci* (Vol. 33). www.annualreviews.org

Soethoudt, M., Grether, U., Fingerle, J., Grim, T. W., Fezza, F., De Petrocellis, L., Ullmer, C., Rothenhäusler, B., Perret, C., Van Gils, N., Finlay, D., Macdonald, C., Chicca, A., Gens, M. D., Stuart, J., De Vries, H., Mastrangelo, N., Xia, L., Alachouzos, G., … Van Der Stelt, M. (2017). Cannabinoid CB2 receptor ligand profiling reveals biased signalling and off-target activity. *Nature Communications 2017 8:1*, *8*(1), 1–14. https://doi.org/10.1038/ncomms13958

Song, X., Ma, F., & Herrup, K. (2019). Accumulation of Cytoplasmic DNA Due to ATM Deficiency Activates the Microglial Viral Response System with Neurotoxic Consequences. *The Journal of Neuroscience*, *39*(32), 6378. https://doi.org/10.1523/JNEUROSCI.0774-19.2019

Sorokina, S. S., Malkov, A. E., Shubina, L. V., Zaichkina, S. I., & Pikalov, V. A. (2021). Low dose of carbon ion irradiation induces early delayed cognitive impairments in mice. *Radiation and Environmental Biophysics*, *60*(1), 61–71. https://doi.org/10.1007/S00411-020-00889-0

Sridharan, D. M., Asaithamby, A., Bailey, S. M., Costes, S. V., Doetsch, P. W., Dynan, W. S., Kronenberg, A., Rithidech, K. N., Saha, J., Snijders, A. M., Werner, E., Wiese, C., Cucinotta, F. A., & Pluth, J. M. (2015). Understanding cancer development processes after HZE-particle exposure: roles of ROS, DNA damage repair and inflammation. *Radiation Research*, *183*(1), 1–26. https://doi.org/10.1667/RR13804.1

Stoppini, L., Buchs, P.-A., & Muller, D. (1991). A simple method for organotypic cultures of nervous tissue. In *Journal of Neuroscience Methods'* (Vol. 37).

Stuster, J. (2016). *Behavioral Issues Associated With Long Duration Space Expeditions: Review and Analysis of Astronaut Journals; Experiment 01-E104 (Journals) Phase 2 Final Report*. http://www.sti.nasa.gov

Sun, L., Apweiler, M., Normann, C., Grathwol, C. W., Hurrle, T., Gräßle, S., Jung, N., Bräse, S., & Fiebich, B. L. (2024). Anti-Inflammatory Effects of GPR55 Agonists and Antagonists in LPS-Treated BV2 Microglial Cells. *Pharmaceuticals 2024, Vol. 17, Page 674*, *17*(6), 674. https://doi.org/10.3390/PH17060674

Tanaka, M., Sackett, S., & Zhang, Y. (2020). Endocannabinoid Modulation of Microglial Phenotypes in Neuropathology. *Frontiers in Neurology*, *0*, 87. https://doi.org/10.3389/FNEUR.2020.00087

Taniguchi, K., & Karin, M. (2018). NF-κB, inflammation, immunity and cancer: coming of age. *Nature Reviews. Immunology*, *18*(5), 309–324. https://doi.org/10.1038/NRI.2017.142

Timmerman, R., Burm, S. M., & Bajramovic, J. J. (2018). An overview of in vitro methods to study microglia. *Frontiers in Cellular Neuroscience*, *12*, 242. https://doi.org/10.3389/FNCEL.2018.00242/BIBTEX

Tudurí, E., Imbernon, M., Hernández-Bautista, R. J., Tojo, M., Fernø, J., Diéguez, C., & Nogueiras, R. (2017). GPR55: a new promising target for metabolism? *Journal of Molecular Endocrinology*, *58*(3), R191–R202. https://doi.org/10.1530/JME-16-0253

Turcotte, C., Blanchet, M. R., Laviolette, M., & Flamand, N. (2016). The CB2 receptor and its role as a regulator of inflammation. *Cellular and Molecular Life Sciences: CMLS*, *73*(23), 4449. https://doi.org/10.1007/S00018-016-2300-4

Turnquist, C., Harris, B. T., & Harris, C. C. (2020). Radiation-induced brain injury: current concepts and therapeutic strategies targeting neuroinflammation. *Neuro-Oncology Advances*, *2*(1), 1–10. https://doi.org/10.1093/NOAJNL/VDAA057

Ung, M.-C. (2020). *The long-term effects of low dose ionizing radiation on the adult mouse brain and consequences for behavior*. T.

Ung, M.-C., Garrett, L., Dalke, C., Leitner, V., Dragosa, D., Hladik, D., Neff, F., Wagner, F., Zitzelsberger, H., Miller, G., Hrabě De Angelis, M., Rößler, U., Weisenhorn, D. V., Wurst, W., Graw, J., & Hölter, S. M. (2021). International Journal of Radiation Biology ISSN: (Print) (Online) Journal homepage: https://www.tandfonline.com/loi/irab20 Dose-dependent long-term effects of a single radiation event on behaviour and glial cells) Dose-dependent long-term effects of a single radiation event on behaviour and glial cells. *International Journal of Radiation Biology*, *97*(2), 156–169. https://doi.org/10.1080/09553002.2021.1857455

Vidal-Itriago, A., Radford, R. A. W., Aramideh, J. A., Maurel, C., Scherer, N. M., Don, E. K., Lee, A., Chung, R. S., Graeber, M. B., & Morsch, M. (2022). Microglia morphophysiological diversity and its implications for the CNS. *Frontiers in Immunology*, *13*. https://doi.org/10.3389/FIMMU.2022.997786

von Widdern, J. C., Hohmann, T., & Dehghani, F. (2020). Abnormal cannabidiol affects production of pro-inflammatory mediators and astrocyte wound closure in primary astrocytic-microglial cocultures. *Molecules*, *25*(3). https://doi.org/10.3390/molecules25030496

Voshart, D. C., Oshima, T., Jiang, Y., van der Linden, G. P., Ainslie, A. P., Reali Nazario, L., van Buuren-Broek, F., Scholma, A. C., van Weering, H. R. J., Brouwer, N., Sewdihal, J., Brouwer, U., Coppes, R. P., Holtman, I. R., Eggen, B. J. L., Kooistra, S. M., & Barazzuol, L. (2024). Radiotherapy induces persistent innate immune reprogramming of microglia into a primed state. *Cell Reports*, *43*(2). https://doi.org/10.1016/J.CELREP.2024.113764

Vuic, B., Milos, T., Tudor, L., Konjevod, M., Nikolac Perkovic, M., Jazvinscak Jembrek, M., Nedic Erjavec, G., & Svob Strac, D. (2022). Cannabinoid CB2 Receptors in Neurodegenerative Proteinopathies: New Insights and Therapeutic Potential. *Biomedicines 2022, Vol. 10, Page 3000*, *10*(12), 3000. https://doi.org/10.3390/BIOMEDICINES10123000

Wang, L. L., Zhao, R., Li, J. Y., Li, S. S., Liu, M., Wang, M., Zhang, M. Z., Dong, W. W., Jiang, S. K., Zhang, M., Tian, Z. L., Liu, C. S., & Guan, D. W. (2016). Pharmacological activation of cannabinoid 2 receptor attenuates inflammation, fibrogenesis, and promotes re-epithelialization during skin wound healing. *European Journal of Pharmacology*, *786*, 128–136. https://doi.org/10.1016/j.ejphar.2016.06.006

Warden, A. S., Han, C., Hansen, E., Trescott, S., Nguyen, C., Kim, R., Schafer, D., Johnson, A., Wright, M., Ramirez, G., Lopez-Sanchez, M., & Coufal, N. G. (2023). Tools for studying human microglia: In Vitro and In Vivo Strategies. *Brain, Behavior, and Immunity*, *107*, 369. https://doi.org/10.1016/J.BBI.2022.10.008

Witter, M. P., & Amaral, D. G. (2004). Hippocampal Formation. In *The Rat Nervous System* (pp. 635–704). Academic Press. https://doi.org/10.1016/B978-012547638-6/50022-5

Yoo, S. S., Jorgensen, T. J., Kennedy, A. R., Boice, J. D., Shapiro, A., Hu, T. C. C., Moyer, B. R., Grace, M. B., Kelloff, G. J., Fenech, M., Prasanna, P. G. S., & Coleman, C. N. (2014). Mitigating the risk of radiation-induced cancers: limitations and paradigms in drug development. *Journal of Radiological Protection : Official Journal of the Society for Radiological Protection*, *34*(2), R25. https://doi.org/10.1088/0952-4746/34/2/R25

Young, K., & Morrison, H. (2018). Quantifying Microglia Morphology from Photomicrographs of Immunohistochemistry Prepared Tissue Using ImageJ. *Journal of Visualized Experiments : JoVE*, *2018*(136), 57648. https://doi.org/10.3791/57648

Zhao, C., Dong, Y., Liu, J., Cai, H., Li, Z., Sun, X., Yin, W., Ma, J., Liu, H., & Li, S. (2021). An enzyme-responsive Gp1a-hydrogel for skin wound healing. *Journal of Biomaterials Applications*, *36*(4), 714–721. https://doi.org/10.1177/08853282211012870

9 EHRENWORTLICHE ERKLÄRUNG

Ich erkläre hiermit, dass ich die vorliegende Arbeit entsprechend den „Regeln guter wissenschaftlicher Praxis der Technischen Universität Darmstadt“ selbstständig und ohne unzulässige Hilfe Dritter angefertigt habe. Sämtliche, aus fremden Quellen direkt oder indirekt übernommenen Gedanken sowie sämtliche von Anderen direkt oder indirekt übernommenen Daten, Techniken und Materialien sind als solche kenntlich gemacht.

Ferner erkläre ich, dass ich bei der Verfassung der Dissertation die „Leitlinien zum Umgang mit digitalen Forschungsdaten an der TU Darmstadt“ in der jeweiligen aktuellen Version beachtet habe. Die Arbeit wurde bisher bei keiner anderen Hochschule zu Prüfungszwecken eingereicht.

Berlin, den 22.01.2025

BD

.....

10 ACKNOWLEDGMENTS

Diese Dissertation wurde durch die Unterstützung der Helmholtz Graduiertenschule „HGS-HIRe for FAIR“ ermöglicht. Darüber hinaus danke ich dem **Deutschen Zentrum für Luft- und Raumfahrt (DLR)** und der **Europäischen Weltraumorganisation (ESA)** für die finanzielle Förderung dieser Arbeit sowie für die Möglichkeit, meine Forschung in einen außergewöhnlich spannenden wissenschaftlichen Kontext einbetten zu können.

Mein besonderer Dank gilt **Prof. Marco Durante** für die Möglichkeit, meine Doktorarbeit in der Abteilung Biophysik der GSI anzufertigen, für die Übernahme des Erstgutachtens sowie für das wertvolle Feedback und die Teilnahme an der ESA-FAIR Space Radiation School. **Prof. Alexander Löwer** danke ich herzlich für die Übernahme des Zweitgutachtens sowie für die langjährige fachliche und persönliche Unterstützung, die über viele Jahre der Zusammenarbeit hinweg von unschätzbarem Wert war.

Ein besonderer Dank gilt **Dr. Felicitas Rapp und Prof. Sonja Kallendrusch** für ihre engagierte Betreuung über die räumliche Distanz hinweg, das sorgfältige Korrekturlesen, ihre Geduld, wertvolle Ratschläge und ihre herzliche Unterstützung. Gemeinsam haben wir die Herausforderungen der Jahre 2019 bis 2024 gemeistert und sind daran gewachsen. Mein Dank gilt ebenfalls **Prof. Ingo Bechmann** und dem gesamten Team der Anatomie der Universität Leipzig für die wertvolle Unterstützung in der Erforschung von Mikrogliazellen. Insbesondere danke ich **Dr. Karsten Winter**, dessen Expertise mir stets hoffnungsvoll zur Seite stand.

Prof. Lisa Sevenich danke ich für die Annahme und Haltung meiner Versuchstiere sowie für die Bereitstellung der Infrastruktur im Georg-Speyer-Haus, die maßgeblich zum Gelingen dieser Arbeit beigetragen hat. Meiner Bachelorstudierenden **Britta Lipinski** spreche ich meinen herzlichen Dank für ihre engagierte Mitarbeit und ihre Bereitschaft aus, stets über sich hinauszuwachsen.

Nicht zuletzt gedenke ich mit größtem Respekt den über **300 Versuchstieren**, die ihr Leben für die Wissenschaft gegeben haben. Ihr Beitrag wird nicht vergessen.

11 PUBLICATIONS, CONFERENCES AND SUPERVISED THESES

Publication

Djouiai B, Thwaite JE, Laws TR, Commichau FM, Setlow B, Setlow P, Moeller R. Role of DNA Repair and Protective Components in Bacillus subtilis Spore Resistance to Inactivation by 400-nm-Wavelength Blue Light. Appl Environ Microbiol. 2018 Sep 17;84(19): e01604-18. doi: 10.1128/AEM.01604-18. PMID: 30054368; PMCID: PMC6147000.

Conference Contributions

Gravimeeti meeting April 2022, „Effects Of Space-Relevant Heavy Ions On The Immune Cells of the Brain.“; Conference talk

European Molecular Biology Organization (EMBO) Workshop, Microglia, Oktober 2021, „Effects of ionizing space radiation on microglia in murine brain slice cultures.“, Poster presentation

Gravimeeting November 2020, „Space_Brain: Welche Rolle spielt die Modulierung von Mikroglia bei (Weltraum-) strahleninduzierten Schäden des ZNS?“, Conference talk

ESA IBER Workshop Juli 2020, „Space_brain: Finding countermeasures to cosmic radiation-induced neuroinflammation.“ Conference talk

Supervised Theses

Britta Lipinski, Bachelorarbeit an der Hochschule Darmstadt 2020, “Effekte von Röntgenstrahlung auf Mikroglia in organotypischen hippocampalen Schnittkulturen von Mäusen.“